Impacts of Vegetation-Generated Turbulence on Sediment Transport

by

Qingjun Judy Yang

S.M., Massachusetts Institute of Technology (2015)

Submitted to the Department of Civil and Environmental Engineering
in partial fulfillment of the requirements for the degree of

Doctor of Philosophy

at the

MASSACHUSETTS INSTITUTE OF TECHNOLOGY

September 2018

Author .... Signature redacted ....
Department of Civil and Environmental Engineering
August 9, 2018

Certified by.. Signature redacted ....
Heidi M. Nepf
Donald and Martha Harleman Professor
Thesis Supervisor

Accepted by... Signature redacted ....
Heidi M. Nepf
Chairman, Department Committee on Graduate Theses

Impacts of Vegetation-Generated Turbulence on Sediment Transport

by

Qingjun Judy Yang

Submitted to the Department of Civil and Environmental Engineering
on August 9, 2018, in partial fulfillment of the
requirements for the degree of
Doctor of Philosophy

Abstract

Aquatic vegetated habitats, including wetlands and mangroves, are disappearing at an annual rate of 1 to 7%. These ecosystems provide habitats important to fisheries, enhance water quality by filtering nutrients from run-off, and also protect coastal regions from storm surges and waves. To mitigate the loss of these habitats, restoration projects import sediment to eroded areas. The success of the restoration depends on its ability to retain sediment; therefore restoration design requires a good understanding of sediment transport within vegetated landscapes. However, there is currently no quantitative model for sediment transport in vegetated regions, and many restoration projects have failed due to unanticipated erosion from the restored regions. The goal of this thesis is to develop a predictive model for sediment transport in regions with vegetation.

First, the affect of vegetation on the critical condition when sediment start to move was explored. To identify the critical condition, an imaging system was designed to track the trajectories of individual moving grain through running water. The critical flow velocity (U_{crit}) above which sediment starts to move was identified from the tracked sediment trajectories for both bare (non-vegetated) and vegetated regions. The experimental results showed that for the same type of sediment, U_{crit} decreased with increasing vegetation solid volume fraction. This was attributed to the vegetation-generated turbulence, which induced a local, vertical, adverse pressure, or a lift force on the sediment grain, facilitating sediment transport. In contrast, the turbulent kinetic energy (k_t) was found to be roughly a constant at the critical condition for different vegetation volume fractions, suggesting that k_t is a more universal metric than τ for predicting the critical condition of the sediment transport. A k_t-based model was developed to predict U_{crit} for channels with different vegetation solid volume fractions. The turbulence-based model successfully predicted U_{crit} for both bare and vegetated channels, providing a useful tool for ecologists to predict whether a vegetated landscape will erode or not.

Second, the impact of vegetation on the bed load transport rate was explored. A system that allows sediment to be bypassed, a cart to distribute sediment, a method that measures the dry weight of wet sand without drying the sediment, a topography system, and an sediment trajectory imaging system were designed. The bed load transport rate (Q_s) was measured for both bare channels and channels with different vegetation solid volume fractions (ϕ) under different flow rates. At the same τ, the measured Q_s increased with increasing ϕ, suggesting that vegetation-generated turbulence, which also increased with increasing ϕ, was augmenting the bed load transport. At the same near-bed turbulent kinetic energy, k_t, the Q_s measured in both bare and vegetated channels agreed within uncertainty, suggesting that k_t may be a more universal predictor of Q_s than τ. The Einstein-Brown τ-based bed load transport model was reinterpreted as a k_t-based model. The new k_t-based model predicted the Q_s measurements for both bare and vegetated channels. The dependence of Q_s on k_t was explained by the statistics of individual grain motion, which showed that Q_s was predominantly controlled by the number of grains in motion, which correlated with k_t. The proposed k_t-based sediment transport model can be used to simulate large-scale landscape evolution and to help ecologists design better coastal restoration strategies.

Third, the impacts of vegetation on bedform characteristics and migration rate were studied. After the measured bed load transport rate converged to an equilibrium value, the bed topography was scanned by a laser topography system. Bedforms with height less than $2cm$ were observed and characterized as ripples. For low vegetation solid volume fraction ($\phi \leq 0.012$), the ripple wavelength was constrained by stem spacing and the ripple height increased with increasing ϕ. However, at the highest vegetation solid volume fraction ($\phi = 0.025$), the ripple height was comparable to the grain size, indicating that an plane bed had formed. The ripple migration speed and the bed load flux associated with the migrating ripples increased with increasing vegetation solid volume fraction for $\phi \leq 0.012$. However, the fraction of the bed load flux carried by migrating ripples decreased with increasing ϕ, suggesting that vegetation facilitated the formation of sheet flow. The impacts of vegetation on bedforms presented here will provide a potential tool for geologists to infer the occurrence of vegetation-related events from geomorphological records.

Thesis Supervisor: Heidi M. Nepf
Title: Donald and Martha Harleman Professor

Acknowledgments

Foremost, I would like to express my deepest gratitude to my advisor, Dr. Heidi Margaret Nepf. My five-year journey towards PhD would never have been so enjoyable, memorable, fruitful, and even possible without the guidance, support, and encouragement of Heidi. Heidi is enthusiastic for science, patient in teaching and mentoring, open-minded to new ideas, and extremely meticulous and rigorous in conducting research. She cares a lot about the people around her and our mother nature and gives as much support as possible to her students and other young researchers. She has great work-life balance, and is always calm and objective. Heidi is my role model. Her distinguished academic achievements, never-give-up personality, and great work-life balance encourages me to continue taking challenges and pursuing academic excellence in a sustainable way. It is a great pleasure to be Heidi's graduate student, and I am very grateful for her guidance, support, and encouragement.

I am tremendously grateful to have the best thesis committee I could every ask for: Dr. Eric Adams, Dr. John Trowbridge, and Dr. Taylor Perron. This thesis would not be possible without the insightful advice and critical suggestions by my committee. Without the recommendation and endless support from my committee, I would not have the opportunity and courage to continue pursuing challenging research questions. I would like to thank Eric for always being willing to meet with me and give me advice whenever I need help and for sharing with me wisdoms about science and life in various circumstances, such as student reception and TGIF. I would like to thank John for pushing me to think more critically and providing support and valuable suggestions for my career. I was very touched when John sent me detailed comments and suggestions on my job application package after I asked for his recommendation. I would like to thank Taylor for inviting me to join his group activities, introducing me to his colleagues, sharing with me his research vision, and encouraging me to take challenges and pursue interdisciplinary research interests. In addition to my committee, I also received tremendous help and support from Dr. Sergio Fagherazzi. I would like to thank Sergio for giving me the opportunity to work with him in the field and for his guidance and support. His open-mindedness in research and teaching has inspired me to think more broadly.

My sincere appreciate also goes to my two proud undergraduate research assistants, Hayoon Chung and Milani Chatterji-Len, who conducted fantastic research which became part of my thesis. My research would not be possible without the help of Andrew Ryan and Scott Spence, who helped with the design and fabrication of the flume and other instruments, and Brenda Pepe, who helped with the purchase, finance, and documentation. I would also like to thank members from the Nepf lab, the MIT Environmental Fluid Mechanics community, and the COFDL community for all the help, support, and company, in particular, Francois Kerger, Jiarui Lei, Yinghao Zhang, John Kondziolka, Elizabeth Follet, Alejandra Oritiz, Jeffrey Rominger, Ruoqian Wang, Chao Yan, Zhenghong Hu, Julien Hopkins, Jenny Weholf, Katie Samuelson, Cindy Wang, Aaron Chow, Ishita Shrivastava, and Anna Wargula. I extend my thanks to William Kearney, Xiaohe Zhang, and students from Sergio's field course for helping me with field work, and thank Dr. Noah Snyder for lending me his bedload sampler. The generous funding support from the Martin family and National Science Foundation is also greatly appreciated.

My life at MIT would not be as smooth and colorful without my wonderful friends from Parsons. I am extremely lucky to have Xiaojing(Ruby) Fu and Jen Nguyen as my friends, mentors, and soul mates. You brought the sunshine and tons of love into my life. I thank Noriko Endo, Neha Mehta for generously sharing your knowledge and wisdom with me; thank Irene Hu, Alison Hoyt, Mariam Allam, Osama Mekki Seidahmed, Anjuli Figueroa, Reetik Sahu, Tiziana Mercado, Sidhant Pai, Michael Chen, Hayley Gadol, Chuliang Song, and Kyle Delwiche for your support, company, and help.

Having the opportunity to initiate and work on TREES (http://trees.mit.edu/) is one of the best things that happened in my life. Special thanks to TREES environmental fighters and artists and advisors: William Porter, Sarah Safieddine, Wenjia Wang, Shanshan Song, Xuan Wang, Kai Yu, Jen Nguyen, Ruby Fu, Max Kessler, Xuanzong Guo, Dan Li, Britt Huhmann, Jane Chui, Rounaq Basu, Yi Xue, Hayley

Gadol, Jared Berezin, and Colette Heald. Love and support from you made me believe that we have the power to make the world a better place. Many thanks to the open-minded and supportive CEE leaders who gave tremendous support and help to TREES: CEE department head Markus Buehler, Kiley Clapper, and the CEE headquarter. Thanks to MIT Environmental Solution Initiative and others who supported TREES.

I would also like to express my gratitude for the help and support from my friends, advisors, and mentors at MIT and all over the world. I extremely thank Maxine Jonas, Ed Carlevale, Hongri Gu, Hongbo Ma, and Thalia Rubio for your help and support with my job/posdoc application; thank GSLI community for all the love you brought to my life; thank my undergraduate mentors and advisors for your support and advise before and after my graduation, especially Dr. Ying Chen, Dr. Liwu Fan, and Dr. Zitao Yu; thank the MIT Geomorphology group for letting me being part of your community and sharing with me your knowledge.

Last but not least, I want to thank my family for unconditional love and support, especially Chunmei Yang, Tingsheng Yang, and Xiaofan Jiang. My family is my refueling station, giving me the courage and power to take challenges and pursue my dreams. Thank you for giving me the freedom to explore whatever I like, always being there for me, and always trusting my choices and decisions.

Contents

List of Figures

List of Tables

Chapter 1

Introduction

1.1 Fundamentals of sediment transport

Sediment transport is an important process that affects the lives of humans and other living creatures in various ways [45]. For example, coastal erosion and migration of rivers and streams caused by sediment transport endangers our infrastructures and the habitats of many species [108]. Deposition of sediment in drainage ditches, canals, and navigation channels impedes the normal operation of these systems and creates large clean-out costs [108], and deposition in farm lands can bury crops, affecting agriculture productivity [41]. Excess suspended sediment in water suffocates fish and affects their feeding ability by attenuating light [5]. Impingement of abrasive sediment on machine surfaces causes turbines and other components in hydropower plants to wear out [23]. In addition, sediment transport exposes carbon-rich soils to microbial processes and induces a large amount of green house gas emission, up to 10% of fossil fuel emissions [54]. Understanding sediment transport processes is important for addressing and mediating the above sedimentation-related problems [108], yet the fundamental mechanisms of sediment transport is still not fully understood due to the intrinsic complexity of turbulence and sediment-fluid-structure interactions [69, 21].

The sediment transport processes inside vegetation is particularly important to understand, because erosion is one of the major causes of the loss of coastal vegetated habitats in the past several decades, including half of the world's wetlands [124] and thousands of acres of seagrass in the U.S. [59]. Vegetation also affects the geomorphic evolution of rivers and floodplains [58, 77], which greatly affects the survival and abundance of aquatic species such as salmon [36]. In order to restore these eroding habitats and protect the species vulnerable to erosion, predictive models for sediment transport in vegetated areas is needed.

Sediment transport is divided into bed load transport and suspended load transport. Bed load refers to the sediment moving with frequent contact with the bed in a confined bed layer region, whose thickness is usually several times the grain diameter [45]. Suspended load refers to sediment moving with the flow in suspension and without frequent contact with the bed [45]. Studies in open channel flows have shown that bed load starts to occur when the shear stress exerted on the grains by the flow exceeds a critical value, called the critical bed shear stress [86]. For each sediment grain size and grain density, the critical shear stress can be inferred from the empirically-constructed Shields diagram [86]. Sediment suspension occurs when upward turbulent diffusion become large enough to balance the settling of the particle due to gravity [45]. Bedload transport rate and suspended load transport rate are usually calculated separately. In particular, most bedload equations estimate the bedload transport rate based on the mean bed shear stress, representing the horizontal drag force on the grains, while the transport rates of suspended load are often a function of the turbulent diffusivity [45]. In this study, we focus on the bedload transport.

1.2 Classic bedload transport models

Current bedload transport models are based on time-mean bed shear stress τ and are mostly empirical or semi-empirical. Pioneering bedload transport studies trace back to 1879, when M.P. Duboys [24] proposed the bed shear stress concept. He assumed that grains move in layers and that the shear stress or tractive force has to overcome the frictions between grains to move the sediment. With support from experimental data, the following semi-empirical Duboys bedload equation was proposed [45]:

$$q_{bv} = \frac{0.173}{d_s^{3/4}}\tau(\tau - \tau_{crit}). \tag{1.1}$$

Here q_{bv} is the volume of sediment in motion per unit width and time in ft^2/s, τ is the bed shear stress in unit lb/ft^2, d_s is the sediment size in mm, and τ_{crit} is the critical shear stress which Duboys approximated as $= 0.0125 - 0.019d_s$. Note that the constants 0.173 in the equation was empirical and has the unit $\frac{[ft]^6[mm]^{3/4}}{[s][lb]^2}$.

The critical bed shear stress can also be estimated based on the classic Shields diagram [86]. Specifically, the Shields curve plots $\tau_{crit}/(\rho_s - \rho)d_s$ as a function of the particle Reynolds number $Re_* = \frac{u_* d_s}{\nu} = \frac{\sqrt{\tau_{crit}/\rho}d_s}{\nu}$, with ρ, ρ_s, g, and ν representing the fluid density, sediment density, gravitational constant, and the fluid kinetic viscosity. Iterations are required to find τ_{crit}.

Following Duboys, a number of empirical τ-based bedload transport models were developed based on lab and field measurements. One of the most-widely-used models is the Meyer-Peter Muller equation [64], which estimates the dimensionless bedload transport, Q_{s*}, as a function of dimensionless bed shear stress (τ_*) ,

$$Q_{s*} = \frac{q_{bv}}{\sqrt{(\rho_s/\rho - 1)gd_s^3}} = 8(\tau_* - 0.047)^{3/2}, \tag{1.2}$$

$$\tau_* = \frac{\tau}{(\rho_s - \rho)gd_s}. \tag{1.3}$$

The Meyer-Peter Muller equation was fitted to the data of [63] and part of the data from [32] with τ_* ranging from 0.06 to 0.18. Wiberg and Smith [114] further generalized the Meyer-Peter Muller's equation to τ_* outside the 0.06 to 0.18 range:

$$Q_{s*} = \beta(\tau_* - \tau_{*crit})^{3/2}. \tag{1.4}$$

Here β is a fitting variable ranging from 5 to 15, depending on the range of $\tau_* - \tau_{*crit}$.

Based on probability concepts, Einstein [26] derived an expression for the dimensionless bedload transport rate Q_{s*} as a function of τ_*,

$$Q_{s*} = \frac{q_{bv}}{\omega_0 d_s} = f(\tau_*), \tag{1.5}$$

Einstein nondimensionalized q_{bv} by the fall velocity ω_0 and d_s based on dimensional analysis. The particle fall velocity can be approximated by the Rubey's approximate equation [83],

$$\omega_0 = \left(\sqrt{\frac{2}{3} + \frac{36\nu^2}{(\rho_s/\rho - 1)gd_s^3}} - \sqrt{\frac{36\nu^2}{(\rho_s/\rho - 1)gd_s^3}}\right)\sqrt{(\rho_s/\rho - 1)gd_s} \tag{1.6}$$

For coarse sand and gravel (e.g. $d_s > 1mm$), $\omega_0 \approx \sqrt{(\rho_s/\rho - 1)gd_s}$, which leads to the same as the nondimensionalization used in equation 1.2. In deriving equation 1.5, Einstein assumed that particles move in steps of average length proportional to d_s and that the probability of a particle to be moved is a function of the ratio of the lift force on the grain to its submerged weight. He further assumed that the lift force is proportional to the bed shear stress. Brown [8] fitted different formulas of $Q_{s*} = f(\tau_*)$ to experimental data and proposed the Einstein-Brown bedload model:

$$Q_{s*} = \begin{cases} 2.15e^{-0.391/\tau_*}, & \tau_* < 0.18 \\ 40\tau_*^3, & 0.18 < \tau_* < 0.52. \end{cases} \tag{1.7}$$

At low sediment transport region ($\tau_* < 1$), the Einstein-Brown model agrees well with the bedload measurements compiled in Figure 9.2 of [45].

1.3 Limitations of current bedload models

Despite the fact that the time-mean bed shear stress (τ)-based models can predict bedload transport in some flow conditions, the mechanisms of bedload transport are still poorly understood due to the complex nature of turbulence and fluid-sediment interactions. In particular, a number of studies have shown that in addition to the mean shear stress, τ, the instantaneous stress or turbulence also play an important role in sediment transport [37, 95, 69, 94]. For example, the instantaneous sediment transport rate was measured in a tidal channel and observed to be intermittent, linked to the bursting patterns of the near-bed turbulence [37]. Sumer et al. [95, 94] conducted flume experiments with obstacles and observed a five-fold increase in Q_s with 20% increase in k_t at conditions with the same τ, suggesting that k_t may play a more important control on Q_s than τ. Nelson et al. [69] conducted experiments in a channel with simulated bedforms and observed that sweeps and ejections, which contribute equally to τ, produce significantly different sediment transport rates. More recent studies further showed that in addition to the stress fluctuations, the duration of the fluctuations plays an important role the bedload transport [21]. Specifically, Diplas et al. [21] have shown that in order for a grain to move, not only does the magnitude of the peak force have to be above a critical value, but also the impulse, which is product of the magnitude and duration of the instantaneous force larger than the critical force, has to be larger than a critical value, depending on the grain size [10, 11]. Other studies have shown that in contrast with the horizontal drag on the sediment grain, which is proportional to the bed shear stress, the lift force on the grains provides a dominant control in sediment transport [95, 75, 88]. For example, flow visualization has revealed that turbulent bursts can lift up sediment grains, initiating sediment transport [95, 75]. Smart and Habersack [88] measured the pressure gradient above and below a gravel and showed that the uplift force on the sediment grain due to the advecting turbulence can overcome the submerged weight of the grain, initiating grain entrainment. The Einstein-relationship (equation 1.5) was based on the assumption that the probability of particle in motion depends on the ratio of the lift force to the particle submerged weight and that the lift force is proportional to τ. For conditions in which the lift force does not scale with τ, the Einstein-theory could be interpreted as the dimensionless bedload transport as a function of dimensionless lift force instead of τ. For channels with steady and uniform flow, the turbulent kinetic energy, the lift force, and τ are linearly related [8, 69] such that the role of turbulence, lift force, and the bed shear stress are coupled and the τ-based models already incorporate information about the turbulence and lift force. However, in places with obstacles, such as bedforms and vegetation, the τ-based models have been found to be inaccurate [69, 94, 118]. Nelson et al. [69] measured the sediment transport rate and bed shear stress at different locations relative to a step and found that the correlation between sediment transport rate and the bed stress is quite poor. Sumer et al. [94] measured bed load transport rate in channels with and without external turbulence generators, such as horizontal pipes and grids, and found that the bed load transport rate correlated with the fluctuations of the bed stress instead of the mean bed shear stress τ. Yager and Schmeeckle [118] measured the bed load transport rate and bed shear stress simultaneously in channels with emergent model vegetation and found that commonly-used τ-based models can not predict sediment transport in vegetated channels. This is likely because these obstacles generates additional turbulence which induces additional lift force so that the lift force and τ are not linearly related and τ-based models do not incorporate information about turbulence and the lift force in channels with external turbulence generators.

The inaccuracy of τ-based bedload models in regions with vegetation is particularly problematic because vegetation is prevalent in coastal areas, rivers, and streams, and erosion inside vegetation poses a serious threat to human habitats and other living creatures [115, 118, 55]. For example, erosion is one of the major causes of the loss of coastal vegetated habitats in the past several decades, including half of the world's wetlands [124] and thousands of acres of seagrass in the U.S. [59]. Vegetation also affects the geomorphic evolution of rivers and floodplains [58, 77], which greatly affects the survival and abundance of aquatic species such as salmon [36]. In order to restore these eroding habitats and protect the species vulnerable to erosion, predictive models for bedload transport in vegetated areas is needed. To date, a number of laboratory sediment transport experiments have been conducted in regions with model vegetation, providing important insights into the impact of vegetation on sediment transport [44, 48, 118, 104, 55, 121, 119, 105]. Jordanova and James [44] and Kothyari et al. [48] measured the bedload transport rate in a flume with a sloping bed and with vegetation simulated by cylinders. They calculated the total stress from the slope after the flow became uniform, i.e., after the surface slope and bed slope became the same, and found that the bed load transport rate was not a function of the total stress because a large portion of the total stress was balanced by the vegetation drag. They suggested that the vegetative drag, which is a function of vegetation density, vegetation drag coefficient and velocity, be subtracted from the total drag to estimate the bedload transport rate. However, the vegetation drag coefficient varies with the flow rate, the vegetation stem size, the vegetation solid volume fraction, and the vegetation morphology [98, 70], making it difficult to apply the drag partition method to estimate bed load transport. Yager and Schmeeckle [118] measured both bedload transport rate and near-bed velocity and observed elevated bedload transport rate in places with high turbulence intensity, yet no quantitative bedload model was developed in their study. Tinoco et al. [104, 105] measured the suspended sediment concentration with increasing flow velocity in vegetated channels. They inferred the critical velocity when sediments started to suspend from the measured concentration and found out that the critical velocity decreased with increasing vegetation solid volume fraction, which they attributed to the vegetation-generated turbulence.

1.4 Impact of vegetation-generated turbulence on bedload transport (thesis structure)

This thesis describes the impact of vegetation-generated turbulence on the incipient condition of sediment transport, the bedload transport rate, and the bedform characteristics. Chapter 2 describes how vegetation-generated turbulence significantly reduces the critical bed shear stress at which sediment starts to move. A turbulence-based model is derived and validated to predict the critical velocity for sediment transport in regions with different vegetation volume fractions. Chapter 3 discusses the impact of vegetation-generated turbulence on the bedload transport rate. The current bed shear stress-based bedload models are shown to underestimate the bedload transport rate in channels with vegetation. A re-interpretation of the bed stress-based models into turbulence-based models is proposed, and the re-interpreted turbulence-based bedload model is validated by experimental data. The results show that ignoring vegetation-generated turbulence will lead to an underestimation of bedload transport rate in salt marshes by several orders of magnitude. Chapter 4 further explores the impact of vegetation on bedload transport and bedform characteristics. A model for predicting turbulent kinetic energy in vegetated channels with mobile beds is validated, which provides a tool for applying the turbulence-based bedload transport model when turbulence cannot be measured directly. Ripples were observed, and the ripple wavelength was shown to be constrained by vegetation spacing. The ripple height increased with increase vegetation volume fraction for channels with vegetation volume fraction ≤ 0.012, but was comparable to grain size at high vegetation volume fraction (0.025), suggesting that vegetation both enhances bed-load transport and facilitates an earlier transition to sheet flow. Chapter 5 is a summary of the thesis and future research directions that extend current research to more complicated environment. Appendix A describes the sediment-recirculation flume, tools for distribute and catch the sand, and a method to calculate the bedload transport rate. Appendix B presents the steps to track the trajectories of moving sediment grains. Particle tracking codes are included and a method to validate the trajectories in Adobe Premiere is described in detail. Appendix C illustrates the mechanical design and the LabView interface of a laser topography system and the procedure to use the system. Appendix D documents the measured turbulent kinetic energy and Reynolds stress profiles above mobile sand beds for the experiments described in Chapter 3 and 4. Appendix E documents the measured bed topography profiles in both temporal and spatial domain, which were used to identify the ripple characteristics for both bare and vegetated channels (Chapter 4, Table 4.2).

Chapter 2

The onset of sediment transport in vegetated channels

This laboratory study advances our understanding of sediment transport in vegetated regions, by describing the impact of stem density on the critical velocity, U_{crit}, at which sediment motion is initiated. Sparse emergent vegetation was modeled with rigid cylinders arranged in staggered arrays of different stem densities. The sediment transport rate, Q_s, was measured over a range of current speeds using digital imaging, and the critical velocity was selected as the conditions at which the magnitude of Q_s crossed the noise threshold. For both grain sizes considered here (0.6-0.85mm and 1.7-2mm), U_{crit} decreased with increasing stem density. This dependence can be explained by a threshold condition based on turbulent kinetic energy, k_t, suggesting that near-bed turbulence intensity may be a more important control than bed shear stress on the initiation of sediment motion. The turbulent kinetic energy model unified the bare-bed and vegetated channel measurements. [1]

---

[1] The results of this chapter was published in "JQ Yang, H Chung, and HM Nepf. The onset of sediment transport in vegetated channels predicted by turbulent kinetic energy. *Geophysical Research Letters*, 43(21), 2016."

2.1 Background

Aquatic vegetation provides important ecosystem services [65, 50, 19], whose global value has been estimated to be in the tens of trillion dollars per year [14]. However, a large amount of aquatic vegetation has been lost in recent decades, including over half of the wetlands and thousands of acres of seagrass in the U.S [59]. An understanding of sediment transport in vegetated regions is essential for vegetation restoration because the evolution of vegetated landscape occurs through the interplay of flow, vegetation and sediment accretion. Yet, there are currently no predictive models for sediment transport in vegetation. This study takes a first step toward developing a sediment transport model by quantifying the incipient conditions for sediment transport in vegetated regions. cite In a bare channel the critical velocity defining incipient sediment motion, U_{crit}, has historically been related to the time-mean bed shear stress (τ) [87]. However, more recent studies support the role of turbulence in initiating sediment motion [37, 69, 21]. In a bare channel, the role of turbulence may be inherently represented in the Shields diagram because the turbulent kinetic energy and τ are linearly related [91]. In a vegetated channel, however, the turbulence is predominantly generated by the vegetation [99, 93], such that τ is no longer a surrogate for near-bed turbulence. This may explain why bed shear stress models based on open channel studies do not work in vegetated channels [118, 39, 104].

In this paper, we assume that the near-bed turbulence plays the central role in initiating sediment motion, as also proposed by [69] and [21]. A prediction for U_{crit} is devised based on the near-bed turbulence generated by both bed shear stress and vegetation wakes. The model is shown to be consistent with measurements made in bare and sparsely vegetated channels.

2.2 Theory: a turbulent kinetic energy based model

Previous studies have shown that the initiation of grain motion is connected to the passage of turbulent eddies and the associated fluctuations in near-bed pressure, which generate sufficient instantaneous lift and drag forces to destabilize the grains [88, 123]. Because the magnitude of the fluctuating drag and lift forces are correlated with the near-bed turbulent kinetic energy (k_t), we propose using k_t as a predictor of the incipient condition of sediment transport. This proposal is supported by observations of sediment erosion over a bare bed and a bed with *Spartina anglica* at different stem densities [115]. In the Widdows study, the relation for open channel flow, $\tau = 0.19k_t$, was used to estimate the mean bed stress from the measured turbulent kinetic energy $k_t = (\overline{u'^2}+\overline{v'^2}+\overline{w'^2})/2$, with u', v', w' denoting the velocity fluctuation [91]. However, as discussed in [71, 80, 121], this relation assumes turbulence production is linked to bed stress, which is not true in vegetated systems, for which turbulence production is primarily associated with the vegetation. Therefore, Widdows' conclusion that the critical τ was unchanged between bare and vegetated beds (Figure 6 in [115]) was incorrect, and in fact their data actually shows that the threshold for erosion was defined by a critical value of k_t. Finally, the duration of the turbulence-driven lift and drag is also important, and may be characterized by an impulse parameter (e.g., [10, 11]). The duration is connected to eddy scale, which in turn is connected to the grain size and stem diameter, so that for a fixed grain size and stem diameter, k_t alone should set the critical threshold.

Over a bare channel, the near bed k_t is proportional to τ [91], and τ is proportional to the time-mean, depth-average velocity squared U^2 [116, 45]. Specifically, $k_{tb} = C_b U^2$, with C_b a coefficient dependent on the bed roughness. In a vegetated channel, both the bed-generated turbulence and the vegetation-generated turbulence contribute to the near bed k_t. For simplicity, we assume that the total near-bed k_t is the sum of the two, neglecting any mutual influence. For a sparse emergent canopy, specifically $d/s_n < 0.56$ with d and s_n denoting the stem diameter and the average surface-to-surface distance between the nearest stem neighbor, respectively, which we consider in this study, stem-scale eddies can exist throughout the canopy, so that the vegetation-generated turbulence can be described by equation (4.1) in [99]:

$$k_{tv} = 1.2[C_D \frac{\phi}{(1-\phi)\pi/2}]^{2/3} U^2. \tag{2.1}$$

Here C_D is the stem drag coefficient and ϕ is the solid volume fraction within the canopy. In order for equation (2.1) to apply, the stem Reynolds number Re_d $(= Ud/\nu)$ must be larger than 120 for stem wake turbulence to be generated [56]. In this study $600 < Re_d < 2500$ and $d/s_n \leq 0.25$ ($\phi \leq 5\%$), so that $k_{tv} \approx 1.2(\frac{C_D\phi}{\pi/2})^{2/3}U^2 \approx 0.9C_D^{2/3}\phi^{2/3}U^2$. Assuming that the total near-bed k_t is the sum of k_{tb} and k_{tv}, the total near bed k_t in a sparse emergent canopy can be estimated as:

$$k_t = C_b U^2 + 0.9C_D^{2/3}\phi^{2/3}U^2. \tag{2.2}$$

If k_t sets the threshold for incipient sediment motion, then equation (2.2) can be used to predict the critical velocity. The critical k_t should be a function of the sediment size (d_s). For vegetated and bare channels with the same d_s, $C_b U_{crit}^2 + 0.9C_D^{2/3}\phi^{2/3}U_{crit}^2 = C_b U_o^2$, with U_o denoting the critical velocity for a bare bed, i.e. $U_{crit} = U_o$ when $\phi = 0$. Re-arranging,

$$\frac{U_{crit}}{U_o} = \frac{1}{\sqrt{1 + C\phi^{2/3}}}. \tag{2.3}$$

in which the coefficient $C = 0.9C_D^{2/3}/C_b$. Estimations of C_b and C_D can be found in [45] and [98, 13], respectively. Hereafter equation (2.3) is referred to as the turbulence model for sparse vegetation. For dense vegetation ($d/s_n \geq 0.56$), the turbulence generated in the stem wakes has a weaker dependence on solid volume fraction (Figure 14 and equation (4.1) in [99]), so that U_{crit} is expected to have a weaker dependence on ϕ compared with the sparse vegetation (equation (2.3)).

2.3 Methods: tracking the trajectories of moving sediments in a flume

The model emergent vegetation was created using rigid circular cylinders with diameter $d = 6.3mm$ fixed in a staggered pattern in PVC boards (Figure 2-1). The solid volume fraction (ϕ) ranged from 0.006 to 0.05, similar to conditions found in marshes [70]. One layer of sieved light-brown sand was glued to the PVC boards. Two sand sizes (d_s) were used: 0.6 to 0.85mm and 1.7 to 2mm. The boards were placed in a horizontal recirculating flume with a 1-m wide and 10-m long test section. Flow was generated by a centrifugal pump and measured with an in-line flow meter with $0.001 m^3/hr$ precision. The measured flow rate, Q, was used to estimate the average channel velocity $U = Q/(wh(1-\phi))$, with w and h denoting channel width and water depth, respectively. A digital camera was placed approximately 1m downstream from the leading edge of the boards to observe the sand motion (Figure 2-1b). h was measured close to the camera and was controlled to be 20 to 22cm.

A layer of black sand with the same size distribution as the light-brown sand was spread on top of the light-brown sand. The motion of the black sand was recorded at 60 frames per second with a 1280×960-pixels camera and a 35mm fixed focal length lens (Figure 2-1b). The original imaging area was around 10cm by 7.6cm with one grain diameter corresponding to 10 to 20 pixels. To capture the spatial heterogeneity of sediment motion, the imaging window contained an integral number of the repeated pattern of dowels (Figure 2-1a). To eliminate distortions in the image due to water surface movement, a small glass tank was positioned above the channel and extended less than 1 cm below the water surface (Figure 2-1c).

The following steps were used to estimate the sand transport rate, Q_s. First, in each frame the percentage of the pixels occupied by black sand grains was defined as the black sand occupancy, P_{blk}. Second, the trajectory of each black grain (Figure 2-1a) was identified using IDL particle tracking MatLab code written by Crocker and Grier [17]. Third, the average streamwise velocity of the black sand grains (U_p) was calculated from the identified trajectories, producing an average velocity for all particles over 30 seconds. The volume of particles in motion per unit bed area (γ) was estimated from the number of moving particles averaged over the 1800 frames. The black sand transport rate was then calculated as $Q_{blk} = U_p\gamma$ [117, 30]. Assuming sand motion only occured in the top layer [40] and all sand motion followed the same probability distribution, the total sediment transport rate Q_s for a full bed of loose grains can be estimated as $Q_s = Q_{blk}/P_{blk}$. We calculated Q_s for different imaging durations and found that Q_s converged to a constant value at less than 30 seconds.

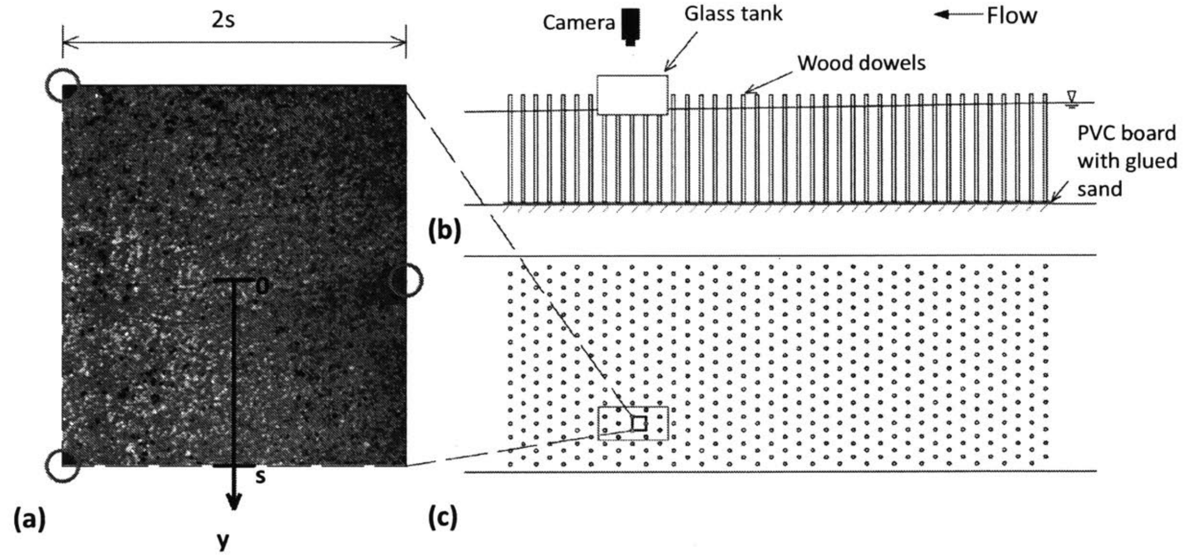

Figure 2-1: Experimental setup for tracking sediment trajectories

(a)The gray-scale image of the sand bed with superimposed trajectories of moving black sand (the red lines). The flow was right to left in the image. The red circles indicate the positions of dowels. LDV measurements were taken along the y axis defined, as shown in (a), at the mid-point of the unit cell of the repeating dowel pattern. $y = 0$ (the center of the image) was in line with the upstream dowel and mid-way between the upstream and downstream dowel rows. $y = s$ (lower edge of the image) was in line with the downstream dowel. (b) Side view of the test section. Vertical circular cylinders represent emergent stems of vegetation. The digital camera, with polarizing lens, was positioned above a glass tank with 15cm width and 30cm length in the horizontal plane. Several dowels under the tank were cut to allow the bottom of the tank to touch the water surface. (c) Top view of the test section shown in (b). The dowels were placed in a staggered pattern. The black box with red circles inside the blue box (the glass tank) represents the region captured by the camera.

For each vegetation solid volume fraction (ϕ) the sediment transport rate (Q_s) was measured at several channel velocities (U). A reference video with no black sand was also recorded for each flow condition and used to define the noise level. For each sediment size, the maximum noise value was used as the threshold criterion for sediment motion, Q_{s-crit}. For each vegetation density, an upper and lower bound for U_{crit} was chosen such that above the upper bound all the measured Q_s were larger than Q_{s-crit} and below the lower bound all the measured Q_s were smaller than Q_{s-crit}.

The mean between the upper and lower bound was chosen as U_{crit}.

The instantaneous velocity (u, w) was recorded at the critical condition $(U = U_{crit})$ using backscatter Laser Doppler velocimetry (LDV) at 1mm above the bed. Here (u, v, w) refer to the velocity along the x, y, z axes, corresponding to the steamwise, spanwise and vertical directions, respectively. The distance to the bed (1mm) was chosen to characterize the near bed flow condition because the fluid structures that trigger particle motion scale with sediment size [110]. The LDV probe (Dantec Dynamics) was mounted on a manually-driven positioning system, and the velocity was measured above the bed area where the sediment transport videos were recorded. For each velocity record, 10000 samples were collected at frequencies from 5 to 100 Hz. For the majority of the measurements, the sampling frequency was greater than twice the integral time scale from the autocorrelation function [73, 52], indicating that the sampling frequency was sufficient to capture the characteristics of the turbulence. The running average of turbulent statistics (including Reynolds stress and k_t) converged to stable values within 10000 velocity samples, consistent with a previous study [9].

Because the 2-D LDV only measured the vertical (w) and streamwise (u) velocity the turbulent kinetic energy was approximated as $k_t = (2\overline{u'^2} + \overline{w'^2})/2$. This approximation is justified because previous measurements have shown that within an emergent array the kinetic energy contributed by span-wise velocity fluctuation ($\overline{v'^2}$) is approximately equal to ($\overline{u'^2}$) [97]. For the vegetated cases, velocity was recorded along a lateral transect midway between rows at $y/s = 0$, 0.25, 0.5, 0.75 and 1, where s is the distance between dowels defined in Figure 2-1a. For the bare bed, the velocity was measured at two positions located laterally 5cm apart.

To show that the selected lateral positions captured the flow heterogeneity and provided representative spatial averages, we also measured the velocity for 3 minutes each at 18 vertical locations at the selected lateral positions. The average channel velocity estimated from these vertical profiles agreed with the flow meter reading within 10%, indicating that our selected lateral positions were adequate to characterize the flow heterogeneity. Furthermore, the LES results shown in figure (10) of [93] confirm that for sparse vegetation our lateral transect captured most of the flow heterogeneity.

2.4 Results: the turbulence-based model unified measurements in both bare and vegetated regions

Above a critical channel velocity, the sediment transport rate Q_s increased steadily with increasing U (Figure 2-2). The black dashed line denotes the noise threshold, $Q_{s-crit} = 0.01 mm^2/s$. Once sediment transport was initiated, the sediment transport rate was consistently higher for cases with model vegetation, compared to bare-bed, and at the same channel velocity the sediment transport rate generally increased with increasing vegetation solid volume fraction (ϕ).

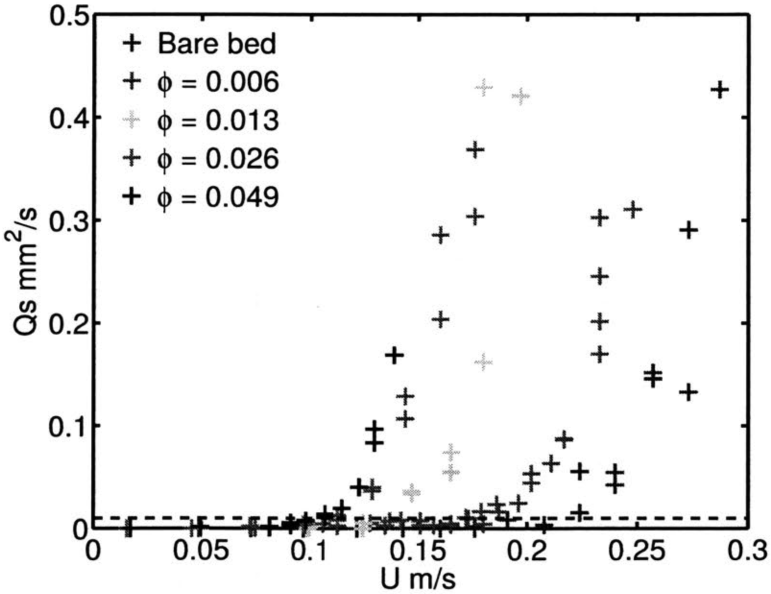

Figure 2-2: The transport rate of the mobile black sediment

Sediment transport rate, Q_s, versus channel velocity, U, for bare bed and four vegetation solid volume fractions (ϕ). The sediment size $d_s = 0.6$ to 0.85mm. The horizontal dashed line denotes the critical sediment transport rate, $Q_{s-crit} = 0.01 mm^2/s$ defined based on the noise threshold.

The incipient velocity (U_{crit}) was identified from the Q_s and U data as described in the Methods section and listed in Table2.1. For both grain sizes the value of U_{crit} decreased with increasing vegetation solid volume fraction (ϕ), with the greatest drop between the bare bed and the sparsest stem density (Figure 2-3). As expected, the values of U_{crit} were higher for the larger grain size. Hongwu et al. [39] estimated similar values of U_{crit} as a function of stem density for a grain size comparable to our smaller grain (data included in Figure 2-3).

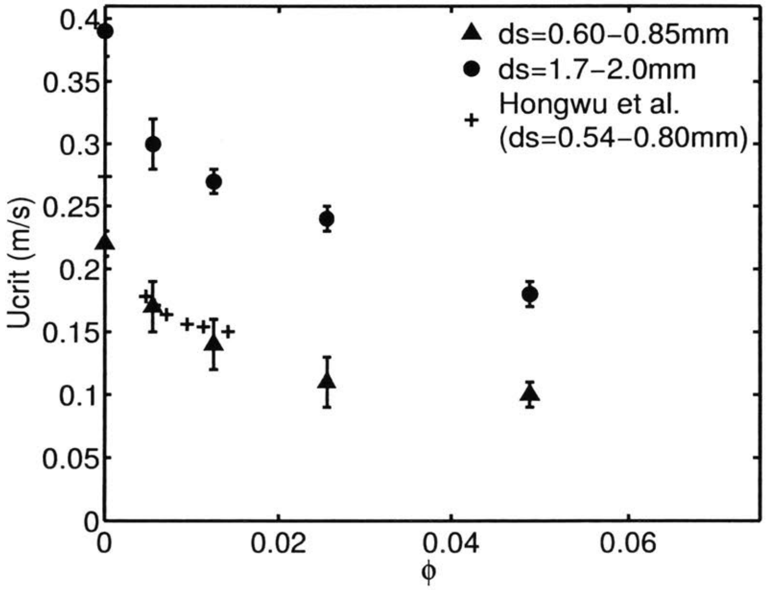

Figure 2-3: The critical velocity when sediment starts to move

The critical velocity for sediment motion, U_{crit}, versus vegetation solid volume fraction, ϕ. The filled triangles and circles with error bars are from the present study. The crosses are from [39] .

The spatially-averaged near-bed turbulence, k_t, was measured at the critical condition ($U = U_{crit}$) for each stem density (red symbols in Figure 2-4). To clarify overlapping points, the $x-$axis of measured k_t has been shifted right by 0.001. The lower and upper bound of measured k_t correspond to the value of k_t measured at U equal to the lower and upper bound of U_{crit}, respectively. Note that the spatial heterogeneity of k_t is much smaller than the error of k_t due to the uncertainty in U_{crit}. Within uncertainty the critical k_t was constant across all stem densities and bare bed.

To further support the turbulence model, the near-bed turbulence was also es-

Table 2.1: The measured critical velocity

Grain size ($d_s(mm)$)	ϕ	$Ucrit(m/s)$
0.60-0.85	0	0.22 ± 0.01
0.60-0.85	0.006	0.17 ± 0.02
0.60-0.85	0.013	0.14 ± 0.02
0.60-0.85	0.025	0.11 ± 0.02
0.60-0.85	0.049	0.10 ± 0.01
1.70-2.00	0	0.39 ± 0.02
1.70-2.00	0.006	0.30 ± 0.02
1.70-2.00	0.013	0.27 ± 0.01
1.70-2.00	0.025	0.24 ± 0.01
1.70-2.00	0.049	0.18 ± 0.01

timated using equation (2.2). The bed turbulence coefficient, C_b, was estimated from the measured bare-bed values of $k_t = 0.0012m^2/s^2$ and $U_o = 0.22m/s$, specifically $C_b = k_t/{U_o}^2 = 0.025$. Previous bare-bed studies have shown that the near-bed $k_t \approx 5.3\tau/\rho$ [91] and $\tau/\rho = C_f U^2$ [116]. For the conditions in this study ($h \approx 0.2m, d_s = 0.6 - 0.85mm$) $C_f \approx 0.0034$ (the Darcy-Weisbach friction relation in [45]), from which a predicted C_b is 0.02, agreeing with the measure value (0.025) within 25%. The value for C_D was approximated as 1.0 ± 0.5 for our experimental conditions ($600 < Re_d < 2500$) based on experimental data compiled in (Figure 4 in [13]). As ϕ increased, the contribution from the bed-generated turbulence k_{tb} (black squares in Figure 2-4) decreased significantly due to the decrease of U_{crit}. In contrast, the estimated contribution from vegetation-generated turbulence k_{tv} (black diamonds in Figure 2-4) increased with increasing ϕ because increasing the stem density provided more site for stem-wake turbulence generation (equation (2.1)). The predicted $k_{tb} + k_{tv}$ (equation (2.2), or the black circles) agreed with the measured k_t (the red symbols) within uncertainty, which both validated equation (2.2) and supported the hypothesis that the critical velocity was set by a threshold in near-bed k_t.

In Figure 2-5, the measured U_{crit}, normalized by the critical velocity for bare bed, U_o, is compared to the turbulence model described by equation (2.3). First, normalizing by U_o collapsed the two data sets (triangle and circles in Figure 2-5) within uncertainty, consistent with equation (2.3). Second, the model prediction

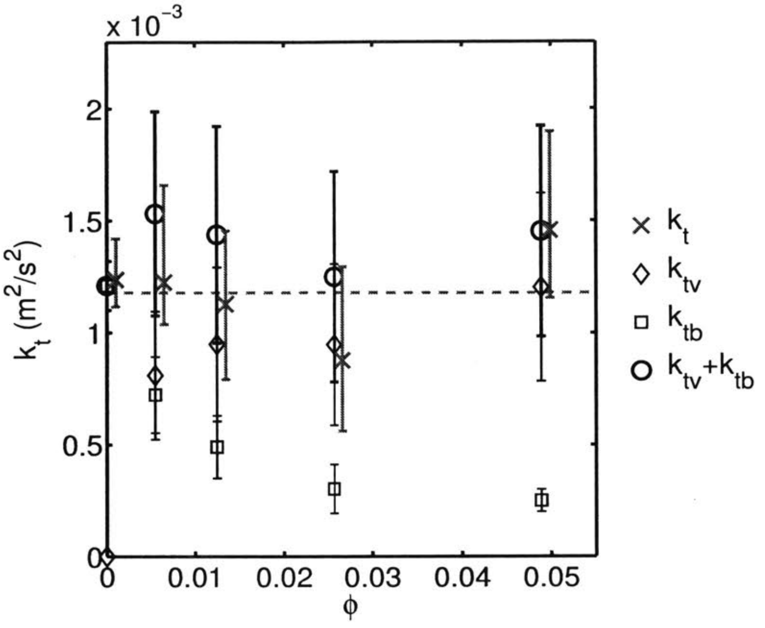

Figure 2-4: The turbulent kinetic energy at the critical condition

The measured turbulent kinetic energy (k_t, red symbols) and the predicted contribution from bed-generated turbulence k_{tb} and vegetation-generated turbulence k_{tv} at the critical condition ($U = U_{crit}$) for d_s = 0.6-0.85mm. The horizontal dashed line represents the average of measured k_t weighted by 1 over the error of k_t. The errors in k_{tb} and k_{tv} were contributed by the uncertainty in U_{crit} and C_D through standard propagation of error (e.g., [100]). For k_{tv}, the uncertainty in C_D contributed to the majority of its error.

with $C_b = 0.025$ and $C_D = 1$ is shown with a black dashed curve. The uncertainty in the predicted U_{crit}/U_o (gray shadow in Figure 2-5)) arose mainly from the uncertainty in $C_D(= 1 \pm 0.5)$. Both of our experimental data sets and the data from [39] (plus signs) agree with the turbulence model within uncertainty.

The model also has good agreement with the measurements of Widdows and Brinsley [115] which use natural vegetation (*Spartina anglica*) and natural mud with median grain size around $17.4 \pm 0.2 \mu m$ (diamonds in Figure 2-5). In their study, U_{crit} was defined as the velocity required to erode 10 grams of sediment per unit bed area, extrapolated from the suspended mass versus velocity curve. We estimated the solid volume fraction of *Spartina* (ϕ) as $\pi d^2 n/4$ with n denoting the number of stems per bed area, which is reported in the paper. *Spartina anglica* leaves are 1.5cm wide at the base and taper to a point, so that 0.75 cm was chosen as an estimation of d.

The values of U_{crit}/U_o versus ϕ (diamonds in Figure 2-5) agree with the turbulence model within uncertainty, indicating that the turbulence model can be extended to conditions with natural vegetation and fine sediment.

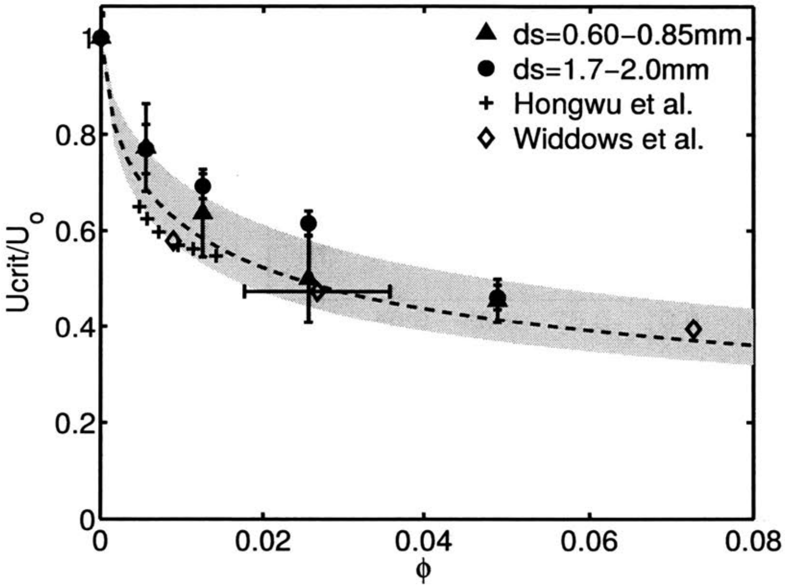

Figure 2-5: The turbulence-based model for the critical velocity of sediment transport

The incipient velocity of sediment motion U_{crit} normalized by the incipient velocity for a bare bed with the same sediment size (U_o). The black dashed curve with gray shadow represents the turbulence model (equation (2.3)) with $C_b = 0.025$ and $C_D = 1 \pm 0.5$. The black dashed curve corresponds to $C_D = 1$, and the upper and lower edge of the gray region represent $C_D = 0.5$ and 1.5, respectively. The horizontal bar for the diamond symbol at $\phi \approx 0.025$ represents the range of ϕ reported for this condition [115].

Finally, the difference between U_{crit} values measured with different grain sizes (Figure 2-3) is consistent with U_{crit} set by a critical value of k_t. As noted by previous researchers (e.g., [88]), let's assume that the eddy-induced pressure fluctuations initiate sediment motion. From Bernoulli's equation, the eddy-induced pressure fluctuation P_e should scale as $\rho {U_e}^2$, with U_e denoting the eddy velocity. Because ${U_e}^2$ is proportional to k_t, P_e is proportional to k_t. Consider a grain of size d_s, at the critical condition the lift force on the grain, $P_e \pi {d_s}^2/4$, approaches or exceeds the weight of the grain, $(\rho_s - \rho)\frac{1}{6}\pi {d_s}^3 g$, with ρ_s denoting the sand density and g denoting the gravitational acceleration. Therefore, the critical values of P_e and k_t increase linearly with d_s. Because k_t is proportional to U^2 for the same ϕ (equation (2.1)), U_{crit} is expected to increase linearly with $\sqrt{d_s}$. In the present study, the ratio of $\sqrt{d_s}$ for the two grain sizes was between 1.4 and 1.8, thus the ratio of U_{crit} was expected to be 1.6 ± 0.2. The corresponding ratio between the measured U_{crit} values (Figure 2-3) was $1.9 \pm 0.2(SD)$. The agreement within uncertainty between the measured U_{crit} ratio and the expected ratio further supports the turbulence model.

2.5 Conclusions

Turbulence has been recognized to play an important role in initiating sediment motion. In a vegetated channel, the generation of turbulence in the wakes of vegetation elements exceeds that associated with bed-shear, such that previous bare-bed sediment-transport models based on bed shear stress alone do not work. This study developed a model for the critical velocity for the onset of sediment transport (U_{crit}) based on a threshold value of near-bed turbulent kinetic energy (k_t). The model was validated by laboratory experiments conducted in both bare channels and channels with model vegetation of different densities. At the critical condition when sediment starts to move, the measured k_t was roughly a constant for all vegetation densities and bare bed (Figure 2-4), indicating that k_t may be a universal metric that can be used to predict sediment motion in both bare and obstructed channels. The new model correctly predicted U_{crit}, unifying both the bare-bed and vegetated channel measurements (Figure 2-5). Previous experimental data with natural vegetation and natural mud also agreed with the new model within uncertainty, suggesting that the model can be extended to predict U_{crit} in natural conditions.

Chapter 3

The bed load transport rate in vegetated channels

Previous studies have shown that current sediment transport models, based on the bed shear stress (τ), are not accurate for regions with vegetation. The present study demonstrated that the inaccuracy arises from the influence of vegetation-generated turbulence. Bed load transport rate, Q_s, and near-bed velocity were measured in a sediment-recirculating flume with model vegetation of different vegetation volume fractions (ϕ) and with bare sand-beds. At the same τ, the measured Q_s increased with increasing ϕ, suggesting that vegetation-generated turbulence, which also increased with increasing ϕ, was augmenting the bed load transport. At the same near-bed turbulent kinetic energy, k_t, the Q_s measured in both bare and vegetated channels agreed within uncertainty, suggesting that k_t may be a more universal predictor of Q_s than τ. A τ-based bed load transport model was reinterpreted as a k_t-based model. The new k_t-based model predicted the Q_s measurements for both bare and vegetated channels.[1]

---

[1] A version of this chapter is in revision for publication in *Geophysical Research Letters*, "Yang and Nepf. A turbulence-based bed-load transport model for bare and vegetated channels."

3.1 Background

Many coastal habitats, including around 50% of the world's wetlands, 30 to 50% of mangroves, and 50% of the seagrasses [124, 61], have been lost in the past several decades, and continue to be lost at rates of 1 to 7% per year [61]. Projects to restore these vegetated habitats, such as diverting sediments into the eroded areas, rely on the processes of sediment retention to regenerate new landscape, and simulations of landscape evolution used to assess and guide these restoration projects require accurate representations of sediment transport [27, 112, 96, 76]. Unfortunately, many restoration projects have failed, making it crucial to understand sediment transport in regions with vegetation [20, 102, 46]. However, existing sediment transport models, based on the time-averaged bed-shear stress (τ), were developed for regions without vegetation and have subsequently been shown to be inaccurate for regions with vegetation, so that there are currently no predictive models for sediment transport in regions with vegetation [118, 104].

We hypothesize that existing τ-based models fail within regions of vegetation because they do not account for vegetation-generated turbulence. Turbulence plays an important role in sediment transport [37, 69, 21]. A number of studies have observed that turbulent bursts or vortices occurring over a sediment particle can lift up the particle, initiating sediment transport [95, 75, 88]. The sediment lift-up has been attributed to the local, vertical adverse pressure, or the lift force, induced by the turbulent bursts [95, 109, 88]. Consistent with this hypothesis, Bagnold [4] observed that many sediment grains were ejected vertically from the bed and some were even ejected in the upstream direction, suggesting that sediment transport was initiated by a lift force rather than the horizontal drag force. Dittrich [22] and Zanke [123] analyzed velocity fluctuations and suggested that the lift force in turbulent flow is predominantly contributed by the pressure fluctuations induced by the turbulence passing above the grains, rather than by the force due to the curvatures of the streamlines over the grains, which is related to τ. For steady flow over a flat bed without vegetation, the lift force, the turbulent intensity, and τ are linearly related [25, 26], so that τ-based models capture the process of sediment motion. However, in regions with vegetation, the vegetation generates additional turbulence, so that the total turbulence intensity and associated lift force no longer scale with τ, which explains why the τ-based models do not work in vegetated regions.

In this paper, we propose using turbulent kinetic energy (k_t) to predict the sediment transport rate in vegetated regions, because the turbulence-induced lift force, a major control of the sediment transport, has been suggested to be proportional to the steam-wise velocity fluctuation squared [22, 123], which by definition scales with k_t. In addition, previous laboratory experiments have demonstrated that the incipient condition of sediment transport, including bed load and suspended load, in both bare (non-vegetated) and vegetated channels are determined by a critical value of k_t instead of τ [119, 105]. In this study, a τ-based sediment transport model developed for bare channels is reinterpreted as a k_t-based model. The reinterpreted k_t-based model predicted measurements in both bare and vegetated channels.

3.2 Methods

3.2.1 Experimental setup

The experiments were conducted in a flume that recirculates water and sediments separately (Figure 3-1). The flume has a $1m$ wide and $10m$ long test section. Experiments were carried out in channels without vegetation and with model vegetation of different solid volume fractions (ϕ) and at a range of channel-average velocity (Table 3.1). The flow rate Q was controlled by a centrifugal pump and measured with a flow meter with $1m^3/hour$ accuracy. The cross-sectional averaged velocity was calculated as $U = Q/(wh(1-\phi))$, with $w = 1m$ and h representing the flume width and water depth, respectively. To simulate emergent vegetation, aluminum dowels with diameter $d = 6.3mm$ were fixed in perforated PVC boards in a staggered pattern and extended through the water column. The number of dowels per bed area varied over the range $n = 0$ to 810 stems/m^2. The frontal area of the vegetation per unit

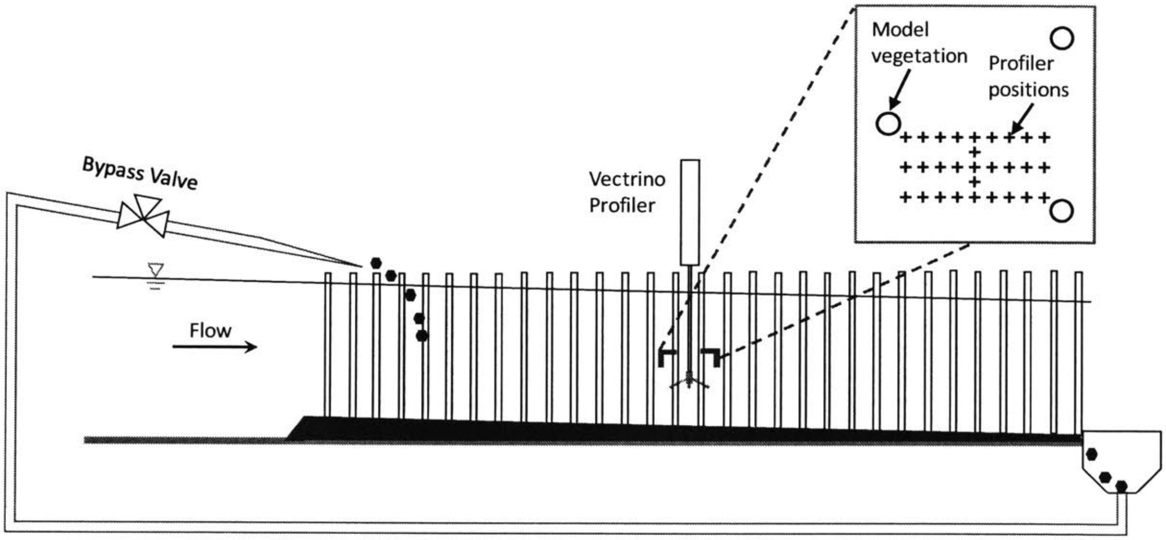

Figure 3-1: Schematic side-view of the sediment-recirculating flume

Vegetation was modeled by aluminum cylinders. The near-bed velocity was recorded at 2 cm from the bed using a Nortek Vectrino. Inset with blue edge: the top view of the region where the velocity measurements were made. 3-minute velocity measurements were recorded at multiple horizontal positions, indicated by the black pluses.

volume was $a = nd = 0$ to $5.1m^{-1}$ and the solid volume fraction of the vegetation was $\phi = (\pi/4)nd^2 = 0$ to 0.025, similar to conditions found in marshes [70]. The dowels covered the entire width of the flume and 3 meters in the streamwise direction for experiments 2.1-2.4, and 3.1-3.3. For cases 4.1-4.4, a large water surface slope was set up by the high vegetation solid volume fraction. To minimize the impact of the surface slope and associated flow depth variation on bed load measurements for these cases, the length of the streamwise vegetation coverage was reduced to 2 meters. The water depth h was measured in the middle of the vegetated region.

At the beginning of each experiment, a 4 cm-thick layer of sand was placed on top of the PVC boards and manually flattened. The sand grain density was $\rho_s = 2.65g/cm^3$ and the sand diameter was in the range 0.42 to 0.60 mm, with median grain size $d_s = 0.5mm$. Only bed load transport was observed during the experiment. Every few hours, the sand was bypassed from the sand-recirculating pipe through a three-way valve and collected in a mesh bag with $0.25mm$ holes. The bypass duration ranged from 1 to 10 minutes, chosen to be long enough to ensure that the volume of the collected sand was significantly larger than the background debris retained in the bag, which was $0.1g/s$, representing the lower-bound of measurable transport. For extremely large transport rate ($> 150g/s$), the sand filled the bag within 30 seconds, comparable to the time to switch the bypass valve on and off (around 10 seconds each way), thus measurements in this range had large uncertainties and were not included here. The collected sand was put into a container with water and a marked water line. The water surface in the container was maintained at the marked water line, and the dry mass of the sand was calculated from the mass difference of the container with and without the sand and the density difference between the sand (ρ_s) and the water (ρ). The instantaneous bed load transport rate, defined as the mass of sand passing through the channel cross section per time per unit width, was calculated as the mass of the collected sand divided by the time to collect the sand and the width of the flume. We repeated the bed load measurement at least 3 times until the cumulative average of all the instantaneous measurements varied by less than 10%. The average and standard error of all the measured instantaneous bed load transport rates were used to represent the equilibrium bed load transport rate and its uncertainty, $Q_s \pm \sigma_{Q_s}$ (Table 3.1).

3.2.2 Velocity measurements

A Nortek Vectrino profiler, an acoustic sensor that measures the velocity, was mounted on a manually driven positioning system placed in the middle of the vegetation (Figure 3-1). The positioning system allowed the profiler to move in the stream-wise (x), the lateral (y), and the vertical (z) directions. After the bed load transport rate reached equilibrium, the Vectrino profiler was used to measure the velocity at 0 to $4cm$ relative to the bed with $1mm$ vertical resolution and $100Hz$ sampling rate for 3 minutes at multiple horizontal locations. A typical distribution of measurement locations is indicated by the plus symbols in the inset of Figure 3-1, and the number of locations is listed in the second to last column of Table 3.1. Measurements at $2cm$

Table 3.1: The measured bed load transport rate and flow characteristics.

Case number	a $[m^{-1}]$	ϕ	U $[m/s]$	h $[m]$	$Q_s \pm \sigma_{Q_s}$ $[g/(m \cdot s)]$	$k_t \pm \sigma_{k_t}$ $[cm^2/s^2]$	$(\tau_{RS} \pm \sigma_{RS})/\rho$ $[cm^2/s^2]$
Bare channels							
1.1	0	0	0.42	0.12	0.36 ± 0.05	28 ± 1 (8)	3.9 ± 0.2
1.2	0	0	0.47	0.12	1.84 ± 0.08	46 ± 1 (34)	6.0 ± 0.2
1.3	0	0	0.65	0.12	24 ± 1	111 ± 11 (8)	14.7 ± 1.3
1.4	0	0	0.88	0.12	134 ± 8	205 ± 10 (8)	12.8 ± 1.6
1.5	0	0	0.33	0.12	0	NA	NA
Channels with emergent vegetation							
2.1	1.1	0.005	0.27	0.12	0.5 ± 0.1	19 ± 3 (24)	0.5 ± 0.2
2.2	1.1	0.005	0.30	0.12	2.5 ± 0.3	20 ± 2 (24)	0.2 ± 0.2
2.3	1.1	0.005	0.34	0.12	9 ± 1	32 ± 5 (24)	1.9 ± 0.5
2.4	1.1	0.005	0.43	0.12	68 ± 17	65 ± 8 (24)	6.2 ± 0.7
3.1	2.5	0.012	0.21	0.12	0.15 ± 0.02	17 ± 2 (27)	0.5 ± 0.1
3.2	2.5	0.012	0.24	0.12	2.6 ± 0.5	22 ± 2 (27)	0.1 ± 0.1
3.3	2.5	0.012	0.28	0.12	9.4 ± 0.6	45 ± 5 (27)	2.0 ± 0.6
4.1	5.1	0.025	0.21	0.10	1.3 ± 0.1	20 ± 2 (23)	0.5 ± 0.1
4.2	5.1	0.025	0.23	0.10	2.9 ± 0.3	42 ± 4 (23)	0.1 ± 0.1
4.3	5.1	0.025	0.27	0.10	17 ± 1	46 ± 4 (23)	1.0 ± 0.2
4.4	5.1	0.025	0.31	0.10	41 ± 2	51 ± 5 (23)	1.6 ± 0.3
4.5	5.1	0.025	0.17	0.10	0	NA	NA

Note that the number in parenthesis indicates number of spatial positions at which velocity measurements were made.

relative to the time-mean bed elevation was used to represent the near-bed condition, because the velocity data at less than $2cm$ from the mean bed had low correlation and low signal to noise ratio (SNR) due to the interference of the bed with the acoustic signal of the profiler.

The local near-bed turbulent kinetic energy ($(\overline{u'^2}+\overline{v'^2}+\overline{w'^2})/2$) and the local near-bed Reynolds stress ($\rho(-\overline{u'w'})$), with u', v', w' denoting the velocity fluctuations in the steam-wise, lateral, and vertical directions, respectively, were calculated from the velocity measurements made with the Nortek Vectrino profiler at each location (plus signs in the inset of Figure 3-1). For each velocity record, the time-averaged velocity, turbulent kinetic energy, and Reynolds stress converged to a stable value within 3 minutes. The spatial average and standard error of the local turbulent kinetic energy and local Reynolds stress measured at different horizontal locations were denoted as $k_t \pm \sigma_{k_t}$ and $\tau_{RS} \pm \sigma_{RS}$, respectively. We calculated the spatial-average from the local turbulent kinetic energy using an increasing number of measurement positions, and found that k_t converged to a stable value at fewer than the total number used in the present study (listed in the second to last column of Table 3.1), indicating that the number of velocity measurements was adequate to capture the spatial variation of the turbulent kinetic energy.

3.3 Results

The equilibrium bed load transport rate (Q_s) and the channel-average velocity (U) are listed in Table 3.1. For the same U, cases with greater vegetation solid volume fraction (ϕ) generally had higher Q_s. Because the spatially-averaged Reynolds stress (τ_{RS}) is commonly used as an approximation of the mean bed shear stress (τ) to estimate Q_s for bare channels [74, 6], we first explored if τ_{RS} could predict Q_s in channels with vegetation. As suggested by Einstein [26], the dimensionless bed load transport rate, Q_{s*}, was defined as the ratio of the bed load transport rate Q_s to the product of ρ_s, the fall velocity of the grains (ω_0), and the grain size,

$$Q_{s*} = \frac{Q_s}{\rho_s \omega_0 d_s}. \tag{3.1}$$

The particle fall velocity ω_0 can be approximated from the Rubey's equation [83],

$$\omega_0 = [\sqrt{\frac{2}{3} + \frac{36\nu^2}{(\rho_s/\rho - 1)gd_s^3}} - \sqrt{\frac{36\nu^2}{(\rho_s/\rho - 1)gd_s^3}}]\sqrt{(\rho_s/\rho - 1)gd_s}. \tag{3.2}$$

For coarse sand and gravel (e.g. $d_s > 1mm$), $\omega_0 \approx \sqrt{(\rho_s/\rho - 1)gd_s}$ such that $Q_{s*} \approx \frac{Q_s}{\rho_s\sqrt{(\rho_s/\rho-1)gd_s^3}}$. The dimensionless Reynolds stress τ_{RS*} represents the ratio of the horizontal force, $\tau(\pi d_s^2/4) \approx \tau_{RS}(\pi d_s^2/4)$, exerted on the grain to the submerged weight of the grain, $(\rho_s - \rho)g(\pi d_s^3/6)$, namely

$$\tau_{RS*} = \frac{\tau_{RS}}{(\rho_s - \rho)gd_s}, \tag{3.3}$$

with g represents the gravitational acceleration. The measured Q_{s*} versus the measured τ_{RS*} is plotted in Figure 3-2. Measurements from the present study are plotted as triangles, and measurements from [118] using similar sediment and model vegetation are plotted with circles. Note that while the present study measured bed load directly, Yager and Schmeeckle [118] inferred Q_{s*} from the difference in the pixels of sequenced images recorded by a camera. In addition, [118] covered a smaller range of channel velocity U than the present study. The black curve represents the τ-based Einstein-Brown bed load transport model [26, 8]:

$$Q_{s*} = \begin{cases} 2.15e^{-0.391/\tau_*}, & \tau_* < 0.18 \\ 40\tau_*^3, & 0.18 < \tau_* < 0.52. \end{cases} \tag{3.4}$$

For bare channels ($\phi = 0$, dark blue triangles), measured Q_{s*} agreed with the Einstein-Brown model within uncertainty for the majority of the cases. However, for vegetated channels, the measurements did not agree with the τ-based model and instead the measured Q_{s*} were consistently higher than the model prediction, suggesting that

τ_{RS*} cannot be used to estimate Q_{s*} for regions with vegetation.

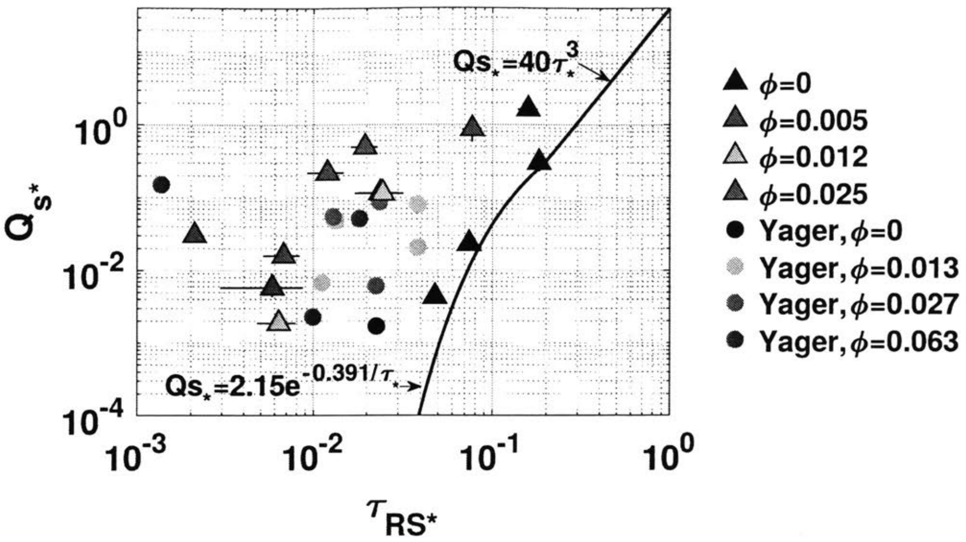

Figure 3-2: The measured dimensionless bed load transport rate

Plot of the dimensionless bed load transport rate Q_{s*} versus the dimensionless Reynolds stress τ_{RS*} measured in the present study (triangles) and in [118] (circles). The black curve represents the Einstein-Brown model [26, 8].

The disagreement between the Q_{s*} versus τ_{RS*} measurements in vegetated channels and the τ-based model suggested that either the τ-based model does not work for regions with vegetation or τ_{RS} can not be used to approximate τ in regions with vegetation. To examine the later, we estimated τ for vegetated channels using the bed shear stress model developed under similar experimental conditions [121]:

$$\tau = \begin{cases} \frac{4\rho\nu U}{d}, & Re_d = \frac{Ud}{\nu} < \frac{4}{C_f} \\ \rho C_f U^2, & Re_d \geq \frac{4}{C_f}. \end{cases} \tag{3.5}$$

Here ν and C_f represent the kinematic viscosity of water and the bed drag coefficient, respectively. Re_d is the stem Reynolds number. Yang et al. [121] showed that when $Re_d < \frac{4}{C_f}$, model vegetation suppresses the viscous sub-layer thickness to the stem radius ($d/2$) such that τ was set by d and ν. When $Re_d \geq \frac{4}{C_f}$, which represents conditions in this study, the viscous sub-layer thickness is already smaller than $d/2$ such that the impact of vegetation on τ is negligible and $\tau = \rho C_f U^2$. C_f can be estimated from the sediment size d_s and water depth h using the semi-empirical equation [113, 45]:

$$C_f = \frac{1}{[5.75log(2h/d_s)]^2}. \tag{3.6}$$

For the sediment sizes and range of water depth h used in the present study and in [118], equation 3.6 predicts $C_f = 0.004 \pm 0.001$. In the bare channel (cases 1.1 to 1.4), the near-bed Reynolds stress measurements suggested $C_f = \tau/U^2 = \tau_{RS}/U^2 = 0.0030 \pm 0.0015$, consistent with equation 3.6. $C_f = 0.0030 \pm 0.0015$ was used in this study.

The measured dimensionless bed load transport rate Q_{s*} versus the dimensionless bed shear stress ($\tau_* = \tau/((\rho_s - \rho)gd_s)$) estimated from equation 3.5 is plotted in Figure 3-3(a). For bare channels (dark blue triangles), Q_{s*} versus τ_* agreed with previous bare channel measurements (small black dots) and the Einstein-Brown model (solid curve) within uncertainty, confirming the validity of our measurements and the τ estimation. However, for cases with vegetation (symbol color indicates ϕ using color bar), at conditions with similar τ_*, the measured Q_{s*} was consistently larger than the bare channel measurements and the Einstein-Brown model. Moreover, at conditions with the same τ_*, as vegetation solid volume fraction ϕ increased (symbol color shifting from dark blue to light blue to orange to red), the measured Q_{s*} also increased, and the deviation from the Einstein-Brown model became larger. The increase of Q_{s*} with increasing ϕ supported the idea that the vegetation-generated turbulence, which also increased with ϕ, facilitated the bed load transport.

To test our hypothesis that k_t was a more important control on Q_s in vegetated conditions, we converted the τ-based Einstein-Brown model into a k_t-based model. Specifically, the Einstein-Brown model was originally developed for bare channels, for which $k_t = \tau/(0.19\rho)$ [91, 6]. Using this conversion, the τ-based Einstein-Brown model was reinterpreted as a k_t-based model by substituting $\tau_* = 0.19k_{t*}$ into equation 3.4:

$$Q_{s*} = \begin{cases} 2.15e^{-2.06/k_{t*}}, & k_{t*} = \frac{k_t}{(\rho_s/\rho - 1)gd_s} < 0.95 \\ 0.27k_{t*}^3, & 0.95 < k_{t*} < 2.74. \end{cases} \tag{3.7}$$

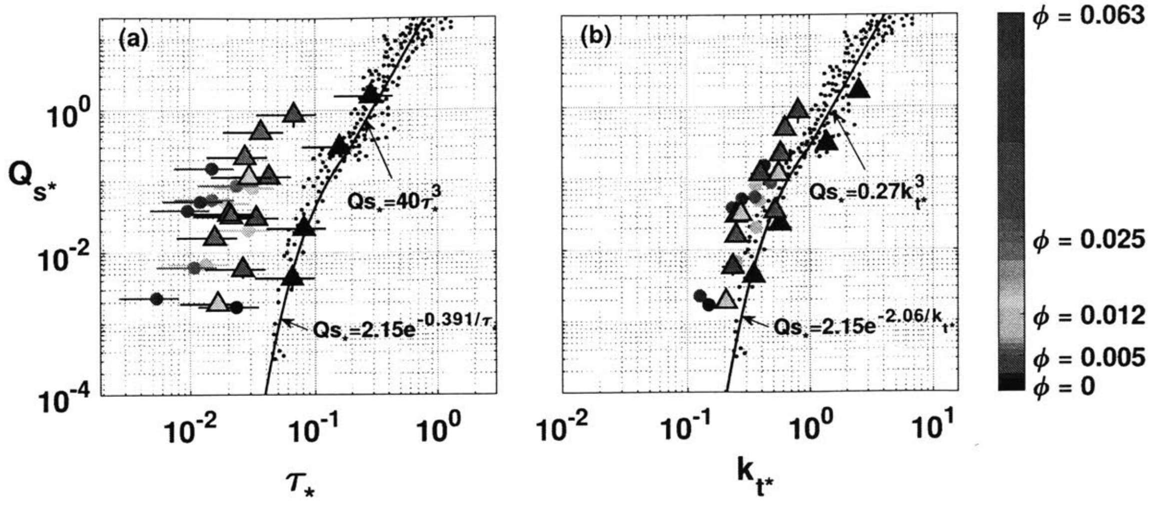

Figure 3-3: Comparison of τ-based model and k_t-based model

Comparison of (a) τ-based model and (b) k_t-based model. Measurements from the present study and [118] are indicated by triangles and circles, respectively. k_{t*} was measured at $2cm$ and $5mm$ from the bed in the present study and [118], respectively. The black curves represent the τ-based model (equation 3.4) and the reinterpreted k_t-based model (equation 3.7) in (a) and (b). The black dots are previous measurements in bare channels compiled in Fig. 9.2 of [45].

with Note that the τ-based model (equation 3.4) and the k_t-based model (equation 3.7) are equivalent for bare channels. However, we expect that in channels with vegetation, only the k_t-based model will work, because vegetation provides an additional source of turbulence such that $\tau_* = 0.19k_{t*}$ does not apply. The converted k_t-based model, together with the Q_{s*} versus k_{t*} measurements, are plotted in Figure 3-3(b). The black dots represent the same data shown as black dots in Figure 3-3(a) with the x-axis converted to $k_{t*} = \tau_*/0.19$. Under conditions with the same k_{t*}, Q_{s*} for both bare channel cases and cases with different vegetation solid volume fractions agreed within uncertainty, suggesting that k_{t*} is a more universal predictor of Q_{s*} than τ_*. Furthermore, The root-mean-square deviation ($RMSD = \sqrt{\sum_{j=1}^{m}(log(\hat{Q}_{s*}) - log(Q_{s*}))^2/m}$, with m, $\hat{Q}_{s*}$, and Q_{s*} representing the total number of measurements, the model estimation of the bed load transport rate, and the bed load transport rate measurements, respectively) was 0.8 for the k_t-based model, much smaller than the $RMSD$ for the τ-based Einstein-Brown model (= 5.2), confirming that the k_t-based model provided a better framework for predicting Q_s.

3.4 Discussion

3.4.1 Comparing the influence of U and k_t on bed load transport

Previous experiments have shown that the velocity of moving sediment grains increases with increasing channel velocity U [53, 82], so that we expect U to also play a role in setting Q_s, which isn't clearly evident in the k_t model described above. To further explore why k_t provided the dominant control on Q_s, we looked into previous measurements of individual grain velocity from [119]. Yang et al. [119] recorded the trajectories of loose black sand grains distributed over a layer of glued brown-sand. Cases with and without the same model vegetation considered here were investigated. The velocity of individual sand grains was measured and used to calculate the mean streamwise velocity of all moving sand grains, U_p. The volume of sediment in motion per unit bed area, γ, was also tracked (Table 3.2 and 3.3). The bed load transport rate is then $Q_s = U_p\gamma$ [117, 30]. For both bare and vegetated channels, U_p varied roughly linearly with U, and both spanned a factor of 3 across range of conditions considered here (Figure 3-4(a)). In contrast, over the same range of U, γ changed by over 2 orders of magnitude (Figure 3-4(b)). Roseberry et al. [82] also observed that γ increased more quickly with U than did U_p. Both the present study and [82] suggest that Q_s $(= U_p\gamma)$ is predominantly controlled by γ, which increases two-fold faster with U than does U_p. Further, at conditions with the same U, γ increased with increasing ϕ (Figure 3-4(b)). Specifically, at $U = 0.22 m/s$, γ increased by over 2 orders of magnitude between $\phi = 0$ and 0.012, suggesting that the vegetation-generated turbulence, which increased with ϕ, significantly enhanced the number of particles in motion. The turbulent kinetic energy k_t was calculated from U using the near-bed turbulent kinetic energy model (equation4.4) [119]. In contrast, at the same $\sqrt{k_t}$, γ for different ϕ varied within one order of magnitude and with no dependence of γ on ϕ (Figure 3-4(c)), suggesting that the number of sediment grains in motion correlated more closely with k_t than with the mean velocity U. This was consistent with the observation that the number of particles in motion fluctuates in response to near-bed turbulence [82] and is also supported by the idea that the transport of sediments is triggered by turbulent bursting events [95, 75]. To summarize, [119]'s data showed that Q_s $(= U_p\gamma)$ is predominantly controlled by γ and that γ scales with k_t, which suggests that Q_s has a stronger dependence on k_t than U, consistent with the observations presented in Figure 3-3.

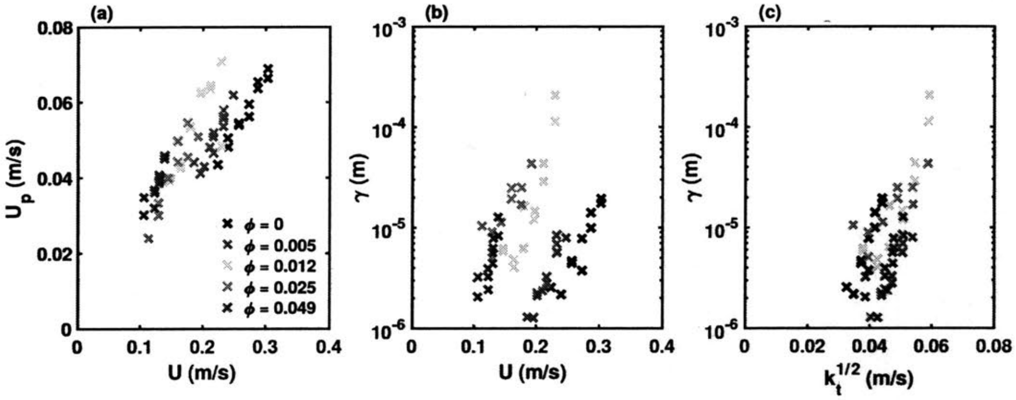

Figure 3-4: Statistics of moving sediment grains

Variation in (a) the mean stream-wise velocity of moving sediments, U_p, and (b) the volume of particles in motion per unit bed area, γ, as a function of channel velocity, U, and (c) γ as a function of the square root of the turbulence kinetic energy, $\sqrt{k_t}$.

3.4.2 Implications for sediment transport modeling

Observations reported here have shown that at the same channel velocity (U) and time-mean bed shear stress (τ), vegetation-generated turbulence increased the sediment transport (Figure 3-3). However, vegetation also exerts a drag which, for the same bed slope or surface slope, reduces U, which would tend to decrease k_t and thus Q_s [72]. To take into account these two competing effects that vegetation has on sediment transport, we predicted the bed load transport rate Q_s under the same energy slope (s), e.g., the surface slope due to tidal forcing or the same bed slope, but increasing vegetation solid volume fraction (ϕ).

Table 3.2: The sediment transport statistics – Part 1

ϕ	$U(m/s)$	$U_p(m/s)$	$\gamma \times 10^6(m)$
0.000	0.22	0.043	2.6
0.000	0.24	0.051	2.2
0.000	0.24	0.048	2.2
0.000	0.26	0.054	4.4
0.000	0.26	0.054	4.7
0.000	0.27	0.059	7.8
0.000	0.27	0.056	3.8
0.000	0.29	0.064	9.9
0.000	0.29	0.065	14.1
0.000	0.30	0.069	19.4
0.000	0.30	0.066	17.5
0.005	0.20	0.043	2.3
0.005	0.22	0.046	3.3
0.005	0.23	0.054	5.6
0.005	0.23	0.058	8.5
0.005	0.19	0.044	1.3
0.005	0.20	0.041	1.3
0.005	0.20	0.043	2.1
0.005	0.21	0.048	2.4
0.005	0.22	0.052	2.8
0.005	0.22	0.051	2.9
0.005	0.23	0.056	5.8
0.005	0.23	0.056	6.9
0.005	0.25	0.062	8.0
0.012	0.15	0.040	6.2
0.012	0.15	0.039	5.8
0.012	0.17	0.043	4.1
0.012	0.17	0.043	4.9
0.012	0.18	0.053	6.3
0.012	0.18	0.054	16.3
0.012	0.20	0.062	12.0
0.012	0.20	0.063	14.7
0.012	0.21	0.064	28.9
0.012	0.21	0.065	43.8
0.012	0.23	0.071	207.7
0.012	0.23	0.048	112.8

The turbulent kinetic energy k_t was calculated from U using the near-bed turbulent kinetic energy model (equation4.4). Note that two experiments were conducted under the same condition (same ϕ and same U) for most of the conditions and the results of both of them were plotted in Figure 3-4, representing the range or the uncertainty of our measurements.

Table 3.3: The sediment transport statistics – Part 2

ϕ	$U(m/s)$	$U_p(m/s)$	$\gamma \times 10^6(m)$
0.025	0.11	0.024	10.5
0.025	0.13	0.033	5.1
0.025	0.13	0.030	9.0
0.025	0.14	0.040	11.3
0.025	0.16	0.050	19.5
0.025	0.16	0.044	24.8
0.025	0.18	0.055	25.0
0.025	0.18	0.046	16.8
0.025	0.19	0.051	42.8
0.049	0.12	0.036	2.4
0.049	0.13	0.041	4.4
0.049	0.13	0.039	5.7
0.049	0.14	0.045	8.2
0.049	0.11	0.035	3.2
0.049	0.11	0.030	2.1
0.049	0.12	0.032	3.3
0.049	0.12	0.037	3.9
0.049	0.13	0.040	7.8
0.049	0.13	0.039	6.3
0.049	0.14	0.046	12.8

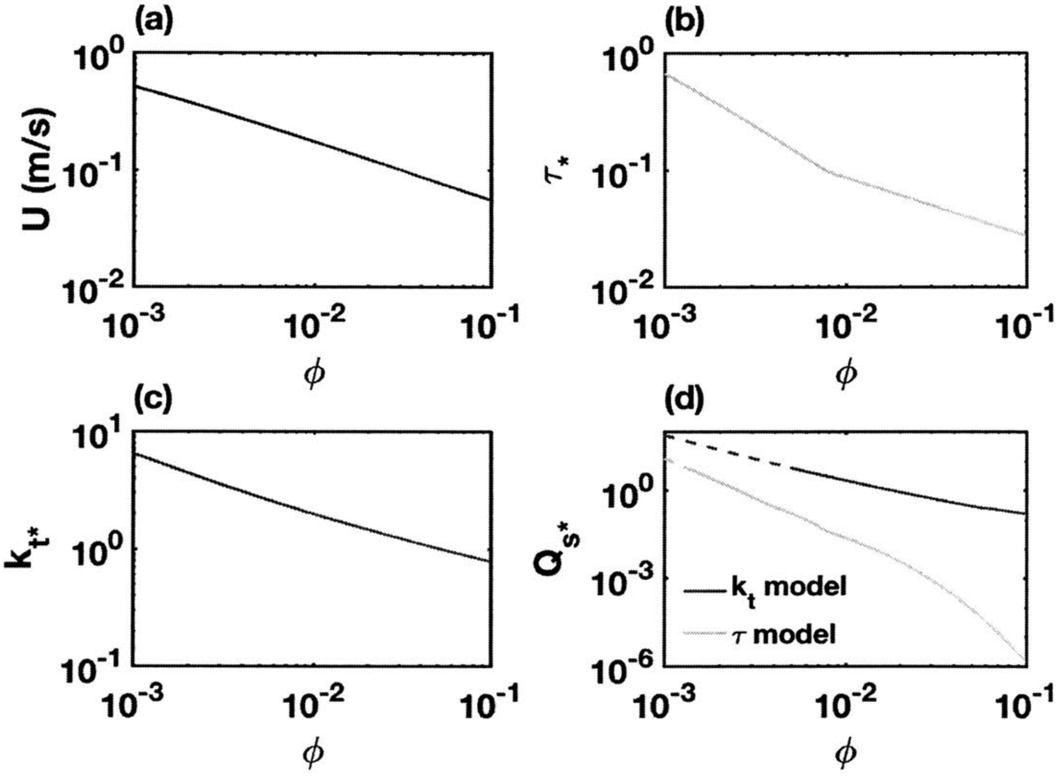

Figure 3-5: Example bedload transport in a salt marsh

(a) The channel velocity U, (b) dimensionless bed shear stress τ_*, (c) dimensionless turbulent kinetic energy k_{t*}, and (d) the dimensionless bed load transport rate Q_{s*}, estimated from both the τ-based models and the k_t-based models, as a function of the vegetation solid volume fraction ϕ, for conditions with the same energy slope (s).

First, U was calculated from the force balance between the energy gradient, the bed shear stress, and the vegetative drag, $\rho ghs = \rho C_f U^2 + \rho \frac{1}{2} C_D a h U^2$ [72], so

$$U = \sqrt{\frac{ghs}{C_f + C_D a h/2}}. \tag{3.8}$$

Here the vegetation drag coefficient C_D was approximated as 1 [72]. For a typical marsh with vegetation diameter $d = 1cm$, water depth $h = 0.2m$, energy slope $s = 0.002$, and mean sediment size $d_s = 0.05mm$ [122, 70, 107], the channel velocity U for different vegetation solid volume fractions ($\phi = 0.001 - 0.1$) is shown in Figure 3-5(a). Under the same energy slope, U decreased with increasing ϕ due to the vegetation drag. The dimensionless bed shear stress (τ_*) and the dimensionless near-bed turbulent kinetic energy (k_{t*}) were then calculated from U for each ϕ using equation 3.5 and the following k_t equation described in [119], respectively.

$$k_t = \frac{C_f}{0.19} U^2 + 0.9 C_D^{2/3} \phi^{2/3} U^2, \tag{3.9}$$

with $C_D = 1$ the vegetation drag coefficient. Because of the pronounced reduction in U, τ_* and k_{t*} also decreased with increasing ϕ (Figure 3-5(b) and (c)). Q_{s*} was calculated from τ_* and k_{t*} using the τ-based model (equation 3.4) and the k_t-based model (equation 3.7), respectively. As shown in Figure 3-5(d), both the τ-based model and the k_t-based model predict a decrease in Q_{s*} with increasing ϕ, consistent with the general observation of reduced sediment transport in vegetated regions [1, 15]. However, the Q_{s*} predicted by the τ-based model was consistently smaller than that predicted by the k_t-based model. For example, at $\phi = 0.01$ (a typical marsh condition), Q_{s*} predicted by the k_t-based model was 2 orders of magnitude larger than that predicted by the τ-based model, illustrating that the vegetation-generated turbulence has a significant influence on Q_s in marshes.

3.5 Conclusions

Sediment transport models based on the mean bed-shear stress, τ, underestimated the sediment transport rate, Q_s, measured in channels with model vegetation, and this was attributed to the vegetation-generated turbulence. Based on this, a reinterpretation of the τ-based Einstein-Brown equations as k_t-based equations was proposed. Experimental measurements in a sediment-recirculating flume and measurements from a previous study verified the k_t model. Specifically, the k_t-based model predicted the measured Q_s for both bare and vegetated channels. The new model will improve the prediction of sediment transport and retention within vegetated habitats, which in turn should improve landscape restoration planning.

Chapter 4

Impact of vegetation on bed load transport rate and bedform characteristics

The impacts of aquatic vegetation on bed load transport rate and bedform characteristics were quantified in a sediment-recirculating flume with model vegetation. Under conditions with the same velocity, the measured bed load transport rate, Q_s, increased significantly with increasing vegetation solid volume fraction, and this was attributed to vegetation-generated turbulence. Conventional models based on mean bed shear stress, τ, could not capture these trends. However, the measured Q_s in both bare and vegetated channels collapsed when plotted against near-bed turbulent kinetic energy, k_t. A re-interpretation of the τ-based Einstein-Brown model in terms of k_t was verified with measured Q_s from the present study and several previous studies. Ripples were observed in channels with model vegetation. For low vegetation solid volume fraction ($\phi \leq 0.012$), the ripple wavelength was constrained by stem spacing and the ripple height increased with increasing ϕ. However, at the highest vegetation solid volume fraction ($\phi = 0.025$), the ripple height was comparable to the grain size, indicating that a plane bed had formed. The ripple migration speed and the bed load flux associated with the migrating ripples increased with increasing vegetation solid volume fraction for $\phi \leq 0.012$. However, the fraction of the bed load flux carried by migrating ripples decreased with increasing ϕ, suggesting that vegetation facilitated the formation of sheet flow.

4.1 Background

Aquatic vegetation provides tens of trillion of dollars worth of ecosystem services annually [14]. For example, by damping storm surge during hurricane Sandy, coastal wetlands reduced flood damage by $625 million [68]. In the Mississippi Valley, wetlands provide $250 million worth of benefits annually by absorbing nitrogen [43]. Unfortunately, large areas of the aquatic vegetation, including half of the world's wetlands [124], have been lost in the past several decades, and continue to be lost globally at rates of 0.7 to 7% annually [61]. One reason for the loss of vegetated landscape is erosion [7, 28]. Diverting sediments to regions of erosion is a common strategy to restore the landscapes [66, 7, 76], yet a lot of restoration projects have failed [20], because the process of sediment transport in regions with vegetation is poorly understood [76, 28].

Current sediment transport models, based on the time-mean bed shear stress τ, were developed for unidirectional flow without obstacles, and have been shown to be inaccurate for regions with obstacles, such as bedforms and vegetation [69, 118]. This is likely because the τ-based models do not take into account the turbulence generated by the obstacles, and turbulence has been shown to play an important role in sediment transport [95, 69, 75, 60, 21, 85, 84]. For example, the instantaneous sediment transport rate in a tidal channel was observed to be intermittent, linked to the bursting patterns of the near-bed turbulence [37]. Sumer et al. [94] conducted flume experiments with obstacles and observed a five-fold increase in Q_s with 20% increase in k_t at conditions with the same τ, suggesting that k_t may play a more important control on Q_s than τ. Flow visualization has revealed that turbulent bursts can lift up sediment grains, initiating sediment transport [95, 75]. The sediment lift-up and subsequent transport were attributed to local, turbulence-induced, vertical adverse pressure, or lift force [95, 109, 123]. Supporting this, Bagnold [4] observed some sediment grains ejected from the bed vertically and even in the upstream direction, indicating that the lift force played a more important role in sediment transport than the bed shear stress, which would tend to produce trajectories in the downstream direction. Based on turbulent flow measurements, Zanke [123] and Dittrich [22] argued that the lift force is mainly contributed by the pressure fluctuations associated with turbulent eddies passing over the sediment, which would be correlated with turbulence intensity, rather than the lift force associated with the curvature of streamlines over individual grains, which would be correlated with the time-mean bed shear stress.

For unidirectional flow without obstacles, which here will be called a bare channel flow, the bed shear stress is the only external force that affects the near-bed turbulence [109], and τ and the turbulent kinetic energy (k_t) are linearly related [91, 38], such that the role of turbulence in sediment transport is implicitly incorporated in the τ-based sediment transport models. For channels with other external forces, such as bed-form-induced drag or vegetative drag, the direct relationship between k_t and τ breaks down, because these additional forces also contribute to turbulence generation [99, 93], which may explain why a τ-based model can not predict sediment transport rate in places with obstacles. For example, Sumer et al. [94] placed pipes and grids in the upper water column to generate additional turbulence, and they noted that at conditions with the same τ, a 20% increase in turbulence level produced a five-fold increase in sediment transport rate. Further, Nelson et al. [69] conducted experiments in a channel with simulated bedforms and observed that sweeps and ejections, which contribute equally to τ, produce significantly different sediment transport rates. Therefore, if the relative contributions of sweeps and ejections change, such as in some nonuniform flow conditions, Q_s could increase even though τ decreases. Based on these observations, Nelson et al. [69] argued that the τ-based methods are not accurate for non-uniform flow conditions, for which the turbulent statistics do not scale with τ. Both Sumer et al. [94] and Nelson et al. [69] suggest that the reason the τ-based models are not accurate for places with obstacles is because they cannot account for the additional sources of turbulence.

Recent studies demonstrated that in regions with vegetation sediment transport is more closely correlated with turbulent kinetic energy than with the time-mean bed stress [119, 120, 103, 106]. Yang et al. [119] showed that k_t is a better predictor of the threshold of sediment motion than τ, and that the critical level of near-bed turbulence is the same in bare and vegetated channels. Similarly, Tinoco and Coco [103, 106] showed that resuspension of sediment within an array of model vegetation is better predicted by a metric based on the turbulence intensity than bed shear stress. Yang and Nepf [120] proposed a re-interpretation of traditional τ-based bedload transport models into k_t-based models. The k_t-based models were validated with measurements of turbulence and bed load in both bare channels and channels with model emergent vegetation of different solid volume fractions (ϕ). In this study, we expand our understanding of the influence of vegetation on bed-load transport. First, a prediction for vegetated-generated turbulence was validated for channels with mobile sand beds, which enabled the incorporation of a wider range of previous bed load transport measurements into the assessment of a k_t-based model for bed load transport. Second, the impact of vegetation on ripple characteristics and the relationship between the ripple migration rate and the bedload transport rate were explored.

4.2 Methods

4.2.1 Laboratory setup

A horizontal flume with a $w = 1m$ wide and 10m long test section recirculated water and sand separately (Figure A-2). The model vegetation consisted of aluminum cylinders with diameter $d = 6.3mm$ placed in a staggered pattern on perforated PVC boards and extending above the water surface. This diameter was consistent with stem diameters found in marsh plants and young floodplain trees [70, 58]. When present, the model vegetation covered the entire flume width. The number of cylinders per unit bed area was in the range $n = 0$ to 810 stems/m^2, producing a vegetation frontal area per unit volume, $a = nd$, in the range 0 to $5.1m^{-1}$, and a vegetation solid volume fraction $\phi = \pi n d^2/4 = 0$ to 0.025, which are typical values for marshes

[70]. Trials with different flow rates without vegetation and with vegetation of different ϕ were carried out to test the impact of vegetation on bed load transport rate (Table 4.1). For cases 2.1-2.4, and 3.1-3.3, the vegetation covered 3 meters in the streamwise direction. For cases 4.1-4.4, cases with the largest ϕ, the vegetation covered only 2 meters in the streamwise direction to minimize the impact of the large surface slope set up by the high vegetation drag and thus large variation in flow depth. The average channel velocity was calculated as $U = Q/(wh(1-\phi))$, with the flow rate Q controlled by a centrifugal pump and measured by a flow meter with $1m^3/hour$ accuracy, and the water depth h measured in the middle of the vegetation patch.

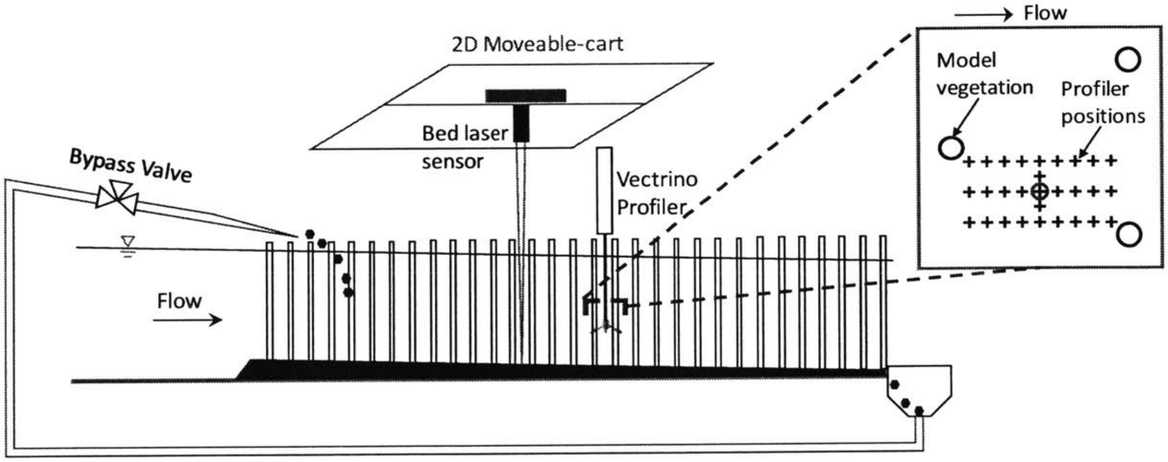

Figure 4-1: The setup of the sediment recirculating experiments

The brown color indicates the sand bed. At the beginning of each experiment, the sand bed was flat and level. After an experiment, the sand bed was sloped (as shown here) and ripples had formed (not shown). The blue-edged inset shows the top view of the velocity measurement positions (the crosses) relative to dowel positions (the black circles). 3-minute velocity measurements taken at positions indicated by the crosses were used to calculate the spatially-averaged turbulent kinetic energy and Reynolds stress. To quantify ripple characteristics, bed elevation as a function of time was recored by the Vectrino profiler at the position marked with a red circle.

Sand with density $\rho_s = 2.65g/cm^3$ and diameter 0.42 to $0.60mm$ (median grain size $d_s = 0.5mm$) was placed on the PVC boards and flattened manually. No sand was observed in suspension. The instantaneous bed load transport rate was defined as the dry mass of the sediment passing an unit cross-sectional width per time. The sediment recirculation pipe included a three-way valve that allowed sediment to be diverted to a mesh collection bag with 0.25mm holes. The valve was engaged for periods of 1 to 10 minutes, depending on the sediment transport rate, and chosen to ensure that the volume of the collected sand was smaller than the capacity of the mesh bag. The collected sand was placed into a container filled with water, and the water surface was maintained at a marked line. The dry mass of the collected sand was calculated as the increase in the total mass of the container divided by the density difference between sand and water and multiplied by the sand density. The bed load transport rate was measured for a minimum of 3 times until the cumulative average of all measurements changed by less than 10% with increasing number of measurements. The equilibrium bed load transport rate and its uncertainty, $Q_s \pm \sigma_{Q_s}$, were estimated as the average and the standard error of all the measured instantaneous bed load transport rates.

4.2.2 The velocity and topography measurements

The instantaneous velocity in the streamwise, spanwise, and vertical direction (u, v, and w, respectively), was measured by a Nortek Vectrino profiler at $100Hz$ sampling rate for 3 minutes at multiple locations in the middle of the vegetation patch (shown with crosses in the inset of Figure A-2). Measurements at $2cm$ from the mean bed were used to represent the near-bed condition, because measurements at less than $2cm$ from the bed had low correlations and signal to noise ratios (SNR) due to interference of the bed with the sensor acoustic signal. The velocity measurements was filtered using the methods proposed in [34, 111, 42], and at the measurement position ($2cm$ from the bed) the correlation was larger than 80% and $SNR > 30dB$. The local turbulent kinetic energy was defined as $(\overline{u'^2} + \overline{v'^2} + \overline{w'^2})/2$, with u', v', and w' denoting the instantaneous deviation from the time-mean velocity and $(\overline{})$ denoting the time-average. The local Reynolds stress was defined as $\rho(-\overline{u'w'})$ with ρ the water density. The time-averaged velocity, turbulent kinetic energy, and Reynolds stress converged to a stable value within 3 minutes, indicating that a 3-minute record was sufficient to capture the desired velocity statistics. The spatially-averaged turbulent

Table 4.1: The measured bed load transport rate and flow characteristics.

Case number	a $[m^{-1}]$	ϕ	U $[m/s]$	h $[m]$	$Q_s \pm \sigma_{Q_s}$ $[g/(m \cdot s)]$	$k_t \pm \sigma_{k_t}$ $[cm^2/s^2]$	$(\tau_{RS} \pm \sigma_{RS})/\rho$ $[cm^2/s^2]$
Bare channels							
1.1	0	0	0.42	0.12	0.36 ± 0.05	28 ± 1 (8)	3.9 ± 0.2
1.2	0	0	0.47	0.12	1.84 ± 0.08	46 ± 1 (34)	6.0 ± 0.2
1.3	0	0	0.65	0.12	24 ± 1	111 ± 11 (8)	14.7 ± 1.3
1.4	0	0	0.88	0.12	134 ± 8	205 ± 10 (8)	12.8 ± 1.6
1.5	0	0	0.33	0.12	0	NA	NA
Channels with model emergent vegetation							
2.1	1.1	0.005	0.27	0.12	0.5 ± 0.1	19 ± 3 (24)	0.5 ± 0.2
2.2	1.1	0.005	0.30	0.12	2.5 ± 0.3	20 ± 2 (24)	0.2 ± 0.2
2.3	1.1	0.005	0.34	0.12	9 ± 1	32 ± 5 (24)	1.9 ± 0.5
2.4	1.1	0.005	0.43	0.12	68 ± 17	65 ± 8 (24)	6.2 ± 0.7
3.1	2.5	0.012	0.21	0.12	0.15 ± 0.02	17 ± 2 (27)	0.5 ± 0.1
3.2	2.5	0.012	0.24	0.12	2.6 ± 0.5	22 ± 2 (27)	0.1 ± 0.1
3.3	2.5	0.012	0.28	0.12	9.4 ± 0.6	45 ± 5 (27)	2.0 ± 0.6
4.1	5.1	0.025	0.21	0.10	1.3 ± 0.1	20 ± 2 (23)	0.5 ± 0.1
4.2	5.1	0.025	0.23	0.10	2.9 ± 0.3	42 ± 4 (23)	0.1 ± 0.1
4.3	5.1	0.025	0.27	0.10	17 ± 1	46 ± 4 (23)	1.0 ± 0.2
4.4	5.1	0.025	0.31	0.10	41 ± 2	51 ± 5 (23)	1.6 ± 0.3
4.5	5.1	0.025	0.17	0.10	0	NA	NA

Numbers in parentheses indicate the number of spatial positions at which velocity measurements were made.

kinetic energy and its uncertainty, $k_t \pm \sigma_{k_t}$, were estimated from the average and the standard error of the local turbulent kinetic energy measured at multiple locations (pluses in the inset of Figure A-2). The number of measurement locations is listed in the parentheses in Table 4.1. We verified that the number of spatial locations was sufficient to capture the spatial average of k_t, by increasing the number of measurements until k_t converged to a stable value. Similarly, the spatially-averaged Reynolds stress and its uncertainty, $\tau_{RS} \pm \sigma_{RS}$, were estimated from the average and the standard error of the local Reynolds stress.

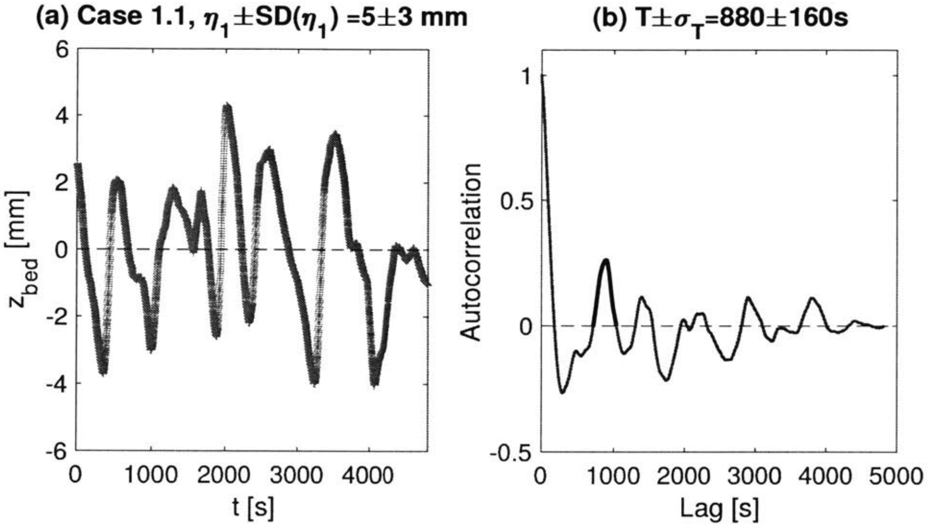

Figure 4-2: Bed elevation in the time domain

(a) The instantaneous bed elevation relative to the mean, z_{bed}, for case 1.1 measured using the Vectrino for 80 minutes. The average and the standard deviation of the ripple height, $\eta_1 \pm SD(\eta_1)$, are indicated in the title, and the number of identified ripples is listed in Table 4.2. (b) The ripple migration period and its uncertainty, $T \pm \sigma_T$, were identified from the time lag corresponding to the first positive peak at lag greater than zero in the autocorrelation of z_{bed} (highlighted by a black curve above).

Bedforms with wave heights less than $2cm$ were observed, and we classified them as ripples because the water surface was not affected by the bedforms. To quantify the ripple height and migration period, the instantaneous bed elevation was recorded at $1Hz$ sampling rate by the Vectrino profiler in the middle of the diagonal between two dowels (the red circle in the inset of Figure A-2). The duration of the measurements, ranging from 30 minutes to 2 hours, was chosen to be much longer than the ripple migration period (Table 4.2). The ripple crest to trough distance was identified using MATLAB findpeaks function (Figure 4-2(a)). The average and the standard deviation of all the identified crest-trough heights, $\eta_1 \pm SD(\eta_1)$, were listed in Table 4.2. The uncertainty in η_1 was estimated as the standard error of the crest-trough heights, i.e., $\sigma_{\eta_1} = SD(\eta_1)/\sqrt{m_1}$, with m_1 denoting the number of the identified crest-trough heights (Table 4.2). The ripple migration period (T) was determined from time lag corresponding to the first positive peak at lag greater than zero in the autocorrelation of the bed elevation (Figure 4-2(b)). The uncertainty in T, denoted as σ_T, was estimated as half the range of the first positive lobe (the black color part of the curves in Figure 4-2(b).

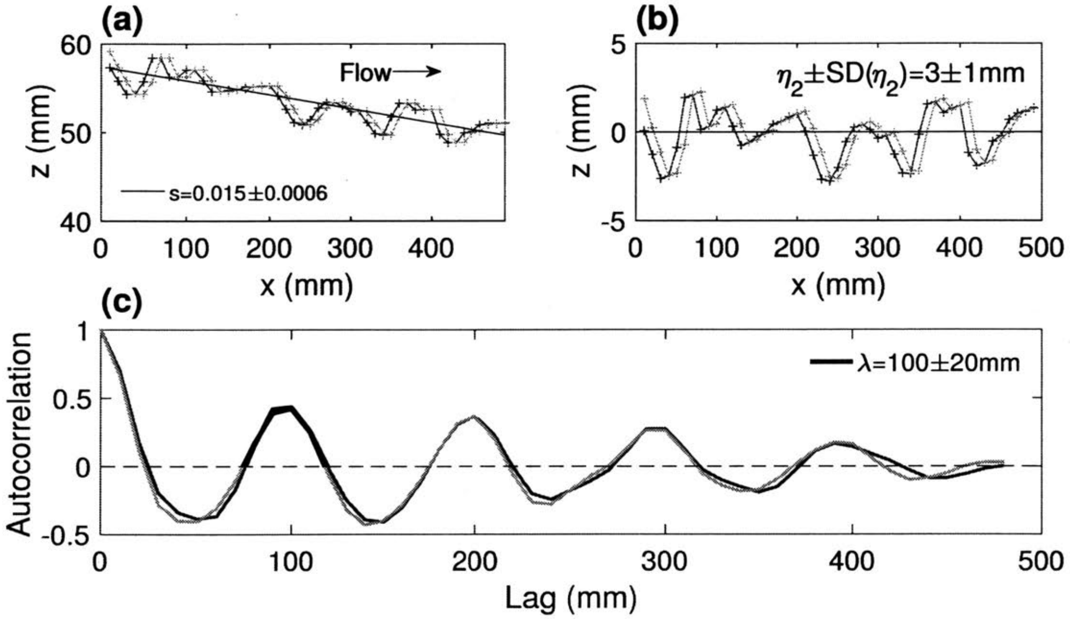

Figure 4-3: Bed elevation in the spatial domain

(a) Two bed topography profiles, indicated with different colors, measured 5cm apart for case 3.1. Note that the x and y-axes are plotted in different scales. (b)The ripple only profiles obtained by subtracting the fitted mean bed slope (the black line in Figure(a)) from the bed topography profiles. (c) The spatial autocorrelation of the ripple profiles with x-axis representing the lag in distance. The first autocorrelation peak at lag greater than zero, indicated by black overlay curve, was used to estimate the ripple wavelength λ. The uncertainty σ_λ was half the range of the positive lobe.

At the end of each experiment, the flow was stopped to scan the bed topography using a Keyence laser sensor mounted on a 2D moving system (Figure A-2). Two bed elevation profiles are shown in Figure 4-3(a). The two profiles were measured $5cm$ apart laterally and covered $50cm$ in the streamwise direction. The ripple profiles (Figure 4-3(b)) were obtained by subtracting the bed slope (the fitted black line in Figure 4-3(a)) from the bed elevation profiles. The ripple crest to trough distance was identified using MATLAB findpeaks function and the number of identified ripples is listed in (Table 4.2). The ripple height and its spatial variation, $\eta_2 \pm SD(\eta_2)$, were estimated as the average and the standard deviation of the identified crest-trough distances (Table 4.2). The uncertainty in η_2 was estimated as the standard error of the identified crest-trough distances, namely $\sigma_{\eta_2} = SD(\eta_2)/\sqrt{m_2}$, with m_2 denoting the number of identified ripples from the laser topography profiles (Figure 4-3(b)). The ripple wavelength λ, was determined from the distance lag corresponding to the first positive peak with greater than zero lag in the spatial autocorrelation of the bed elevation (Figure 4-3(c)). The uncertainty of the ripple wavelength, σ_λ, was half the range associated with the chosen peak, shown with black curve. For cases 4.1-4.4 with the densest vegetation, the laser signal experienced too much interference from the closely-spaced dowels, so η_2 and λ could not be determined.

4.2.3 Estimation of bed shear stress

For bare channels, the time-averaged bed shear stress, τ, was estimated from the quadratic stress law [113, 79, 45]:

$$\tau = \rho C_f U^2, \tag{4.1}$$

C_f was estimated from the sediment size d_s and water depth h using the semi-empirical equation [113, 45]:

$$C_f = \frac{1}{[5.75log(2h/d_s)]^2}. \tag{4.2}$$

For vegetated channels, τ was estimated using the model proposed by Yang et al. [121] that incorporates the impact of the vegetation on bed shear stress:

$$\tau = \begin{cases} \frac{4\rho\nu U}{d}, & Re_d = \frac{Ud}{\nu} < \frac{4}{C_f} \\ \rho C_f U^2, & Re_d \geq \frac{4}{C_f}. \end{cases} \tag{4.3}$$

Here ν is the kinematic viscosity of water, and $Re_d = Ud/\nu$ is the stem Reynolds number. As described in [121], at $Re_d < \frac{4}{C_f}$ the stem-generated turbulence depresses the viscous sub-layer thickness to stem radius ($d/2$). For $Re_d \geq \frac{4}{C_f}$ the sub-layer thickness is already smaller than $d/2$ such that stem-generated turbulence has a negligible impact on the bed shear stress. In this study, $Re_d \geq \frac{4}{C_f}$ such that the impact of vegetation on τ is negligible and equation 4.1 applies to all cases.

4.3 Results

4.3.1 The turbulent kinetic energy in vegetated channels

For vegetated channels, Yang et al. [119] proposed the following model based on [99] for near-bed turbulent kinetic energy, k_t, capturing the sum of the bed-generated turbulence and vegetation-generated turbulence,

$$k_t = \frac{C_f}{0.19}U^2 + 0.9C_D^{2/3}\phi^{2/3}U^2, \tag{4.4}$$

with C_D the vegetation drag coefficient. However, Yang et al. [119] only validated the model for a stationary (glued) sand bed. Measurements in the present study were used to test whether equation 4.4 can provide good estimates of near-bed k_t over a mobile bed of sand. The measured k_t is plotted against the k_t estimated from equation 4.4 in Figure 4-4. The triangles, circles, and squares are measurements from the present study, [118], and [119], respectively. The vegetation drag coefficient C_D used in equation 4.4 was estimated from the following empirical equation validated by direct force measurements in a similar laboratory setup with an array of emergent, steel cylinders [49],

$$C_D = 1.8\zeta Re_d^{-3/50}[1 + 0.45ln(1 + 100\phi)] \times (0.8 + 0.2F - 0.15F^2). \tag{4.5}$$

The coefficient ζ depends on the spatial configuration of the cylinders, and $\zeta = 0.8$ for a staggered array. The Froude number $F = U/\sqrt{gh}$ with g the gravitational acceleration. Note that no calibration was done to improve the fit of the measured k_t to equation 4.4. The good agreement between the measured k_t and the estimated k_t confirmed the validity of equation 4.4 in conditions with a mobile bed of sand.

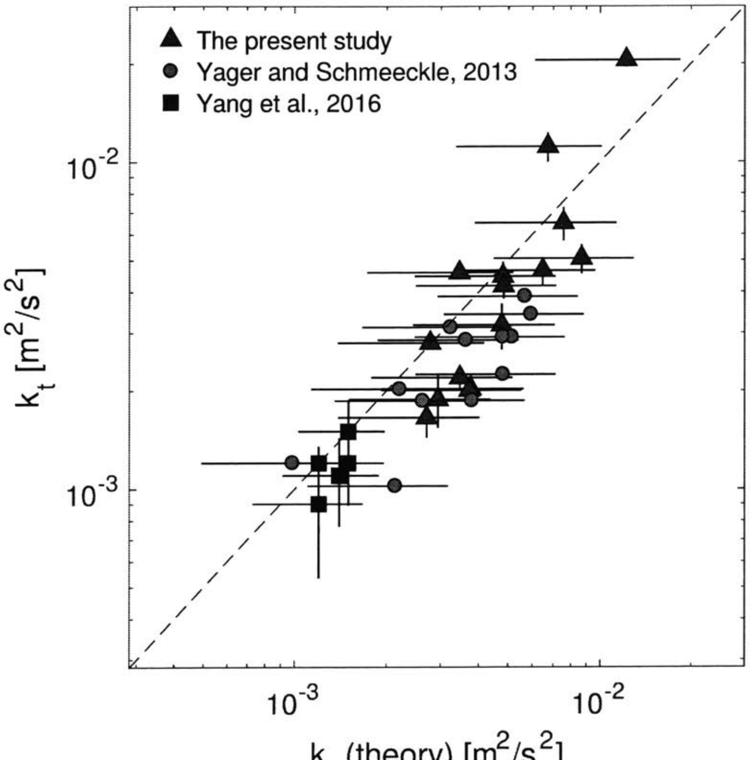

Figure 4-4: The measured near-bed turbulent kinetic energy

The measured turbulent kinetic energy, k_t, versus k_t(theory) estimated from equation 4.4. The present study (blue triangles) and Yang et al. [118] (red circles) have a mobile sand bed. Yang et al. [119] (black squares) had a glued sand bed. The horizontal error bars represent the uncertainty in the predicted k_t due to the uncertainties in C_f and C_D, which were estimated based on the range of flow conditions used in each data set. The vertical error bars represent the spatial variation in the measured k_t (Table 4.1).

4.3.2 Models for bed load transport rate in vegetated channels

As suggested by Einstein [26], the dimensionless bed load transport rate, Q_{s*}, was defined as the ratio of the bed load transport rate Q_s to the product of ρ_s, the fall velocity of the grains (ω_0), and the grain size,

$$Q_{s*} = \frac{Q_s}{\rho_s \omega_0 d_s}. \tag{4.6}$$

The particle fall velocity ω_0 can be approximated from the Rubey's equation [83],

$$\omega_0 = [\sqrt{\frac{2}{3} + \frac{36\nu^2}{(\rho_s/\rho - 1)gd_s^3}} - \sqrt{\frac{36\nu^2}{(\rho_s/\rho - 1)gd_s^3}}]\sqrt{(\rho_s/\rho - 1)gd_s}. \tag{4.7}$$

For coarse sand and gravel (e.g. $d_s > 1mm$), $\omega_0 \approx \sqrt{(\rho_s/\rho - 1)gd_s}$ such that $Q_{s*} \approx \frac{Q_s}{\rho_s\sqrt{(\rho_s/\rho-1)gd_s^3}}$. The dimensionless bed shear stress, τ_*, represents the ratio of the horizontal force $\tau(\pi d_s^2/4)$ exerted on the grain to the submerged weight of the grain, $(\rho_s - \rho)g(\pi d_s^3/6)$,

$$\tau_* = \frac{\tau}{(\rho_s - \rho)gd_s}. \tag{4.8}$$

Similarly, the dimensionless near-bed turbulent kinetic energy, k_{t*}, represents the ratio of the turbulence induced lift force, which is proportional to $\rho k_t(\pi d_s^2/4)$ [22, 123], to the submerged weight of the grain.

$$k_{t*} = \frac{k_t}{(\rho_s/\rho - 1)gd_s}. \tag{4.9}$$

Bed load transport measured in five different data studies are included in Figure 4-5. The triangles are measurements from the present study, for which Q_{s*} was measured as the mass of the recirculating sediment, τ_* was estimated from equation 4.3, and k_{t*} was measured. The small black dots are previous measurements, Q_{s*} and τ_*, in bare channels reported in [45], and for which k_{t*} was estimated based on the empirical relation for bare channels, $k_{t*} = \tau_*/0.19$ [91, 38]. The circles represent measurements by Yager and Schmeeckle [118] in which Q_{s*} was inferred from digital image analysis of the bed, τ_* was estimated from equation 4.3, and k_{t*} was measured. The present study covered a wider range of velocity than considered in [118]. The squares and the diamonds represent bed load transport rate estimated from the mass of the sediment leaving a flume [48] and the mass of sediment fed into a sediment-feed flume [44], respectively. Note that no near-bed velocity measurements were given in [48] and [44], so that both τ_* and k_{t*} were estimated from reported channel velocity and vegetation characteristics using equation 4.3 and equation 4.4, respectively.

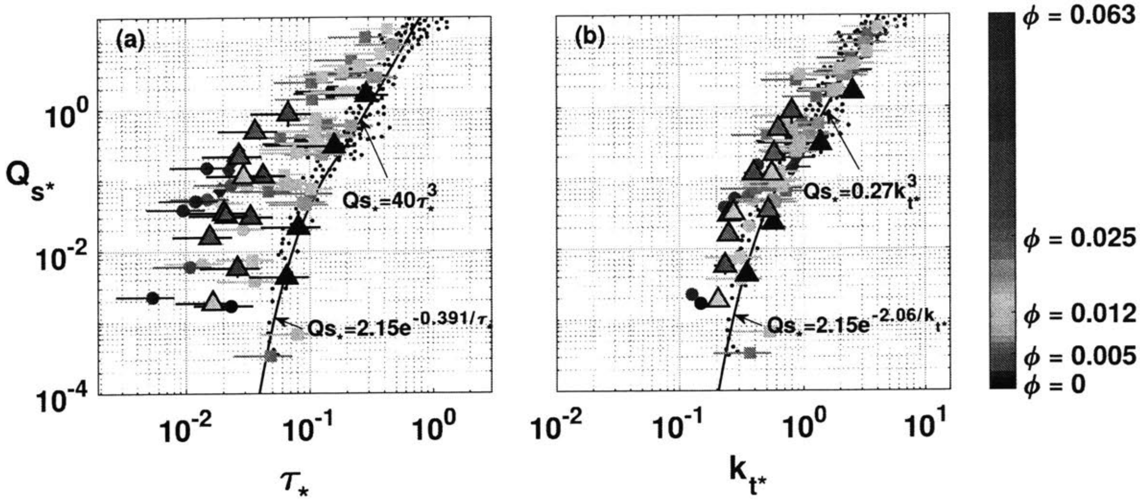

Figure 4-5: The sediment transport rate measurements and models

Comparison of a τ-based sediment transport model and the k_t-based sediment transport model. (a) The measured dimensionless bed load transport rate (Q_{s*}) versus the dimensionless bed shear stress (τ_*) for different vegetation solid volume fractions (ϕ). Measurements from the present study, [118], [44], and [48] are indicated by triangles, circles, diamonds, and squares, respectively. The small black dots are bare channel measurements compiled in [45] and the black curves represent the τ-based Einstein-Brown model given in equation 4.10 [26, 8]. (b) The measured Q_{s*} versus the dimensionless turbulent kinetic energy, k_{t*}. The black curves represent the k_t-based model given in equation 4.11.

For the same τ_*, the measured Q_{s*} increased for higher vegetation solid volume fraction ϕ (Figure 4-5(a)), suggesting that the vegetation-generated turbulence enhanced bed load transport. The measurements in bare channels (dark blue triangles in Figure 4-5) agreed with the Einstein-Brown semi-empirical τ-based bedload transport model [26, 8]:

$$Q_{s*} = \begin{cases} 2.15e^{-0.391/\tau_*}, & \tau_* < 0.18 \\ 40\tau_*^3, & 0.18 < \tau_* < 0.52. \end{cases} \tag{4.10}$$

However, measurements in vegetated channels were consistently higher than this model. In contrast, the measured bed-load transport collapsed more closely together when plotted versus near-bed turbulent kinetic energy (Figure 4-5(b)). In light of this, Yang and Nepf [120] suggested a re-interpretation of the Einstein-Brown equation in terms of near-bed k_t. The Einstein-Brown equation is based on measurements in a bare channel, for which $k_t = \tau/0.19\rho$ [91, 38]. Using this conversion, the Einstein-Brown equation can be re-written as

$$Q_{s*} = \begin{cases} 2.15e^{-2.06/k_{t*}}, & k_{t*} < 0.95 \\ 0.27k_{t*}^3, & 0.95 < k_{t*} < 2.74. \end{cases} \tag{4.11}$$

The k_t version of the Einstein-Brown relation is shown by a solid line in Figure 4-5(b). There was good agreement between this relation and all the measurements, suggesting that k_t is a better predictor of bed-load transport because it works in both bare and vegetated channels and across a wide range of vegetation solid volume fractions.

Note that for the cases shown in Figure 4-5, the median grain size ($d_s = 0.5$ to $5.9mm$) was smaller than or comparable to stem diameter ($d = 2$ to $13mm$). We caution that the k_t-based model (equation 4.11) may not work for channels with d_s several times larger than d. For a sparse array (d smaller than the average surface-to-surface distance between stems), which is the case for the present study and most salt marshes, the characteristic size of the eddies is approximately equal to d [99]. As the spatial extent of the turbulence-induced pressure is of the same order of magnitude as the eddy size [88], if d_s is several times larger than the eddy size or d, then only a small portion of the grain will be exposed to the lifting pressure, which means that the total lift force on the grain will not be proportional to the horizontal projected area of

Table 4.2: The measured ripple characteristics.

Case number	$\lambda \pm \sigma_\lambda$ $[m]$	$\eta_1 \pm SD(\eta_1)$ (# of ripples) $[mm]$	$\eta_2 \pm SD(\eta_2)$ (# of ripples) $[mm]$	$T \pm \sigma_T$ $[s]$	U_{ripple} $\pm\sigma_{U_{ripple}}$ $[m/s]$	$Q_{s_{ripple}}$ $\pm\sigma_{Q_{s_{ripple}}}$ $[g/(m \cdot s)]$
Bare channels						
1.1	0.25 ± 0.03	5 ± 3 (5)	2 ± 1 (4)	880 ± 160	0.28 ± 0.06	1.0 ± 0.3
1.2	0.28 ± 0.05	11 ± 2 (9)	4 ± 3 (6)	660 ± 200	0.42 ± 0.15	3.2 ± 1.1
1.3	NA	11 ± 4 (16)	NA	38 ± 4	*NA*	*NA*
1.4	0.29 ± 0.09	13 ± 2 (7)	6 ± 5 (6)	40 ± 20	7 ± 4	60 ± 40
Channels with model emergent vegetation						
2.1	0.21 ± 0.06	3 ± 1 (3)	3 ± 1 (6)	2400 ± 300	0.09 ± 0.03	0.18 ± 0.07
2.2	0.16 ± 0.04	3 ± 1 (8)	3 ± 1 (7)	630 ± 160	0.25 ± 0.09	0.5 ± 0.2
2.3	0.17 ± 0.04	7 ± 3 (17)	7 ± 3 (4)	110 ± 50	1.6 ± 0.8	7 ± 4
2.4	0.17 ± 0.03	12 ± 5 (52)	10 ± 3 (6)	42 ± 11	4 ± 1	33 ± 11
3.1	0.10 ± 0.02	2 ± 1 (4)	3 ± 1 (8)	4600 ± 800	0.02 ± 0.01	0.03 ± 0.01
3.2	0.10 ± 0.02	4 ± 1 (2)	6 ± 2 (8)	2300 ± 500	0.04 ± 0.01	0.12 ± 0.04
3.3	0.16 ± 0.06	6 ± 2 (52)	6 ± 3 (5)	200 ± 110	0.8 ± 0.5	3 ± 2
4.1	*NA*	2 ± 1 (12)	NA	1800 ± 300	*NA*	*NA*
4.2	*NA*	2 ± 1 (7)	NA	1500 ± 500	*NA*	*NA*
4.3	*NA*	3 ± 1 (47)	NA	29 ± 12	*NA*	*NA*
4.4	*NA*	2 ± 1 (55)	NA	30 ± 20	*NA*	*NA*

Because cases 1.5 and 4.5 have zero sediment transport rate, bed topography was not measured for these two cases. λ and η_2, measured by the laser sensor, were not reported for case 1.3, because for this case η_2 was comparable to water depth, indicating that this laser measurement was contaminated by the reflection of the laser signal from the water surface. For cases 4.1-4.4 with the densest vegetation, the laser signal experienced too much interference from the closely-spaced dowels, so η_2 and λ could not be determined.

the grain ($(\pi/4)d_s^2$) and the nondimensionalization (equation 4.9) can not represent the ratio of the lift force to the submerged weight of the grain.

4.3.3 The ripple characteristics and migration rate

The ripple height sampled at one point over time, $\eta_1 \pm SD(\eta_1)$, agreed with the ripple height identified from the scanned topography, $\eta_2 \pm SD(\eta_2)$, within uncertainty (Table 4.2). Because the number of ripples sampled by the Vectrino was larger than the number of ripples scanned by the laser sensor (Table 4.2), the analyses will focus on η_1. For bare channels ($\phi = 0$), the ripple height (η_1) increased between the channel velocity 0.42 and $0.47 m/s$, but was constant within measurement uncertainty for a channel velocity of $0.47 m/s$ and above (Figure 4-6(a)). This is consistent with a previous experimental study over a bare bed that showed that ripple height first increased with increasing U, but at higher velocity, as the ripples started to be washed out, ripple height decreased with increasing U [18]. For our bare channel cases ($\phi = 0$), ripples were observed for all cases and decrease in the ripple height did not occur at velocity up to $0.88 m/s$, indicating that the critical velocity for bed forms to be washed out into upper-regime plane beds [90] was larger than $U = 0.88 m/s$. Previous studies [90, 78] suggested that the transition to upper-regime plane bed occurred when Froude number ($F = U/\sqrt{gh}$) reached 1 so that the transition velocity in this study should be around $1.2 m/s$, consistent with our estimate that the transition for bare bed channels occurred at a channel velocity above $0.88 m/s$. The model vegetation impacted ripple height. First, at $U \approx 0.4 m/s$, the case with vegetation ($\phi = 0.005$) had larger η_1 than the bare channel case, and at $U \approx 0.3 m/s$, the case with $\phi = 0.012$ had larger η_1 than the two cases with $\phi = 0.005$, indicating that at the same channel velocity the low density model vegetation increased ripple height. However, the ripple height was decreased for cases with the densest vegetation ($\phi = 0.025$), for which the ripple height was on average 2 mm, barely four times the grain size, indicating that for the highest stem density the ripples were washed out at $U \leq 0.2 m/s$, suggesting that dense vegetation reduced the critical velocity at which upper-regime plane bed was formed.

For bare channel cases with different U, the ripple wavelength agreed within uncertainty, $\lambda \approx 0.3 m$ (Figure 4-6(b)), consistent with previous studies which indicated that the equilibrium ripple wavelength is only a function of grain size [3]. Soulsby et al. [89] compiled measurements from three laboratory studies and proposed the following empirical relationship: $\lambda = d_s(500+1881 D_*^{-1.5})$ for $1.2 < D_* = [g(\rho_s/\rho - 1)/\nu^2]^{1/3} d_s < 16$. In this study, $D_* = 12.6$, and the predicted ripple wavelength was $\lambda = 0.27 m$, which was consistent with our bare channel measurements ($\lambda \approx 0.3 m$, Table 4.2). For cases with vegetation, λ decreased with increasing vegetation solid volume fraction. The data suggested that the ripple wavelength scaled with the mean distance between two neighboring dowels aligned in the streamwise direction. Specifically, for $\phi = 0.005$

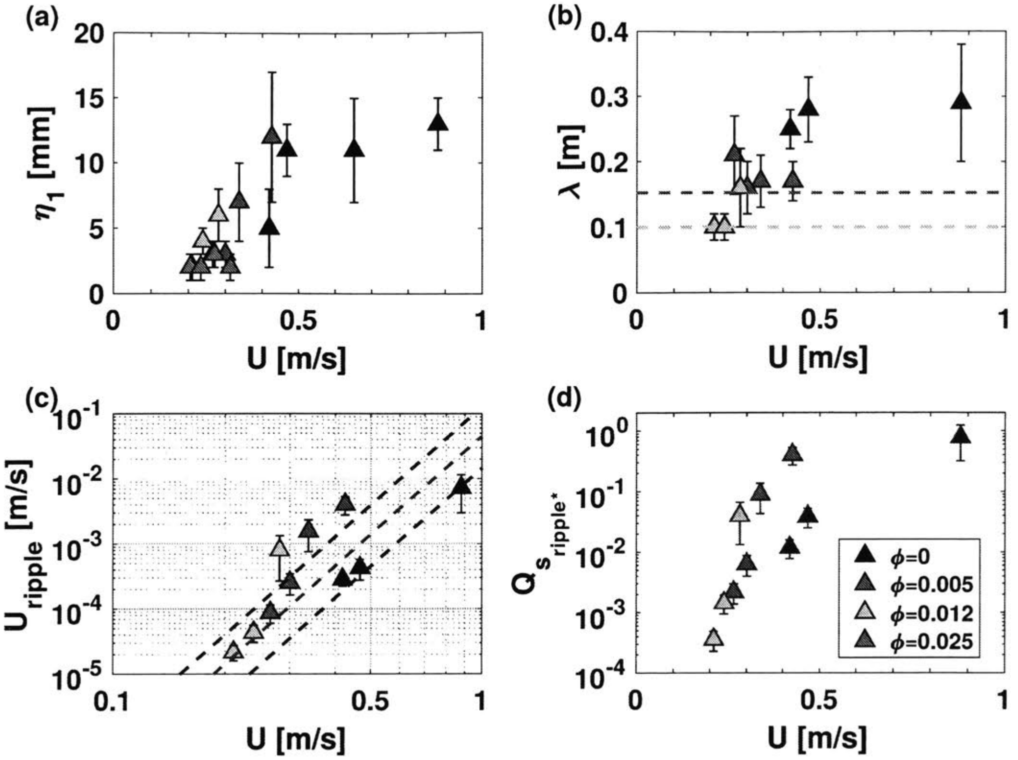

Figure 4-6: The ripple characteristics

(a) The ripple height (η_1) measured by the Vectrino and (b) the ripple wavelength (λ) measured by the laser sensor. For the cases with the densest vegetation ($\phi = 0.025$), the laser scanner wasn't reliable due to the interference from the closely-spaced dowels such that λ was not estimated. The dashed horizontal lines indicate the mean spacing between two neighboring dowels aligned in the streamwise direction. (c) The ripple migration speed $U_{ripple} = \lambda/T$ with the ripple migration period T measured by Vectrino profiler. The red and black dashed lines represent the empirical relationship proposed by Chang [12] for $d_s = 0.40mm$: $U_{ripple}/U^5 = (4.5 \pm 0.6) \times 10^2 (m/s)^{-4}$. Note that the x-axis was plotted in logarithmic scale to facilitate comparison of the present measurements with the [12] model. (d) The ripple migration rate estimated from equation 4.12 was normalized by the same quantity ($\rho_s\sqrt{(\rho_s/\rho - 1)gd_s^3}$) used to normalize Q_s (equation 4.6). The legend in Figure (d) applies to all figures.

and 0.012, the streamwise dowel spacing was $0.15m$ and $0.10m$, shown with blue and cyan dashed lines in Figure 4-6(b)). Except for two cases with large uncertainty (σ_λ), the ripple wave-length was equal to the streamwise stem spacing. Recall that the wavelength was not measurable for the highest volume fraction, for which the ripples were barely measurable.

The ripple migration speed, calculated as $U_{ripple} = \lambda/T$, varied by almost 3 orders of magnitude (Figure 4-6(c)). U_{ripple} increased with increasing U, similar to previous observations [12, 92]. For bare channel cases, the variation in U_{ripple} versus U agreed within uncertainty with the empirical relationship suggested by [12] for $d_s = 0.40mm$, $U_{ripple}/U^5 = (4.5\pm0.6)\times10^2(m/s)^{-4}$ (the dashed red lines and black lines in Figure 4-6(c)). Compared with bare channel cases, U_{ripple} increased with increasing vegetation solid volume fraction (Table 4.2). Specifically, at $U \approx 0.3m/s$, U_{ripple} increased when the solid volume fraction increased from $\phi = 0.005$ to 0.012, and at $U \approx 0.4m/s$, U_{ripple} increased from $\phi = 0$ to 0.005 (Figure 4-6(c)). The increase in ripple migration speed with increasing ϕ was consistent with the idea that the vegetation-generated turbulence increased bed load transport rate (Figure 4-5), causing the ripples to migrate faster.

In bare channels with ripples, before ripples started to be washed out and sheet flow started to form, the sediment transport associated with migrating ripples has been shown to approximate the total bed load transport [16, 18], i.e.,

$$Q_s = Q_{s_{ripple}} = \beta(\eta U_{ripple})C_0\rho_s. \tag{4.12}$$

Here $C_0 = 0.6$ is a porosity factor, and the coefficient β is the product of the ripple shape factor and the flow separation factor. The ripple shape factor is the fraction of a rectangular with width and height equal to the ripple wavelength and height, respectively, occupied by the ripple [51], and the flow separation factor accounts for the fact that many grains on the lee side of a ripple travel in the upstream direction due to flow separation and recirculation [18]. $\beta = 0.2$ to 0.8 was suggested in previous studies [51, 18]. For the bare channel measurements in this study, $\beta = 0.43$ provided the best agreement between measured bed load transport and equation 4.12. The dimensionless ripple migration rate, $Q_{s_{ripple}*}$, was plotted in Figure 4-6(d). $Q_{s_{ripple}*}$ varied by almost 3 orders of magnitude, predominantly due to changes in the magnitude of U_{ripple} (Table 4.2). Specifically, U_{ripple} increased with increasing ϕ, and this explains the increase in $Q_{s_{ripple}*}$ with increasing vegetation solid volume fraction. For example, at $U \approx 0.3m/s$ and $0.4m/s$, $Q_{s_{ripple}*}$ increased as vegetation volume fraction (ϕ) increased from 0.005 to 0.012 and from 0 (bare channel condition) to 0.005.

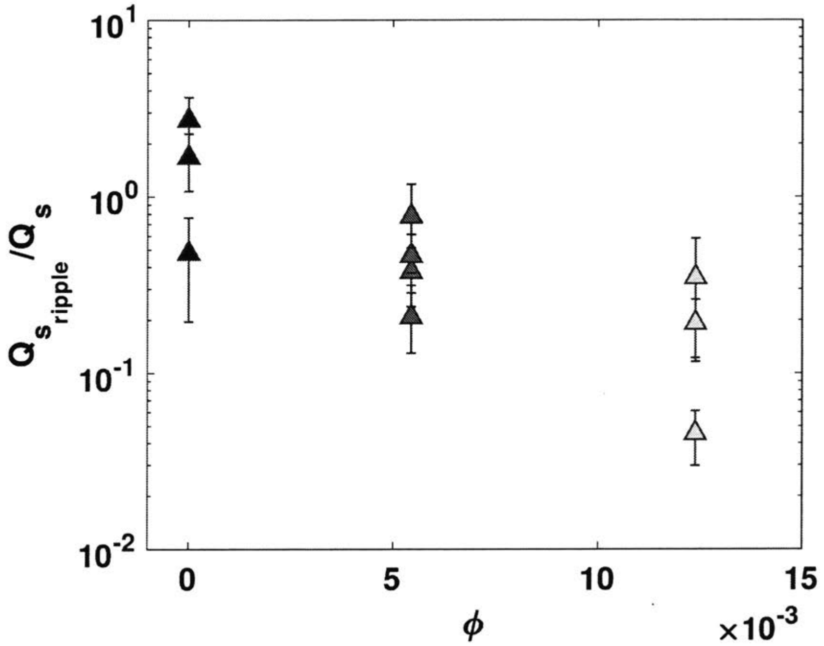

Figure 4-7: The ripple migration rate over bed load transport rate

The ripple migration rate $Q_{s_{ripple}}$ divided by the measured bed load transport rate Q_s as a function of vegetation solid volume fraction ϕ. The vertical error bars were contributed by the uncertainties in η_1, λ, and T (Table 4.2).

To test whether ripple migration represents the bulk of the bed load transport rate in vegetated channels, as it does in bare channels, the ripple migration rate ($Q_{s_{ripple}}$) divided by the measured bed load transport rate Q_s was plotted for both bare and vegetated channels in Figure 4-7. As expected for the fitted value of β, the average of $Q_{s_{ripple}}/Q_s$ for bare channels was one. However, as the vegetation solid volume fraction ϕ increased, $Q_{s_{ripple}}/Q_s$ decreased, indicating that as vegetation volume fraction increased, a increasing fraction of the bed load transport was not associated with ripple migration, which suggested a transition to sheet flow. This is supported by the fact that for cases with the densest vegetation ($\phi = 0.025$), the measured ripple height was significantly smaller than the other vegetated cases, and nearly comparable to the grain size, indicating that sheet flow occurred in the densest vegetated channel at a velocity much smaller than the critical velocity for transition to plane bed in bare channels ($U_{transit} > 0.88m/s$ as shown in Figure 4-6(a)). Furthermore, Nepf [71] and Rominger et al. [81] also report the elimination of migrating bedforms after vegetation was planted on a sand point bar, confirming that vegetation reduced the role of migrating bedforms in sediment transport, and facilitated the formation of sheet flow.

4.4 Discussion: the velocity and the number of moving grains

The measurements indicated a strong correlation between the bed load transport rate (Q_s) and the near-bed turbulent kinetic energy (k_t). However, intuitively, one expects that the channel velocity U should also affect Q_s, because the velocity of the individual grains in motion has been shown to increase with the channel velocity U [53, 82]. To understand the relative contributions of U and k_t to Q_s, the statistics of individual grains in motion provided in previous experiments using the same model vegetation were explored. In [119], mobile black sand grains were placed on top of a glued bed of brown sand grains, and the trajectories of the moving black grains were tracked using a digital camera. The streamwise velocity of individual grains was calculated from their trajectories with the average streamwise velocity of all the moving grains denoted as U_p. The volume of moving sediment per unit bed area, γ, was also calculated from the images. The bed load transport rate can then be estimated as $Q_s = U_p\gamma$ [117, 30].

For each ϕ, the average and the standard deviation of U_p/U at different channel velocity U are represented by black circles with vertical bars (Figure 4-8(a)). The mean U_p/U increased with increasing ϕ, and specifically the mean U_p/U increased by almost 50% as ϕ increased from 0 to 0.063, indicating that at the same U, the vegetation-generated turbulence increased U_p. The greater turbulence levels likely lifted individual particles farther from the bed, and, as noted in [75] particles lifted

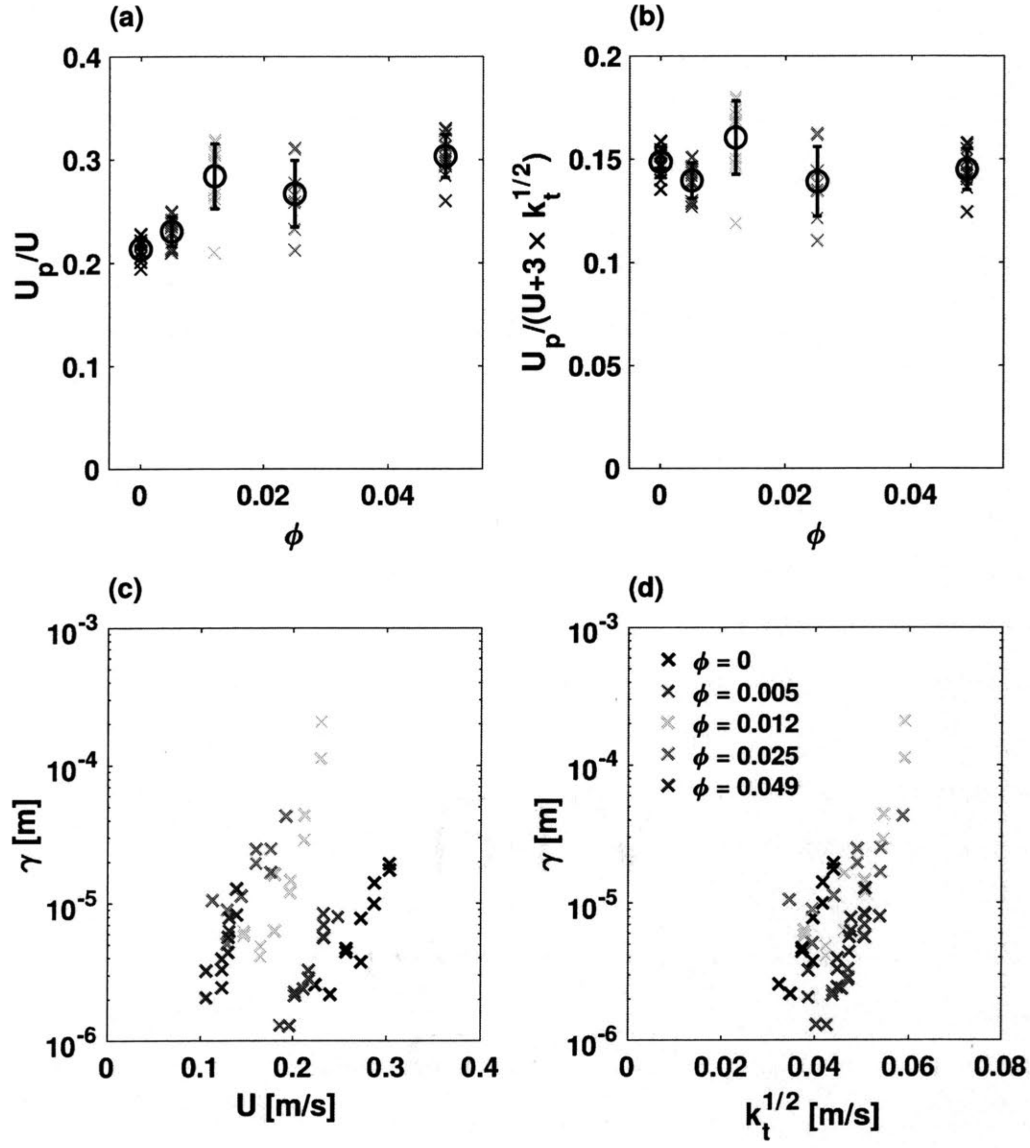

Figure 4-8: Statistics of moving sediment

The colored crosses indicate individual measurements of (a) the mean particle velocity normalized by channel velocity, U_p/U, and (b) U_p normalized by the linear combination of U and $\sqrt{k_t}$ measured at different channel velocities (U) for each vegetation solid volume fraction ϕ. The black circles with error bars in (a) and (b) represent the average and the standard deviation over all the cases with different U for each ϕ. (c)(d) The volume of particles in motion per bed area, γ, versus U and $\sqrt{k_t}$. The legend in Figure (d) applies to all figures.

higher above the bed achieve higher streamwise velocity. To take into account the impact of both U and k_t on U_p, we considered a linear combination, $U + \alpha\sqrt{k_t}$, to predict U_p. The value $\alpha = 3$ resulted in the smallest variation in $U_p/(U+\alpha\sqrt{k_t})$ across all ϕ, with the corresponding average and standard deviation of $U_p/(U + 3\sqrt{k_t}) = 0.15\pm0.01$, with no dependence of $U_p/(U+3k_t)$ on ϕ (Figure 4-8(b)), which suggested that the impact of volume fraction was captured by the magnitude of k_t.

While bedload transport ($Q_s = U_p\gamma$) increases with increasing particle velocity (U_p), which was increased by vegetation-generated turbulence (Figure 4-8(a)), Q_s is predominantly controlled by the number of particles put in motion, γ, which is also affected by the vegetation-generated turbulence. Specifically, Roseberry et al. [82] observed an over 2 orders of magnitude increase in γ with 40% increase in the near-bed velocity, in contrast to just a 60% increase in U_p, suggesting that the variation in Q_s is dominated by the variation in γ rather than U_p. Similarly, considering all the variations in U and ϕ across Yang et al. [119]'s data, the measured U_p varied by less than a factor of 3 (from 2.4 to $7.1cm/s$), but γ varied by two orders of magnitude, from $3.0 \times 10^{-8}m$ to $4.3 \times 10^{-6}m$ (Figure 4-8(c)), showing why that γ has stronger influence on Q_s than U_p. Further, at the same channel velocity U, γ increased significantly with increasing ϕ (Figure 4-8(c)), reflecting the influence of stem-generated turbulence. In particular, at $U = 0.22m/s$, γ increased by over 2 orders of magnitude as ϕ increased from 0 to 0.012, suggesting that the turbulence generated by the model vegetation significantly increased the number of sediment grains in motion. To further illustrate the impact of turbulence on γ, γ was plotted against $k_t^{1/2}$ $[m/s]$ in Figure 4-8(d). At the same $k_t^{1/2}$, γ for different ϕ collapsed to within less than one order of magnitude, and no dependence of γ on ϕ was observed, suggesting that γ or the number of particles in motion was mainly set by k_t rather than U. Finally, Roseberry et al. [82] also noted that γ fluctuates in space and time in response to the near-bed turbulent structures, supporting the hypothesis that the number of grains in motion is mainly set by k_t.

Because γ is mainly set by k_t, it is clear now why Q_s ($= U_p\gamma$) is also more closely correlated to k_t than U, as shown by the experimental results from the current study

(Figure 4-5). Although U could also influence Q_s because U_p scales with both U and k_t (Figure 4-8(b)), in our experiments, U varied by less than a factor of 3 ($U = 0.11$ to $0.30 m/s$), which was not enough range to reveal any dependence of Q_s on U. For the range of conditions considered, the k_t-based model provided a good prediction for Q_s and significantly improved prediction in regions with vegetation compared to the existing τ-based models.

4.5 Conclusions

Bed load transport rate, near-bed velocity, and ripple characteristics were measured in a sediment-recirculating flume with model vegetation. Velocity measurements from the present study validated a model for predicting turbulent kinetic energy (k_t) in vegetated channels with mobile beds. For the same time-mean bed shear stress (τ), both the measured near-bed turbulent kinetic energy (k_t) and the measured bed load transport rate (Q_s) increased with increasing vegetation solid volume fraction (ϕ), suggesting that the vegetation-generated turbulence enhanced bed load transport. Based on this, the turbulent kinetic energy (k_t) was hypothesized to be a better metric for predicting Q_s, because it takes into account the vegetation-generated turbulence. Indeed, the measured bed-load transport was shown to be more closely correlated with k_t than with τ, and further, a re-interpretation of the τ-based Einstein-Brown bed load transport model into a k_t-based model provided a significantly better prediction of measured bed-load transport in both bare channels and vegetated channels. The dependence of Q_s on k_t was explained using statistics of individual grain motion, which showed that Q_s is predominantly controlled by the number of grains in motion, which correlates with k_t. For the lower vegetation solid volume fractions ($\phi = 0.005, 0.012$), the ripple wavelength was constrained by stem spacing and the ripple height increased with increasing ϕ. However, at the highest vegetation solid volume fraction ($\phi = 0.025$), the ripple height was comparable to the grain size, indicating a transition to sheet flow at $U \leq 0.2 m/s$. Both the measured ripple migration speed and the bed load transport associated with ripple migration increased with increasing ϕ, suggesting that vegetation-generated turbulence accelerated bedform migration. However, the fraction of the total bed load transport carried by the migrating ripples decreased with increasing ϕ and in channels with the largest vegetation volume fraction ($\phi = 0.025$), the ripples were essentially eliminated, suggesting that vegetation facilitated the transition from bedforms to plane beds with sheet flow.

Chapter 5

Summary and future directions

5.1 Summary of my PhD work

Predicting bed load transport is important for anticipating detrimental erosion and restoring eroding habitats, yet the mechanisms of bed load transport are not fully understood. In addition to the conventionally-used bed shear stress (τ), turbulence has also been shown to affect bed load transport. For bare channels, i.e., channels without obstacles, the turbulent kinetic energy (k_t) and τ are linearly related, such that the role of turbulence is implicitly incorporated in these τ-based models and the τ-based models can be applied. However, in regions with vegetation, the τ-based bedload models have been shown to be inaccurate. My thesis research has shown that this is because vegetation generates turbulence that enhances bedload transport, and τ-based models do not account for this contribution.

In this thesis, the impact of the vegetation-generated turbulence on bed load transport was explored and quantitative models for predicting bedload transport in regions with vegetation were developed. Chapter 2 focused on the impact of vegetation-generated turbulence on the incipient condition of bedload transport. The trajectories of mobile black grains moving over a glued sand bed were tracked using a digital camera in a bare channel and in channels with emergent model vegetation of different volume fractions, ϕ. The critical velocity at which bed load transport started to occur, U_{crit}, was identified from these trajectories. U_{crit} decreased with increasing

ϕ, indicating that the vegetation-generated turbulence, which increased with increasing ϕ, facilitated the initiation of bedload transport. The critical near-bed turbulent kinetic energy (k_t) was shown to be a constant, suggesting that the k_t is a better predictor than τ of the incipient condition of bed load transport. A model based on a threshold value of k_t to predict U_{crit} in channels with vegetation was developed and validated by experimental data from the present experiments and previous flume experiments with both sand and mud.

Chapter 3 investigated the role of vegetation-generated turbulence on the bedload transport rate. Bedload transport rate Q_s and near-bed velocity were measured in a sediment-recirculate flume with both bare channels and channels with model vegetation simulated by aluminun cylinders. At the same τ, the measured Q_s increased with increasing vegetation solid volume fraction, ϕ, and this was attributed to the vegetation-generated turbulence, which also increased with increasing ϕ. In contrast, Q_s in both bare and vegetated channels collapsed when plotted against near-bed turbulent kinetic energy, k_t, suggesting that k_t plays a more important role in setting Q_s than τ. The dependence of Q_s on k_t was explained using statistics of individual grain motion (data from Chapter 2 experiments), which showed that Q_s was predominantly controlled by the number of grains in motion, which correlated with k_t. A reinterpretation of the τ-based Einstein-Brown equations as k_t-based equations was proposed, and the new k_t-based model predicted the Q_s measurements for both bare and vegetated channels. For an example salt marsh with a typical energy slope, e.g., surface slope due to tide, Q_s was estimated using both the τ-based Einstein-Brown model and the new k_t-based model. The τ-based model was shown to consistently underestimate Q_s by several orders of magnitude, illustrating that the vegetation-generated turbulence has a significant influence on Q_s in marshes.

Chapter 4 explored the impact of the vegetation-generated turbulence on bedform characteristics and the contribution of bedform migration to bedlaod transport. The variations of bed elevation in space and time were recorded by a laser topography scanner and an acoustic sensor, respectively, in both bare and vegetated channels with different vegetation volume fractions (ϕ). Ripples were observed, and the ripple height, wavelength, and period were identified from the laser sensor and acoustic sensor measurements. For the lower vegetation solid volume fractions ($\phi = 0.005, 0.012$), the ripple wavelength was constrained by stem spacing and the ripple height increased with increasing ϕ. However, at the highest vegetation solid volume fraction ($\phi = 0.025$), the ripple height was comparable to the grain size, indicating that dense vegetation facilitated a transition to sheet flow. Ripple migration speed and the bed load flux carried by migrating ripples were estimated from the measured ripple height, wavelength, and period. Both the measured ripple migration speed and the bed load transport associated with ripple migration increased with increasing ϕ, suggesting that vegetation-generated turbulence accelerated bedform migration. However, the fraction of the total bed load transport carried by the migrating ripples decreased with increasing ϕ, and the ripples were essentially eliminated in channels with the largest vegetation volume fraction ($\phi = 0.025$), suggesting that the model vegetation facilitated the transition from bedforms to plane beds with sheet flow.

5.2 Future research questions

5.2.1 Impact of vegetation spatial distribution on bed load transport

My bedload experiments used model vegetation uniformly distributed in a staggered pattern. The experiments showed that under the same time-mean bed shear stress, the turbulence, which represents the fluctuations around the time-mean value in the temporal domain, plays an important role in bed load transport. A natural extension would be to study how the spatial heterogeneity of vegetation, which affects the fluctuations of the turbulent kinetic energy around the spatial average, impact the total spatially-averaged bed load transport. For example, while keeping the mean vegetation volume fraction the same, if some parts of the vegetation get denser and other parts become sparser, the turbulent kinetic energy may be enhanced in regions with higher vegetation volume fraction if we the water surface slope and bed slope is the same (section 3.4.2 and Figure 3-5), where significant erosion might occur [67, 47]. This local enhanced erosion due to the spatial heterogeneity of the vegetation density may affect the total bed load transport rate, because the sediment transport rate varies with vegetation volume fraction ϕ logarithmically instead of linearly (Figure 3-5). For example, if the volume fraction of half of the patch becomes 1.5ϕ and the other half becomes 0.5ϕ, the total patch-averaged volume fraction is still phi. However, since Q_s is not a linear function of ϕ, it is likely that the total transport rate $\frac{1}{2}(Q_s(1.5\phi) + Q_s(0.5\phi)) \neq Q_s(\phi)$. The impact of the spatial distribution of vegetation on bed load transport is an important question to study, because natural vegetation tends to colonize into patches instead of being uniformly-distributed [67, 101, 62].

5.2.2 Impact of eddy duration on bed load transport

Recent studies have suggested that in addition to the magnitude of the instantaneous hydrodynamic forces, the duration of the forces also plays a role in bed load transport [21, 11]. Specifically, Diplas et al. [21] have shown that in order for a grain to move, not only does the magnitude of the peak force have to be above a critical value, but also the impulse, which is product of the magnitude and duration of the instantaneous force, has to be larger than a critical value, depending on the grain size [10, 11]. Because for the same peak force or turbulent kinetic energy, a larger impulse is more likely to initiate bed load transport [21, 10, 11], we hypothesize that for the same turbulent kinetic energy, increasing the duration of the lift force will lead to a decrease in the critical velocity to initiate sediment transport and an increase in the bed load transport rate.

In vegetated channels, the characteristic time scale of one eddy rotation is: $T_e = L_e/U$ [72], with the eddy characteristic length scale L_e equal to stem diameter d for sparse arrays [99] and U the channel velocity. As the characteristic duration of the pressure fluctuations above the sediment scales with the eddy duration [88], if T_e increases, the impulse will also increase, which we hypothesize will lead to an increase in the bed load transport rate.

For the bedload experiments considered here (Figure 4-5 in Chapter 4), the stem diameter ranged from 2mm to 13 mm. Figure 5-1 shows the ratio of the measured Q_s to the $Q_s(theory)$ predicted by by the k_t-based model (equation 4.11), plotted against the characteristic eddy duration $T_e = d/U$ [72, 99]. As T_e increased, $Q_s/Q_s(theory)$ also increased, suggesting that increasing the eddy duration may lead to an increase in Q_s, consistent with out hypothesis. However, because the uncertainty in the measured Q_s, due to variations in experimental set up, is around one order of magnitude (Figure 4-5 in Chapter 4), our experiments are not able to resolve and quantify the impact of eddy duration on bed load transport rate. Specifically, all the measured dimensionless bed load transport rate Q_{s*} agreed with the k_t-based model (equation 4.11) within uncertainty, and no clear dependence of Q_s on stem diameter d was observed (Figure 5-2), indicating that the range of d used here was not able to resolve the dependence of Q_s on d and thus T_e. More experiments with a larger range of vegetation stem diameter and velocity are needed to quantify the impact of eddy duration on Q_s.

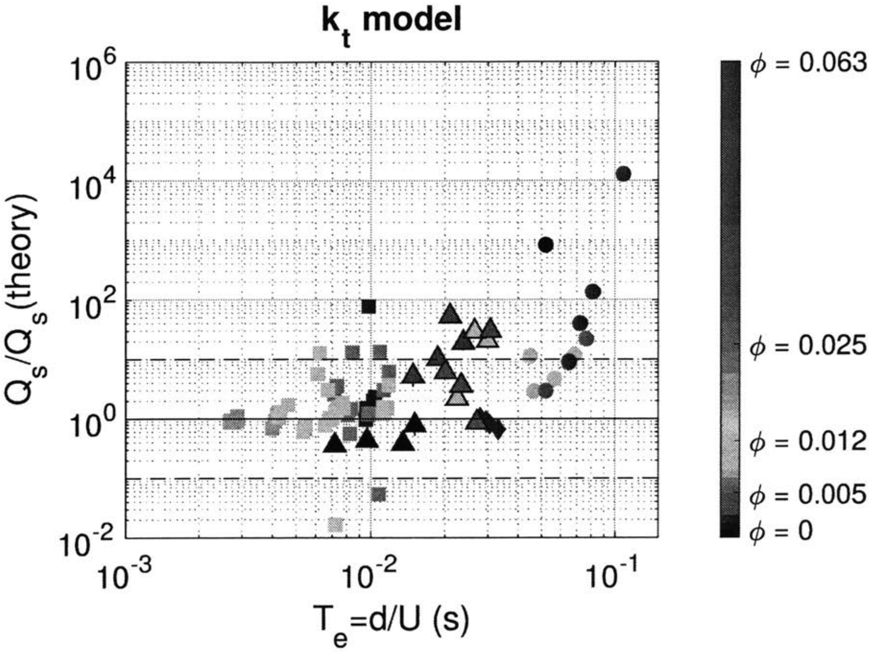

Figure 5-1: Impact of eddy duration of bed load transport rate

The ratio of measured Q_s to the bed load transport rate predicted by the k_t-based model (equation 4.11), $Q_s(theory)$, versus the eddy time-scale T_e [72, 99]. The dashed horizontal lines represent the experimental uncertainty of Q_s, which is one order of magnitude.

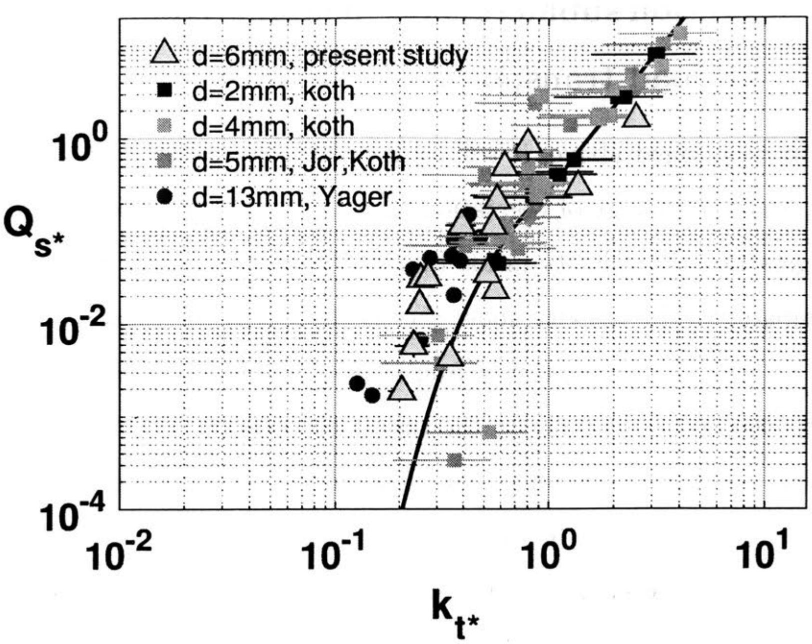

Figure 5-2: Impact of vegetation diameter on bed load transport rate

The measured Q_{s*} versus the dimensionless turbulent kinetic energy, k_{t*}, for different vegetation solid volume fractions (ϕ). The black curves represent the k_t-based model given in equation 4.11. The data sets used here are the same as in Figure 4-5 in Chapter 4, but labelled differently.

In addition, in Section 4.3.2, we argued that the k_t-based model (equation 4.11) may not apply for channels with sediment diameter d_s several times larger than vegetation diameter d, because for large d_s, only a small portion of the grain will be exposed to the lifting pressure, the spatial extent of which is the same order of magnitude as d. Therefore as d_s/d increases to much larger than 1, the k_t model may over-predict Q_s. For the cases presented in this thesis, d_s/d was always smaller or comparable to 1 so that the impact of d_s on Q_s can not be resolved. Further experiments with larger d_s/d is needed to test this hypothesis.

5.2.3 Impact of vegetation submergence, flexibility, and morphology on bed load transport

In addition to the factors mentioned above, it will be interesting to study how the submergence, flexibility, and morphology of vegetation affect bed load transport rate. For submerged rigid vegetation, the velocity inside the vegetation is reduced due to the vegetation drag, compared to the velocity above the vegetation. If the vegetation density is large ($ab \geq 0.1$ with a the vegetation frontal area per unit volume and b the vegetation height), the velocity profile at the top of the canopy will contain an inflection point, which will trigger the formation of a canopy-scale vortices [70]. The canopy-scale vortices may penetrate to the bed, for example at $ab = 0.1$ [57], affecting the total turbulent kinetic energy at the bed and the characteristic time scale of the eddies at the bed, affecting the sediment transport. Considering that submerged vegetation, such as seagrass, is ubiquitous in nature, it is important to study how vegetation submergence affects sediment transport. For submerged and flexible vegetation, such as seagrass, the drag induced by the canopy-scale vortices may cause the vegetation to deform or bend, and as a result the vegetation may wave periodically following the passage of the vortices, which is called monami [2, 35, 70]. The monami motion of vegetation can cause the canopy-scale turbulence to penetrate closer to the bed [31, 70], which may affect the near-bed turbulent kinetic energy and thus bed load transport. Moreover, the morphology of the vegetation may also affect bed load transport. For example, for non-cylindrical vegetation, the frontal area of the vegetation per unit volume (a) varies vertically [70]. A larger a means more energy get extracted by the vegetation, thus the velocity U decreases with increasing a [99, 70]. As the turbulent kinetic energy (k_t) is both a function of U and a, k_t may or may not varies vertically with a varing vertically[99], and as the bed load transport rate (Q_s) if a function of k_t, Q_s also may or may not change with vertical variation of a. The relevant questions are whether the k_t-based model (equation 4.11) apply to cases with non-cylindrical vegetation and how to define the near-bed turbulent kinetic energy.

Appendix A

The sediment-recirculating flume

Figure A-1 shows a flume that recirculates water and sediments separately. The pipeline and structures that returns, distributes, and bypasses sediment as well as related measuring instruments and techniques, such as a sediment imaging system and a laser bed topography system, were designed as part of the work of this thesis.

Figure A-1: Image of the sediment-recirculating flume.

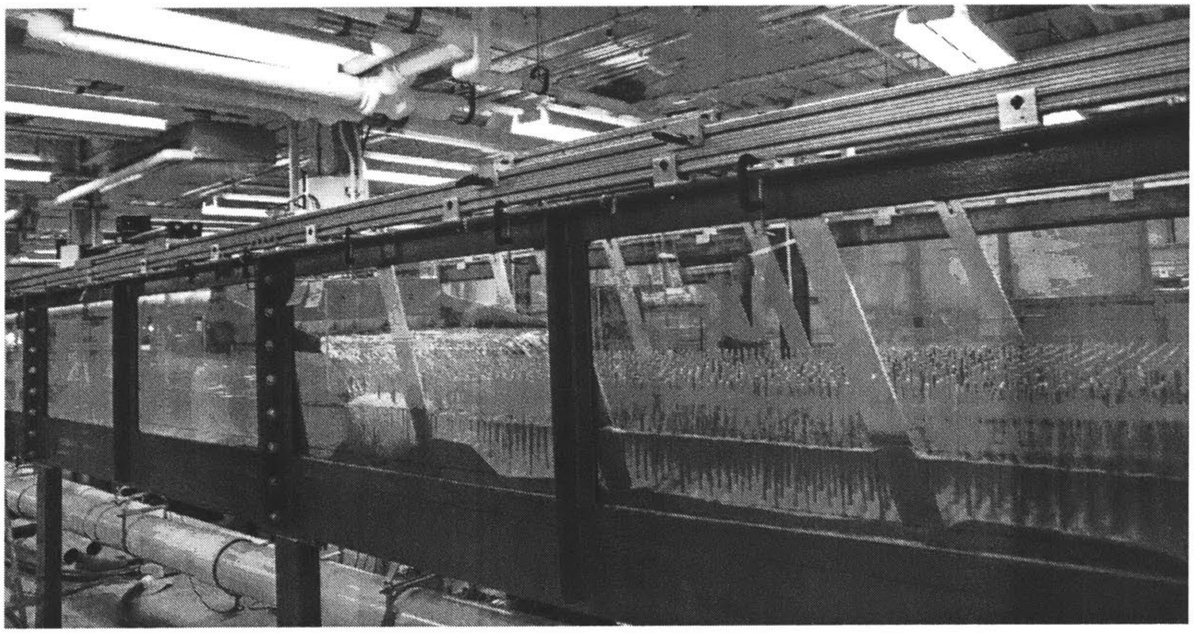

A.1 The Flume

Figure A-2 shows the flume that recirculates water and sand separately. The flume has a 1m wide and 10m long test section. The bed of the flume is horizontal. The water depth can go up to around 0.7m. There are two pumps in the flume system, one to recirculate water, and another one to recirculate sand. The pipe line used to recirculate sand is shown in Figure A-2.

The pump used to recirculate water is controlled by an electrical controller, and the flow rate can be set at the white control panel shown in the left bottom of Figure A-3. A flow meter was installed on the pipe line that recirculates the water to measure flow rate. The maximum flow velocity used in this study was around $1m/s$ and the maximum flow rate used was $380m^3/hour$, while the pump has the power to reach much higher flow rate (up to $1000m^3/hour$). The instruction for how to operate the flume is shown in Figure A-3.

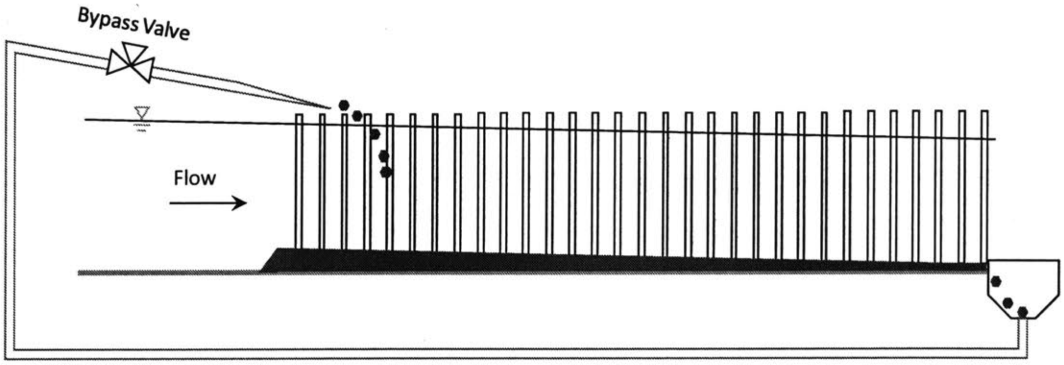

Figure A-2: A schemetic view of the flume.

Figure A-3: Instruction for the operation of the flume.

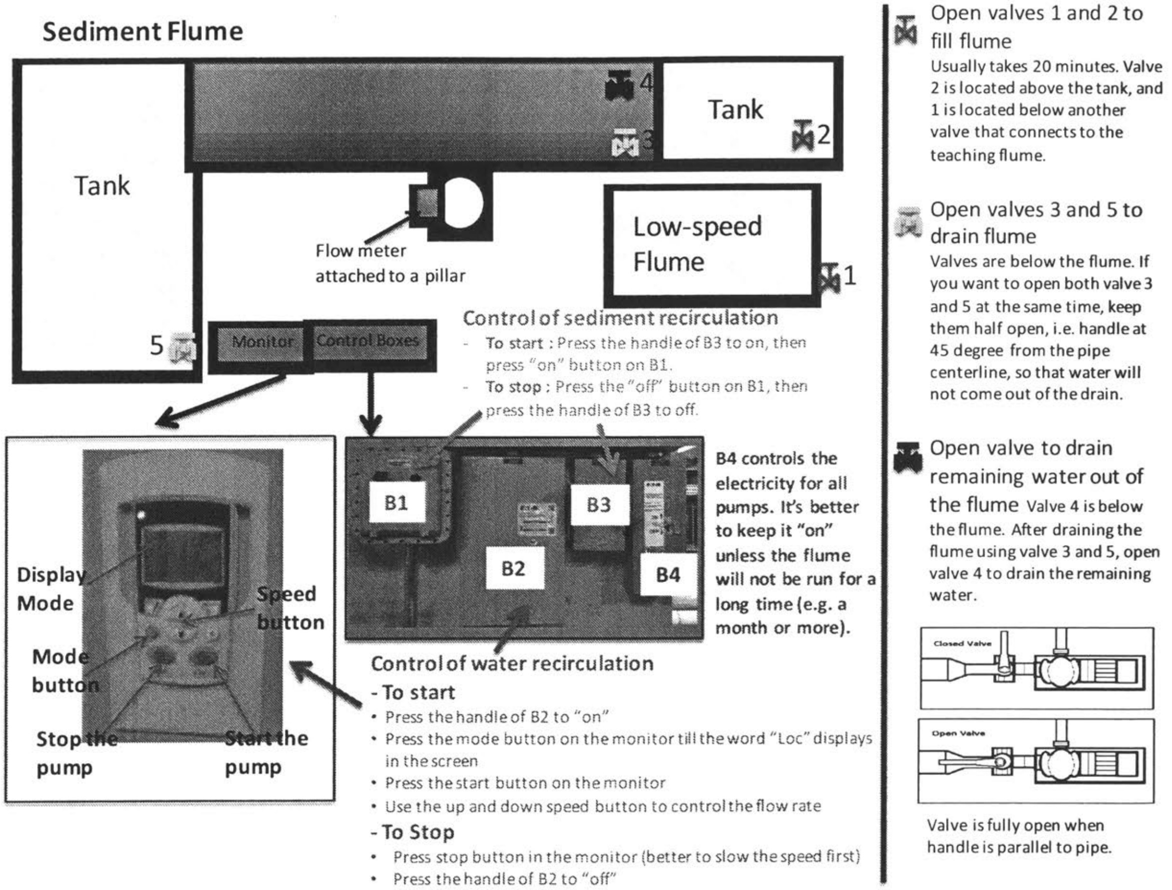

Control of sediment recirculation

- **To start :** Press the handle of B3 to on, then press "on" button on B1.
- **To stop :** Press the "off" button on B1, then press the handle of B3 to off.

B4 controls the electricity for all pumps. It's better to keep it "on" unless the flume will not be run for a long time (e.g. a month or more).

Control of water recirculation

- To start

- Press the handle of B2 to "on"
- Press the mode button on the monitor till the word "Loc" displays in the screen
- Press the start button on the monitor
- Use the up and down speed button to control the flow rate

- To Stop

- Press stop button in the monitor (better to slow the speed first)
- Press the handle of B2 to "off"

Open valves 1 and 2 to fill flume

Usually takes 20 minutes. Valve 2 is located above the tank, and 1 is located below another valve that connects to the teaching flume.

Open valves 3 and 5 to drain flume

Valves are below the flume. If you want to open both valve 3 and 5 at the same time, keep them half open, i.e. handle at 45 degree from the pipe centerline, so that water will not come out of the drain.

Open valve to drain remaining water out of the flume Valve 4 is below the flume. After draining the flume using valve 3 and 5, open valve 4 to drain the remaining water.

Valve is fully open when handle is parallel to pipe.

Figure A-4: The sediment cart that distributes sand uniformly across the flume width.

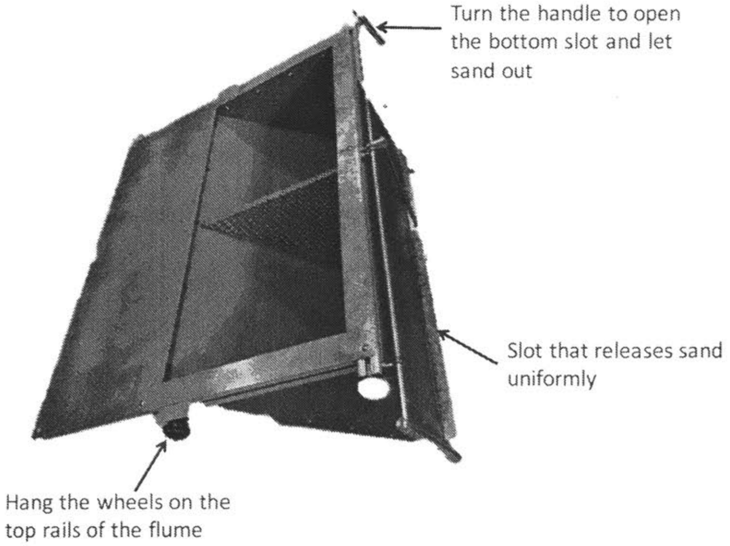

A cart that distributes sand uniformly across the width of the flume can be placed on top the flume rails to distribute sand. The operation of the cart is shown in Figure A-4. After the experiments, the sand needs to be cleaned out the flume manually using buckets or other tools.

During the experiments, a three-way butterfly value installed in the sediment recirculating pipeline can be used to bypass and collect sediments (Figure A-5). The mesh bag was sewn from 60 mesh silk screen fabric with hole size $250 \mu m$ to catch the sediments.

Figure A-5: The design of the sediment bypassing and collecting system.

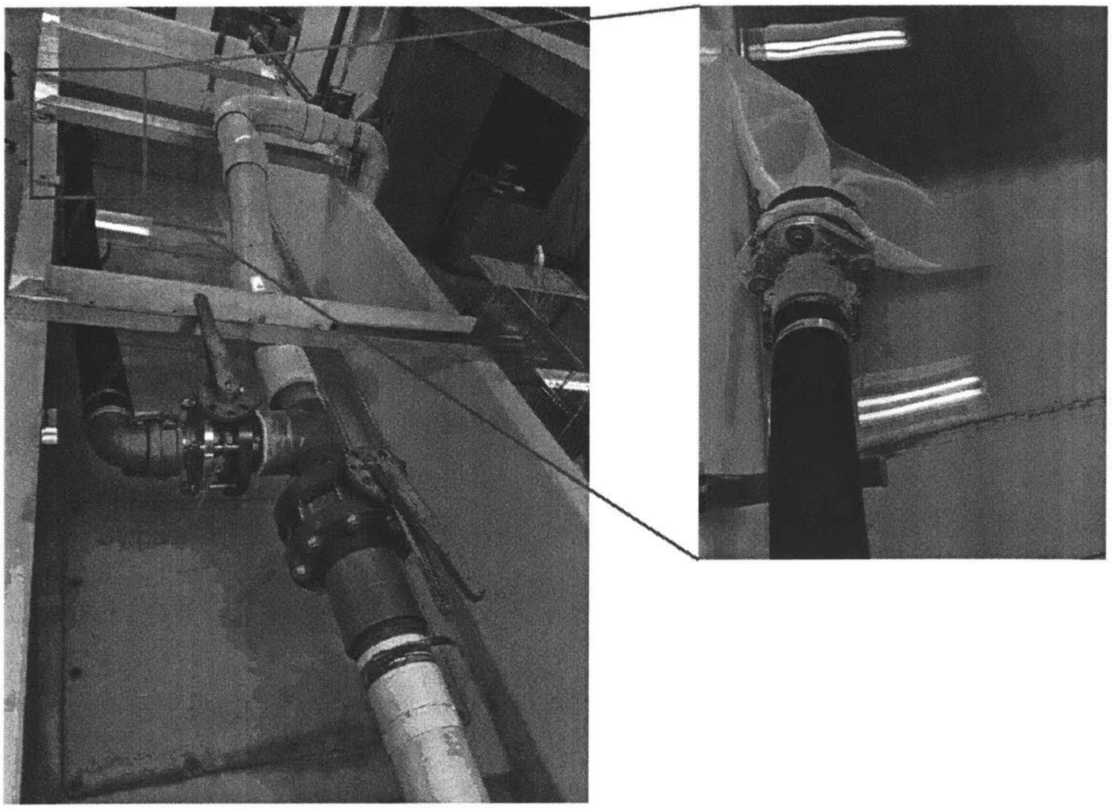

CAUTION: Please make sure at least one of the two valves shown in the figure is open. Otherwise high pressure will build up in the pipe, causing dangerous damage. Both valves can be open at the same time.

A.2 Methods to estimate the dry weight of sediments

The bed load transport rate is usually based on the dry weight of sediments passing a cross-section per unit channel width per time (e.g., [33]). In previous studies, the collected wet sediments were dried to measure their dry weight. In this study, a method to estimate the dry weight of the collected wet sand without drying the sand was developed. Specifically, the density difference between sand and water ($\rho_s - \rho$) was used to calculate the dry weight of the collected wet sediments. Consider a container with a certain volume of water (Figure A-6), if we put sediments into the container and pour water in until the water level reached a marked line so that the total volume is the same as the previous volume of water without sand, then the change in the mass of the container from initial mass without sand M_o to the final mass with sand M_f is due to the density difference between water and sand (ρ and ρ_s). The volume of the added sand is therefore $V_{sand} = (M_f - M_o)/(\rho_s - \rho)$. The dry mass of sand is therefore $M_s = (M_f - M_o)\rho_s/(\rho_s - \rho)$. As $\rho_s = 2.65g/cm^3$ and $\rho = 1.00g/cm^3$, the dry mass of the wet sediments is $M_s = 1.65(M_f - M_o)$. To test this method, dry sediments were wetted and their dry mass was estimated using the above method. The measured mass of the dry sediments (M_s) was plotted against ($M_f - M_o$) in Figure A-7. The measurements collapsed with the prediction ($y = 1.65x$).

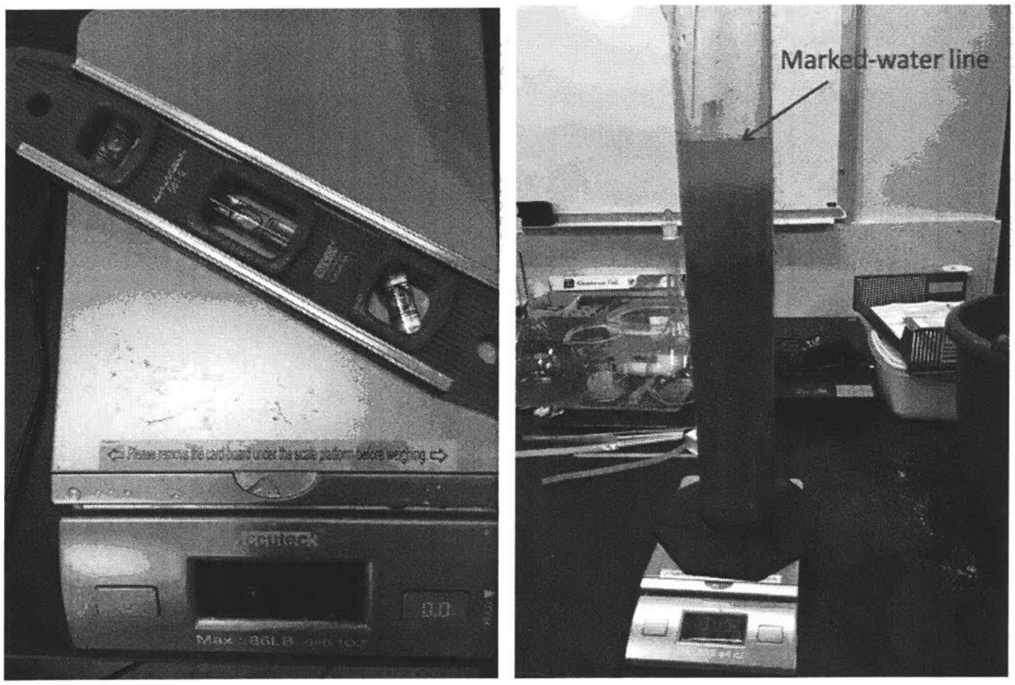

Figure A-6: Method for estimating sediment dry weight

Estimating the dry weight of the wet sand based on the density difference between sand and water. A level indicator was used to align the water surface to the marked water line to keep the total volume of sand and water the same as without sand.

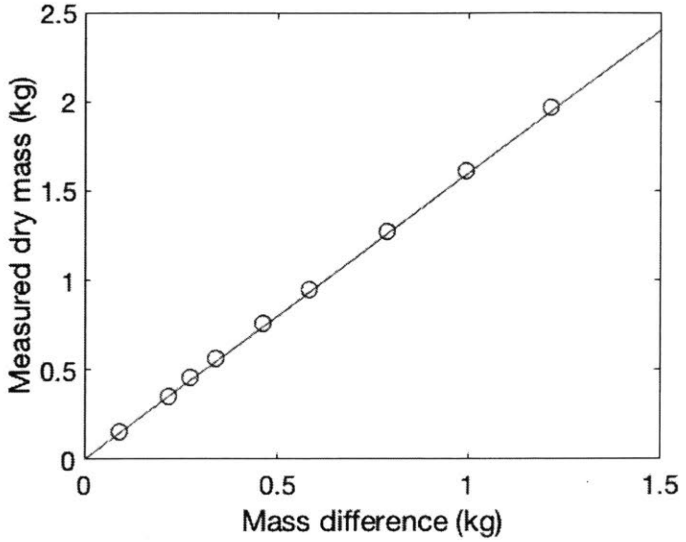

Figure A-7: Calibration of the sediment dry weight method

The measured dry mass of sediments versus the mass difference of the container after sediments were put in it. The redline represents the predicted dry mass $M_s = 1.65(M_f - M_o)$.

Appendix B

Instructions for particle-tracking

To track the trajectories of moving sediment grains, we designed the imaging system that records the sediment positions at up to 60 frames per second (Figure B-1). From the images recorded by the system, the sediment statistics can be calculated following the steps described below. The code to process the images are documented in section B.4.

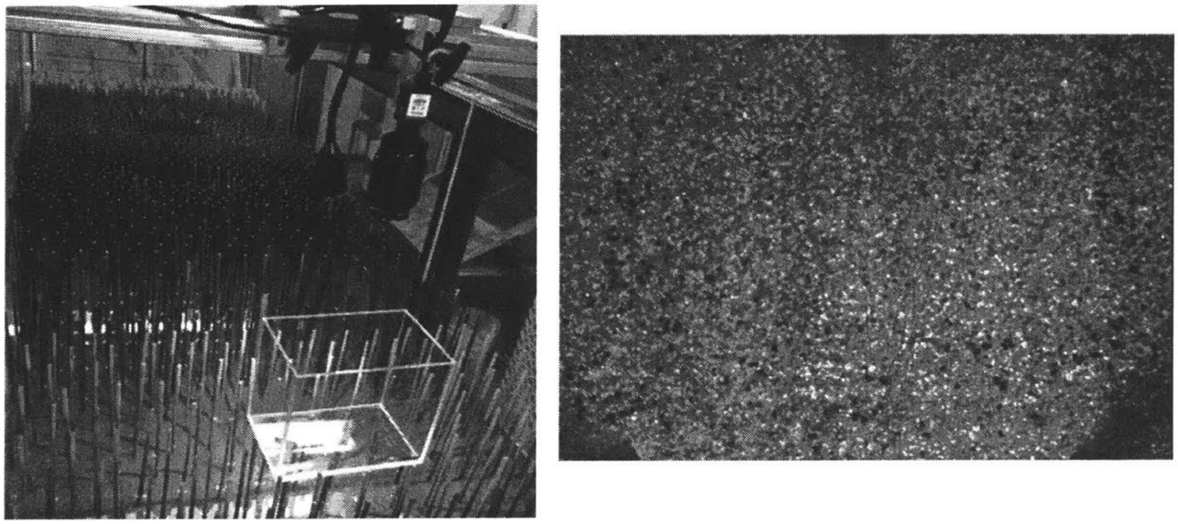

Figure B-1: Imaging system to track sediment trajectories

The imaging system designed to track the trajectories of moving sediment grains. The aquarium was used to reduce the distortion of the image due to surface waves.

B.1 Steps for running particle-tracking codes

STEP 1: read the .avi file and convert it to pictures. (This code converts the videos into pictures and create a folder for each video).

1. Open the MAIN_READ.m file in the subfolder, change Line 5 (the path of the folder to the path where you put all the videos). For example: path_tot = 'D:\Experiments\12_18_density2\';

2. If you want to crop images, you have to go to the Matlab file called: READ_AVI.m Here you have to uncomment line16, and change the crop size.

videoFrame = imcrop(videoFrame,[350, 220, 650, 650]); % [xstart, y_start, x_length, ylength]

Here the ,[350, 220, 650, 650]); % [xstart, y_start, x_length, ylength]is the pixel number.

Always check line 16 in READ _ AVI.m to make sure you get the right images in the folder.

3. Wait, this reading process might take a while, if you want to check the result, you can go to the folders and see how many pictures the code is creating.

STEP 2: Determine the critical intensity for the black sand

1. Open the matlab file called Blk_RATIO.m

2. Choose one pictures from Step1, and change the path Line4 of the Blk_RATIO.m file to the path of the picture you choose.

3. Tune the critical intensity value: the level = in Line 35 of Blk_RATIO.m till the optimal percent of black sand are picked up by the code.

4. Write down the critical intensity value (level) you choose. This value will be used later.

5. Zoom in one of the figures (figure 3, for example), and find out the diameter (in pixels) of the black sand using the "Data Cursor" from the "Tools" in the menu bar. Also write down this value about the diameter.

STEP 3: Set parameters:

1. Open the file called SET_PARAMETERS.m

a. Change Line11 (diameter) to the value you found from the diameter (5 from STEP2). (you can tune this value a little bit to get good results).

b. Change Line 24 (the critical intensity) to the value of level you found from the value of level (4 from STEP2).

c. Change Line 6 to the Frame rate you use.

d. Change Line 13-15 based on the pixel size of images and the actual size you measured using a ruler.

e. Change Line 19 to the mean value of grain size (the upper and lower limit of the sieve size), the unit is mm.

STEP 4: Tune parameters:

1. Play around with the parameter in SET_PARAMETERS.m

a. Chose a value for Line 44 (cntrd_1), this value should be larger than diameter, you can choose it to be diameter+2 or a little bit larger.

b. Tune Line 30 (pkfnd_1), and then open the file SAND_TRACk, → uncomment Line 49-63 (Press Control + T), and then Pause the file at Line 66 (press the line on the left of line 66) → Run the file called MAIN_RUN.m (need to change the path_tot and video_names of MAIN_RUM before run). → check the image from running MAIN_RUN and check how well the red cross symbols matches the white patches.

i. Tune pkfnd till the image you got from step b has the best match.

ii. Remember to uncomment Line 49-63 (Press Control+R) after you tuned pkfnd_1.

c. Tune Line 61 (maxdisp), Line66-69 - - maxdisp and Track_para.mem are the most important parameters for tuning. Maxdisp is the max distance the sand moves during one step. Track_para.mem is the steps particles can be missing. Tune this and then run the file MAIN_RUN → Then go to the folder of the images, and find another folder, and find the image called "traj.jpeg". i. Eyebow the "traj.jpeg". and guess a good value range. ii. Put the "traj.jpeg" and the avi file together in Premier and find the parameters (maxdisp and Track_para.mem) that work best. (will show you how to use premier soon).

B.2 Overlay trajectories on top of videos in Adobe Premiere to test the parameters

This section describes the steps to overlay the tracked particle trajectories on top of the recorded videos in Adobe Premiere to visually confirm the validity of the tracked trajectories.

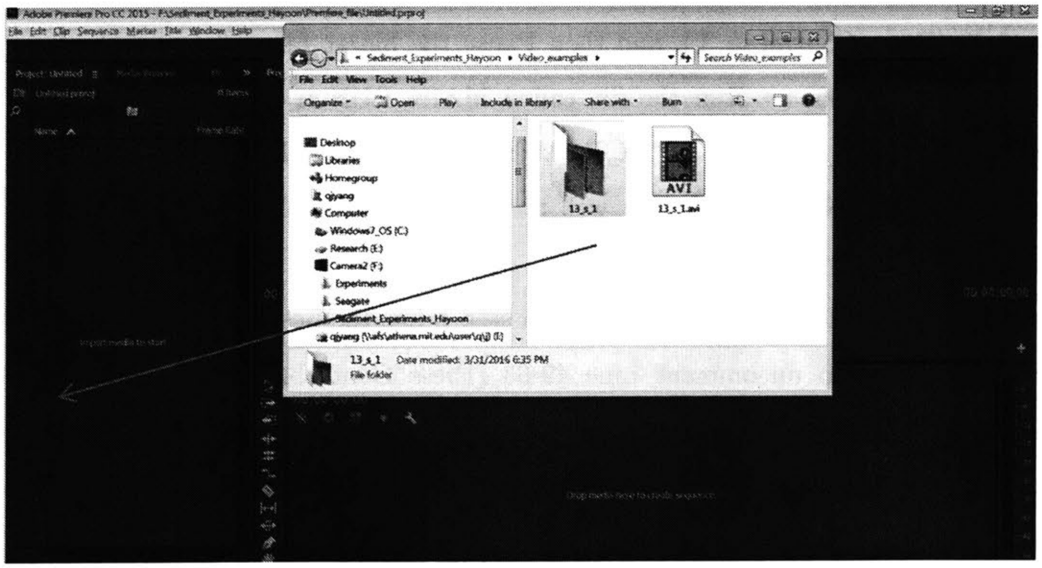

Figure B-2: Adobe Premiere Step 1

Open Adobe Premiere; Drag video and the trajectory image to the left

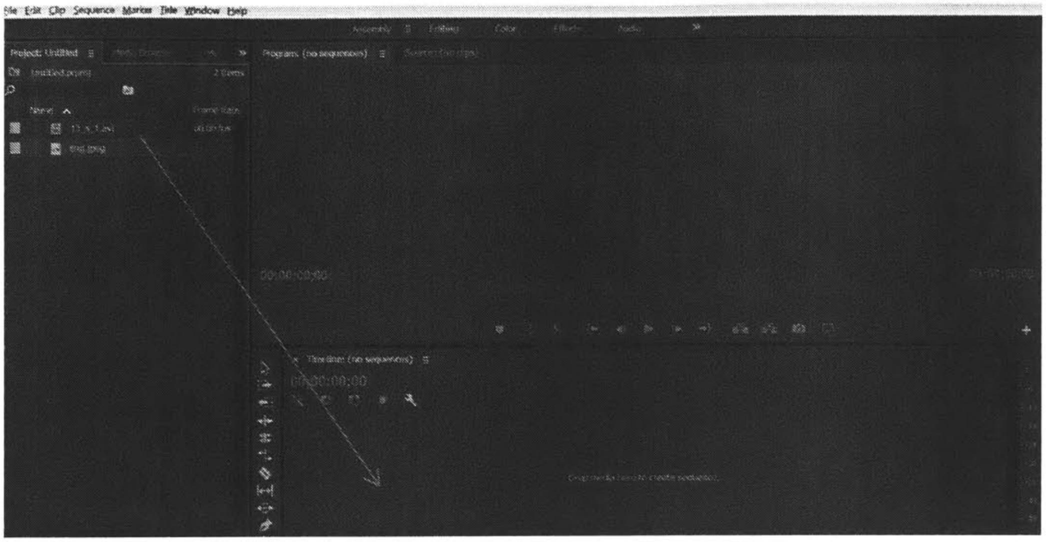

Figure B-3: Adobe Premiere Step 2

Drag the video and image from the left panel to the right panel

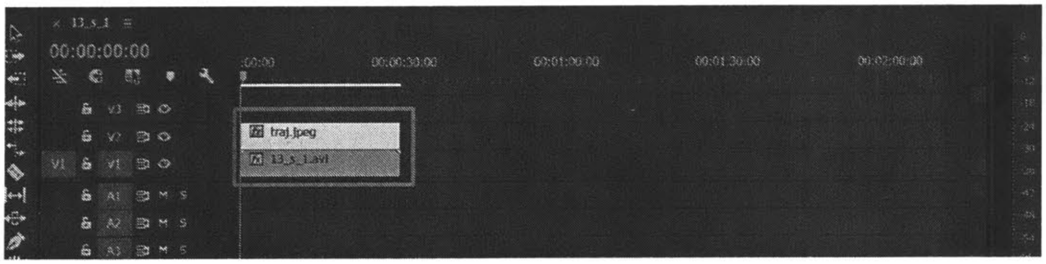

Figure B-4: Adobe Premiere Step 3

Make the two channels the same length

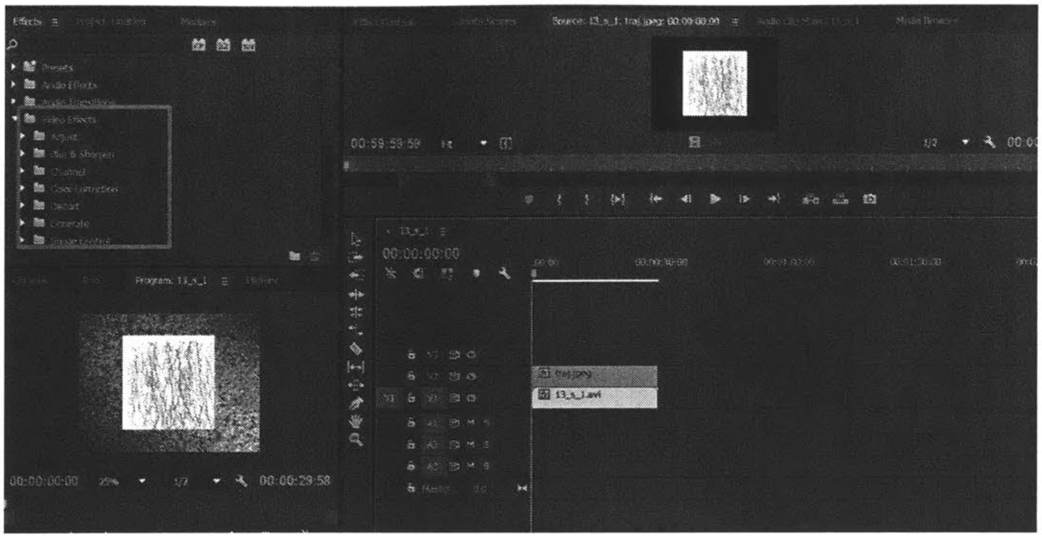

Figure B-5: Adobe Premiere Step 4

Chose the image(click on the image in the right panel) and then chose Video Effects in the left panel

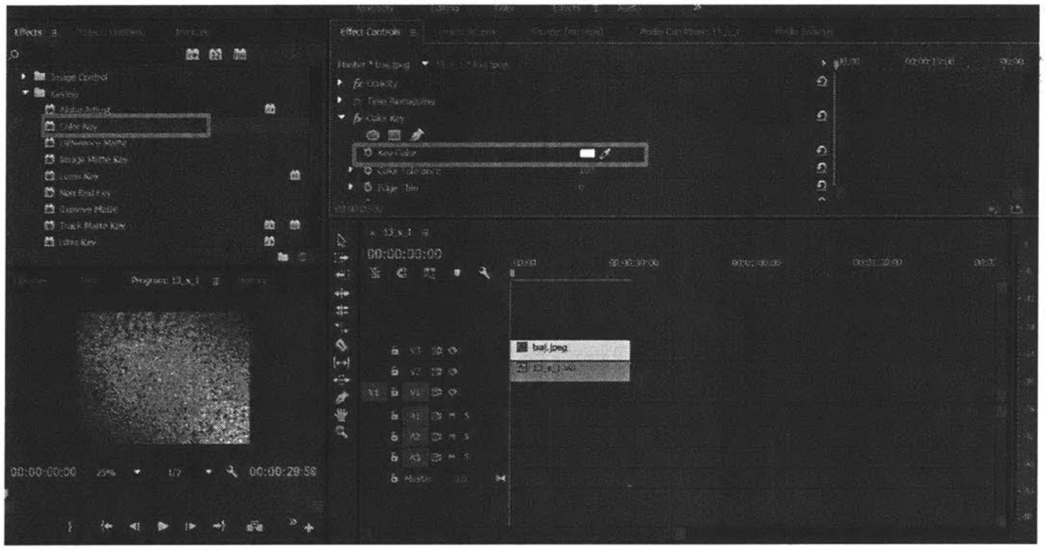

Figure B-6: Adobe Premiere Step 5

Choose video effects → Keying → color key; click on the pen symbol in the "effects control", and then click on the white space of the image, then change the color tolerance to value like 60 (tune it)

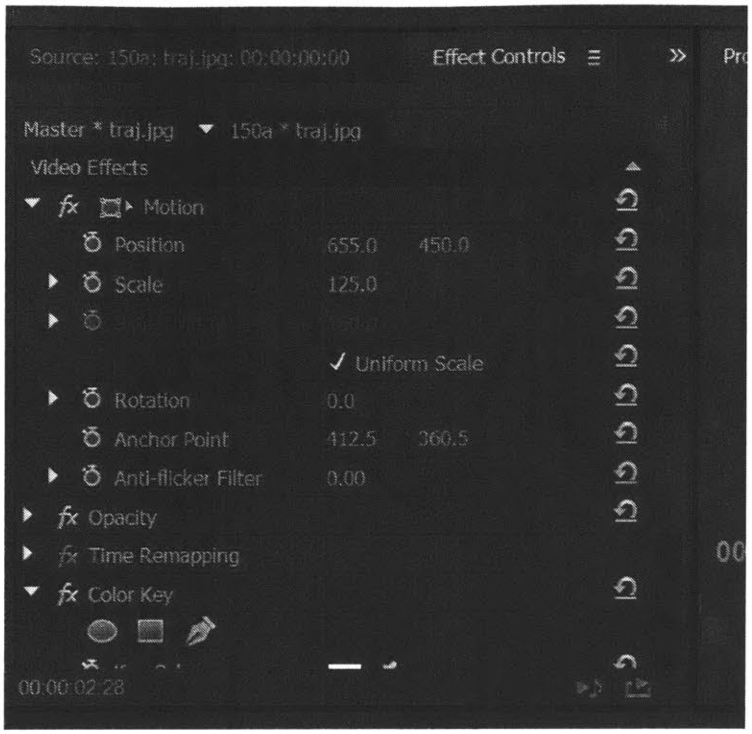

Source: 150a: traj.jpg: 00:00:00:00

Effect Controls

Master * traj.jpg ▼ 150a * traj.jpg

Video Effects

Motion

Position 655.0 450.0

Scale 125.0

✓ Uniform Scale

Rotation 0.0

Anchor Point 412.5 360.5

Anti-flicker Filter 0.00

Opacity

Time Remapping

Color Key

00:00:02:28

Figure B-7: Adobe Premiere Step 6

Adjust the position of the image (Effects control → motion → position)

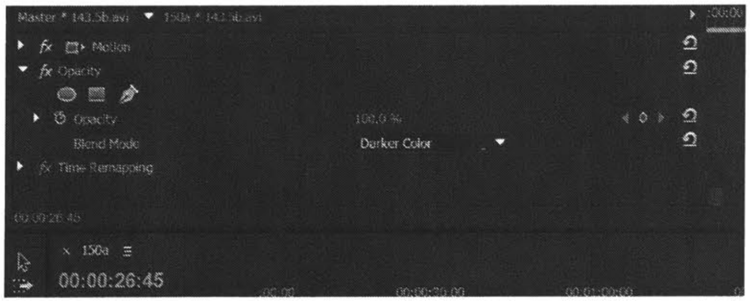

Master * 143.5b.avi ▼ 150a * 143.5b.avi

Motion

Opacity

Opacity 100.0 %

Blend Mode Darker Color

Time Remapping

00:00:26:45

150a

00:00:26:45

Figure B-8: Adobe Premiere Step 7

Export the video from the File in the menu bar

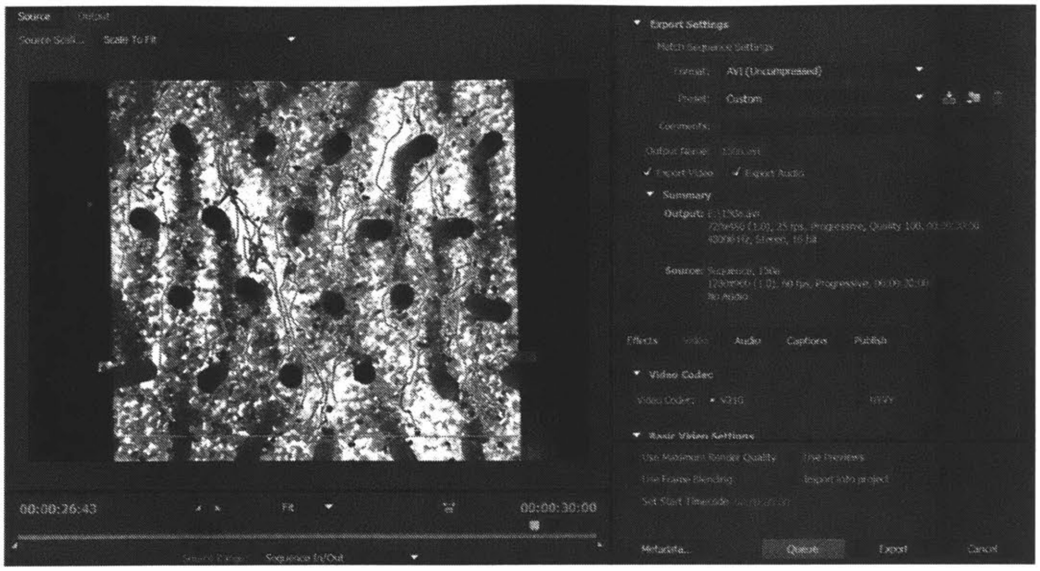

Format: AVI (Uncompressed)

Preset: Custom

Figure B-9: Adobe Premiere Step 8

Save to the hard disk in the computer

B.3 Estimate the sediment transport rate

STEP 1: Find Q_s for each video and put them in a excel file

1. Open the Matlab file called FINAL_QS_S_N.m

2. Change the excel_filename (Line 3) to the name of the excel file you are going to save. For the same vegetation density, this name should be the same, because all the data are going to be saved to the same excel file.

Change row number (line 18) incrementally, starting from 2 . This is the row number in excel that you are going to put the data. Remember to increase the number each time you run a new video.

It's good to start with lower velocity case (put them in beginning rows), and incrementally going to larger rows).

3. Change the path name (line 3, where you put the videos), and the video name (line 4), and the picture name (line 5). Note that the picture name is the name of the picture you took before you shoot each video to correct for the black sand that locked in the sand pockets.

If the picture is not 'jpg' format, change the format in Line 25.

velocity cases gradually.

4. SET_PARAMETERS.m should be set to the same value when you run the MAIN_RUN.m code to the trace the sand trajectory.

5. Change the image size (line 28), if you cropped the image then you have to set the crop size of the image, line 28. Remember to keep the size the same as you set in the file SET_PARAMETERS.

Congrats, you get all the Q_s for each flow velocity. You can use the some rows for the videos without sand, and choose the largest value of Q_s from the non-sand video as the error

STEP 2: Plot Q_s versus U relationship and find U_{crit}

1. Open the file "FINAL_UCRIT2.m".

2. Change the water depth (line 5) for each flow rate Q (line 14), better to let Q incrementally increasing. Change the depth of the aquarium (the distance from the bottom of the aquarium to the bed) in line 8. The width of the aquarium is in line 7.

3. Put the Q_s value for each Q in line 15.

4. Put the value of Q_s error in line 16 for each Q.

5. Change the vegetation density a (line 21). You can find this value from the sheet you use to configure vegetation. For bare bed a=0, then a=1.1, 2.5, 5.4, 9.8. a=9.8 is the densest vegetation.

6. Then Run the code.

B.4 Particle-tracking codes

1. MAIN_READ.m

```
close all; clear; clc;
%% This file automatically do everything
%% all video name
path_tot = ’D:\Density 1 experiments\’;
video_names = ’235.5a’,’235.5b’,’242.5a’,’242.5b’,’248a’;
%% creat folder for each video and process each videos
for ii = 1:numel(video_names)
clock1 = clock path_tot = ’D:\Density 1 experiments\’;
video_names = ’235.5a’,’235.5b’,’242.5a’,’242.5b’,’248a’;
vname = video_namesii;
%% Configure parameters for tracking sand;
READ_AVI; % Option 1: if the avi hasn’t been converted to images yet.
% SET_PARAMETERS %% Need to change parameters here % % clock2 = clock
% % PROCESS; % % save([analysis_path,’nbdelete_’,num2str(nb_delete,1),’.mat’]);
% % close all, clear; clc; end
```

2. READ_AVI.m

```
mkdir([path_tot, vname]) %% creat folders
path_folder = [path_tot, vname,’ \ ’];
mov=VideoReader([path_tot,vname,’.avi’]);
nFrames=mov.NumberOfFrames-1;
% clock1 = clock;
% for i= 1: nFrames
fname = [num2str(i,’%04d’)];
videoFrame=read(mov,i);
% h = imshow(videoFrame);
videoFrame = imcrop(videoFrame,[150, 60, 1050, 680]); % [ xstart, y_start, x_length,
```

```
ylength]
    imwrite(videoFrame,[path_folder, fname,’.png’])
    end
    % clock2 = clock
    % read_time = clock2-clock1
```

3. Blk_RATIO.m

```
    close all; clear;clc;
    %% Read image
    sand_img = imread(’D:\Small_grains\d90_.65_density_9.8\Run 1\94.5b\0001.png’);
    figure
    imshow(sand_img);
    dx = 101.6/1280; % the pixel length in mm;
    % Crop image
    figure;
    S_view = sand_img;
    % S_view = imcrop(sand_img, [290, 1, 990, 960]); % Crop the image ?
    imshow(S_view);
    % Convert to gray-scale
    New_Sview = rgb2gray(S_view);
    figure
    set(gca,’fontsize’,20);
    imshow(New_Sview);
    title(’Intensity’);
    %% Plot the histogram of the intensity
    gray_img = double(New_Sview);
    b = reshape(gray_img,1,[]);
    figure
    set(gca,’fontsize’,20);
```

```
h = hist(b,30);
h = h/sum(h);
bar(h, ’DisplayName’, ’Intensity’);
legend(’show’);
%% Set a threshold value
level = 0.25; % Level is the threshold intensity to identify the black sand ?
BW = im2bw(New_Sview, level);
imshow(BW)
Blk_p = length(find(BW==0))/numel(BW);
%%
figure
subplot(1,2,1)
set(gca,’fontsize’,20);
imshow(S_view);
subplot(1,2,2)
set(gca,’fontsize’,20);
imshow(BW);
title([’Ratio of black sand = ’,num2str(Blk_p,2)]);
```

4. SET_PARAMETERS.m

```
% % configure parameter
mov=VideoReader([path_tot,vname,’.avi’]);
nFrames=mov.NumberOfFrames-1;
Framerate = 60;
n = nFrames;
fname_list = [1:n];
t_list = 1/Framerate*[1:n];
diameter = 15; % The size of the sand in pixels ?
pixel_mm = 1280/101.6; % The number of pixels per mm, for different experiment set this is different?
height = 960;
```

length = 1280;

height_mm = (height)/pixel_mm ; % the length of of camera view, better keep consistent. % !! need to calibrate for each location !!!!!!

length_mm = (length)/pixel_mm ; % the unit is mm, the lateral direction.

dsand = (0.6+0.85)/2; % the unit is mm

Vol_sand = 4/3*pi*(dsand/2)^3; % the unit is mm^3;

nb_blk_sand = 0; % the number of sand pass through a line;

blk_level = 0.25; % The intensity of grayscale to distinguish black sand, depends on the lightening ; ?

method = 'sub';% ?

bpass_para = diameter;

% The number should be something like the diameter of the 'blob's you want to find in pixels. % %

pkfnd_1 = 0.2; % ?

pkfnd_2 = diameter;

% pk = pkfnd(b,pkfnd_1,11);

% pkfnd_1: default is 60; This should give you the location of all of the peaks that are above the given threshold value here given by 60.

% (NOTE: Make it big and the code runs faster

% but you might miss some particles. Make it small and you'll get

% everything and it'll be slow.)

% The brightest feature is max(max(b));

% pkfnd_2: The second parameter (set to 11) is roughly the diameter of the average feature to look for in pixels. This parameter is helpful for noisy data.

% if your data's noisy, (e.g. a single particle has multiple local

% maxima), then set this optional keyword to a value slightly larger than the diameter of your blob. if

% multiple peaks are found withing a radius of sz/2 then the code will keep

% only the brightest. Also gets rid of all peaks within sz of boundary

cntrd_1 = 17;

```
% diamter of the window over which to average to calculate the centroid.
% should be big enough
% to capture the whole particle but not so big that it captures others.
% if initial guess of center (from pkfnd) is far from the centroid, the
% window will need to be larger than the particle size. RECCOMMENDED
% size is the long lengthscale used in bpass plus 2.
% % Find the trajectories with average brightness bigger than critical value
b_crit = 0.03;
nb_delete = 0; % delete the trajctories with maximum distance travelled less than nb_delete*diameter.
U_delete = 1; % delete the sand trajectories with mean velocity > mean(U_traj) + U_delete*std(U_traj);
% % ? % % % % maxdisp = 40;
% an estimate of the maximum distance that a particle
% would move in a single time interval.(see Restrictions)
% If you could not find any trajectories, decrease maxdisp,
% if you find too many trajectories, increase maxdisp.
Track_para.mem = 10;
Track_para.good = 0;
Track_para.dim = 2;
Track_para.quiet = 0;
% OPTIONAL INPUT:
% param: a structure containing a few tracking parameters that are
% needed for many applications. If param is not included in the
% function call, then default values are used. If you set one value
% make sure you set them all:
% ; param.mem: this is the number of time steps that a particle can be
% ; 'lost' and then recovered again. If the particle reappears
% ; after this number of frames has elapsed, it will be
% ; tracked as a new particle. The default setting is zero.
```

```
% ; this is useful if particles occasionally 'drop out' of
% ; the data.
% ; param.dim: if the user would like to unscramble non-coordinate data
% ; for the particles (e.g. apparent radius of gyration for
% ; the particle images), then positionlist should
% ; contain the position data in positionlist(0 param.dim-1,*)
% ; and the extra data in positionlist(param.dim d-1,*). It is then
% ; necessary to set dim equal to the dimensionality of the
% ; coordinate data to so that the track knows to ignore the
% ; non-coordinate data in the construction of the
% ; trajectories. The default value is two.
% ; param.good: set this keyword to eliminate all trajectories with
% ; fewer than param.good valid positions. This is useful
% ; for eliminating very short, mostly 'lost' trajectories
% ; due to blinking 'noise' particles in the data stream.
% ; param.quiet: set this keyword to 1 if you don't want any text
% % Folder names
mkdir([path_tot, vname]) % % creat folders
path_folder = [path_tot, vname,'\'];
% creat folders
mkdir([path_tot, vname,'\','pk',num2str(pkfnd_1,2)]) % % creat folders
path_sub = [path_tot, vname,'\','pk',num2str(pkfnd_1,2),'\'];
% select trajectories with average brightness larger than b_crit
folder_analysis = ['Analysis_dmax_',num2str(maxdisp,2),'pk',num2str(pkfnd_1,2),method];
mkdir([path_sub, folder_analysis]) % % creat folders
analysis_path = [path_sub, folder_analysis,'\'];
% mkdir([ analysis_path,'\','trajectories']) % % creat folders
% traj_path = [ analysis_path,'\','trajectories','\'];
```

5. SAND_TRACK.m

```
% % This file use the subtract images to find sand motion.
% blk_sand: returnes the percentage of sand pixel in each image
% nb_blk_sand: returns the number of moving black sand in the view
% sand_rate: returns the number of moving sand per second per mm
% %
i = 1; fname = [num2str(fname_list(i),' %04d')];
pic0 = imread([path_folder,fname,'.png']);
pos_lst = [];
bsize_lst = [];
blk_sand = zeros(n,1);
for i = 2:n
%_______^^read original images in the folder one by one^^^^^^^^^^^^^^ %
fname = [num2str(fname^list(i),' %04d')];
pic = imread([path^folder,fname,'.png']);
%^^^^^^^^^^^^^^^^^^^^^^Subtract consequent images ^^^^^^^^^^^^^^^^^^^^ %
pic^diff = pic0 - pic;
% figure
% imshow(pic^diff);
aa = double(rgb2gray(pic^diff))/255;
% % figure
% mesh(aa)
% view(0,-90)
bb = bpass(aa,1,bpass^para); %
% figure
% mesh(bb)
% view(0,-90);
pic0 = pic;
%^^^^^^^^^^^^^^^find the center of the moving sand^^^^^^^^^^^^^^^^^^^^ %
pk = pkfnd(bb,pkfnd^1,pkfnd^2);
```

```
%This should give you the location of all of the peaks that are above the given threshold value here given by 60.
%The brightest feature is max(max(b)); The second parameter (set to 11) is roughly the diameter of the average feature to look for in pixels. This parameter is helpful for noisy data.
% % Plot the sand from find sand
% if numel(pk) =0
% fig = figure;
% imshow(aa)
% hold on;
% plot(pk(:,1),pk(:,2),'r+','MarkerSize',3); % %
% set(gca,'position',[0 0 1 1]) % set the drawable position of the image to the hole domain %
% set(gca,'XTick',[]) % Remove the ticks in the x axis!
% set(gca,'YTick',[]) % Remove the ticks in the y axis
% truesize
% % end
% the centroid of the peak
cnt = cntrd(bb,pk,cntrd^1); %out=cntrd(im,mx,sz,interactive); sz: diamter of the window over which to average to calculate the centroid.
% should be big enough
% to capture the whole particle but not so big that it captures others.
% out(:,1) is the x-coordinates
% out(:,2) is the y-coordinates
% out(:,3) is the brightnesses
% out(:,4) is the sqare of the radius of gyration
sand^size = size(cnt);
sand^nb = sand^size(1);
%^^^^^^^^^^^^Put the sand center and time information and the size and the brightness infomation together^^^^^^^ %
```

```
Pos = [];
bsize = [];
if isnan(cnt)==0
Pos = [ cnt(:,1), cnt(:,2), t^list(i)*ones(sand^nb,1) ];
bsize = [ cnt(:,3), cnt(:,4) ];
pos^lst = cat(1, pos^lst,Pos);
bsize^lst = cat(1, bsize^lst,bsize);
end
pic^double = double(rgb2gray(pic))/255;
blk^sand(i) = numel(find(pic^double ¡ blk^level))/numel(pic^double);
% % Plot the sand from find sand
% if numel(cnt) =0
% fig = figure;
% imshow(aa)
% hold on;
% plot(pk(:,1),pk(:,2),’r+’,’MarkerSize’,3); % %
% set(gca,’position’,[0 0 1 1]) % set the drawable position of the image to the hole
domain %
% set(gca,’XTick’,[]) % Remove the ticks in the x axis!
% set(gca,’YTick’,[]) % Remove the ticks in the y axis
% truesize
% % % % Plot the sand from find sand
% fig = figure;
% imagesc(pic)
% hold on;
% plot(cnt(:,1),cnt(:,2),’r+’,’MarkerSize’,3);
% % % set(gca,’position’,[0 0 1 1]) % set the drawable position of the image to
the hole domain
% % set(gca,’XTick’,[]) % Remove the ticks in the x axis!
% set(gca,’YTick’,[]) % Remove the ticks in the y axis
```

```
% truesize
% %
% % screen2jpeg([path^folder,’trajectory;fname,’.png’])
% end %
% %^^^^^^^^^^^^^^^calculate the ratio of black sand^^^^^^^^^^^^^^^^^^^ % %
% % % figure
% imshow(pic^double);
% title([’Black sand ratio = ’,num2str(blk^sand(i),2)]);
% % BW = im2bw(pic^double, blk^level);
% % figure; hold on;
% imshow(BW)
% title([’Black sand ratio = ’,num2str(blk^sand(i),2)]);
% close all
end
```

6. MAIN_RUN.m

```
close all; clear; clc;
% % This file automatically do everything
% % all video name
path_tot = ’D:\Small_grains\d90_.65_density_9.8\Run 1\’;
video_names = ’12.5’,’36’,’59a’,’59b’,’66a’,’66b’,’71’,
’77.5a’,’77.5b’,’83.5’,’89.5’,’94.5a’,’94.5b’,’101’,’112.5a’,’112.5b’,’124a’,’124b’;
% % creat folder for each video and process each videos
for ii = 1:numel(video_names)
clock1 = clock
path_tot = ’D:\Small_grains\d90_.65_density_9.8\Run 1\’;
video_names = ’36’,’59a’,’59b’,’66a’,’66b’,’71’,’77.5a’,’77.5b’,
’83.5’,’89.5’,’94.5a’,’94.5b’,’101’,’112.5a’,’112.5b’,’124a’,’124b’;
% ’12.5’,’36’,’59a’,’59b’,’66a’,’66b’,’71’,’77.5a’,’77.5b’,’83.5’,’89.5’,’94.5a’,’94.5b’,’101’,
% ’112.5a’,’112.5b’,
```

```
vname = video_namesii;
% vname = ’235.5a’;
SET_PARAMETERS % % Need to change parameters here
PROCESS;
save([analysis_path,’ALL.mat’]);
close all, clear; clc; end
```

7. tr_vel.m

```
function [Utot,pmov_nb,pmov_dt] = tr_vel_pvel_number(tr, pixel_mm,Framerate)
x = tr(:,1)/pixel_mm;
y = tr(:,2)/pixel_mm;
t = tr(:,3);
id = tr(:,4);
pmov_nb = numel(unique(id));
% %
% figure; hold on;
% set(gca,’FontSize’,20);
%
% color_jet = jet(10);
tn = []; % Find the position where U is negantive
Un = [];
index_negative = [];
nb_sum = 0;
Utot = [];
% % % delete the trajectories with motion less than nb_delte*diameter
% index_obv = [];
% % for j = 1: max(id)
% index = find(id == j);
% % if max(y(index)) - min(y(index)) ¿ nb_delete*diameter/pixel_mm %
% index_obv = cat(1, index_obv, index);
```

```
% end
% % end
% % tr = tr(index_obv,:);
% bsize_lst = bsize_lst(index_obv,:);
% %
traj_index2 = 0;
ID_traj = [];
T_tot = [];
Utot = [];
U_traj = [];
for j = 1: max(id)
index = find(id == j);
pmov_dt(j) =0;
if numel(index)¿1
x_p = x(index);
y_p = y(index);
t_p = t(index);
traj_index2 = traj_index2 + 1;
Utot( nb_sum+1 : nb_sum +numel(index)-1 ) = (y_p(2: numel(index)) - y_p(1: numel(index)-1 ))./(t_p(2: numel(index)) - t_p(1: numel(index)-1 ));
T_tot( nb_sum+1 : nb_sum +numel(index)-1 ) = t_p(1:numel(index)-1);
ID_tot( nb_sum+1 : nb_sum +numel(index)-1 ) = j;
ID_traj(traj_index2) = j;
U_traj(traj_index2) = mean(Utot( nb_sum+1 : nb_sum +numel(index)-1 ));
% % % % Record the index and value of the negative % % % % velocities.
% % Find the index of negative U
% index_id_n = find(Utraj¡0)
% if numel(index_id_n¿0)
% Un = cat(2, Un, Utraj(index_id_n));
% tn = cat(1, tn, t_p(index_id_n));
```

```
% index_negative = cat(1, index_negative , index(index_id_n));
% end
%
% plot(t_p(1:numel(index)-1 ) , Utot( nb_sum +1 : nb_sum + numel(index)-1
),'o', 'color', color_jet(rem(j,10)+1,:));
% plot the all the velocities at different times,
% different colors indicate different particles.
nb_sum = nb_sum + numel(index) - 1;
pmov_dt(j)=max(t_p)-min(t_p);
clear x_p;
clear y_p;
clear t_p;
clear index;
end
index_U_pixel = find(Utot¿1/pixel_mm*Framerate);
Utot = Utot(index_U_pixel);
T_tot = T_tot(index_U_pixel);
end
```

8. track.m

The original code was written by Crocker and Grier [1996],

can be found in the following link:

http:\\www.physics.emory.edu\faculty\weeks\\idl\

```
%; Judy added some code to track the intensity and size of particles at
% around line 1077
%
% ; see http:\\glinda.lrsm.upenn.edu\ weeks\idl
% ; for more information
olist = olist(2:end,:);
%bigresx = 0;
```

```
%resx = 0;
nolist = length(olist(:,1));
res = zeros(nolist,dd+1);
for j=1:dd
res(:,j) = xyzs(olist(:,1),j);
end
res(:,dd+1) = olist(:,2);
for j = 1:2
bright_Usize(:, j) = bsize_Ulst(olist(:,1),j); %%
end
```

Appendix C

Guideline for measuring bed topography and surface slope

C.1 Design of the topography and water-surface system

This section describes the topography system that maps the 3D bed topography (Figure C-1). A Keyence laser sensor to measure bed elevation and an Omega acoustic sensor that measures the distance from the sensor to the water surface, are mounted on a 2-D moving system. Previous studies such as [29] require the flume to be drained to measure the bed topography. In this study, I developed a method to directly measure bed topography without draining the flume by correcting for the difference in the speed of light in air and in water. In the situation with no water layer, if the bed elevation changes by Δh, the sensor would record a change in the travel time of the light dt, and calculate the distance change as $\Delta h_{sensor} = C_{angle} \times dt \times c_{air}$. The coefficient $C_{angle} \approx 2$ varies with the distance from the sensor head to the bed. With a water layer present (Figure C-3), the change in the time due to bed elevation change is $dt = \Delta h / C_{angle} / c_{water}$, therefore the relationship between the change in the sensor reading and the bed elevation change is $\Delta h_{sensor} = \Delta h \times c_{air} / c_{water} = 1.33 \Delta h$. To test if this hypothesis is true, sand layers with different Δh were put in the flume, and were measured using a ruler. The laser sensor reading Δh_{sensor} was also recorded for different measured Δh. The experimental results show that $\Delta h_{sensor} = (1.4 \pm 0.1)\Delta h$, in good agreement with the prediction. Because the bed elevation before and after bed form migration were measured and subtracted, the absolute value of the water depth does not come into the equation in measuring bed elevation change.

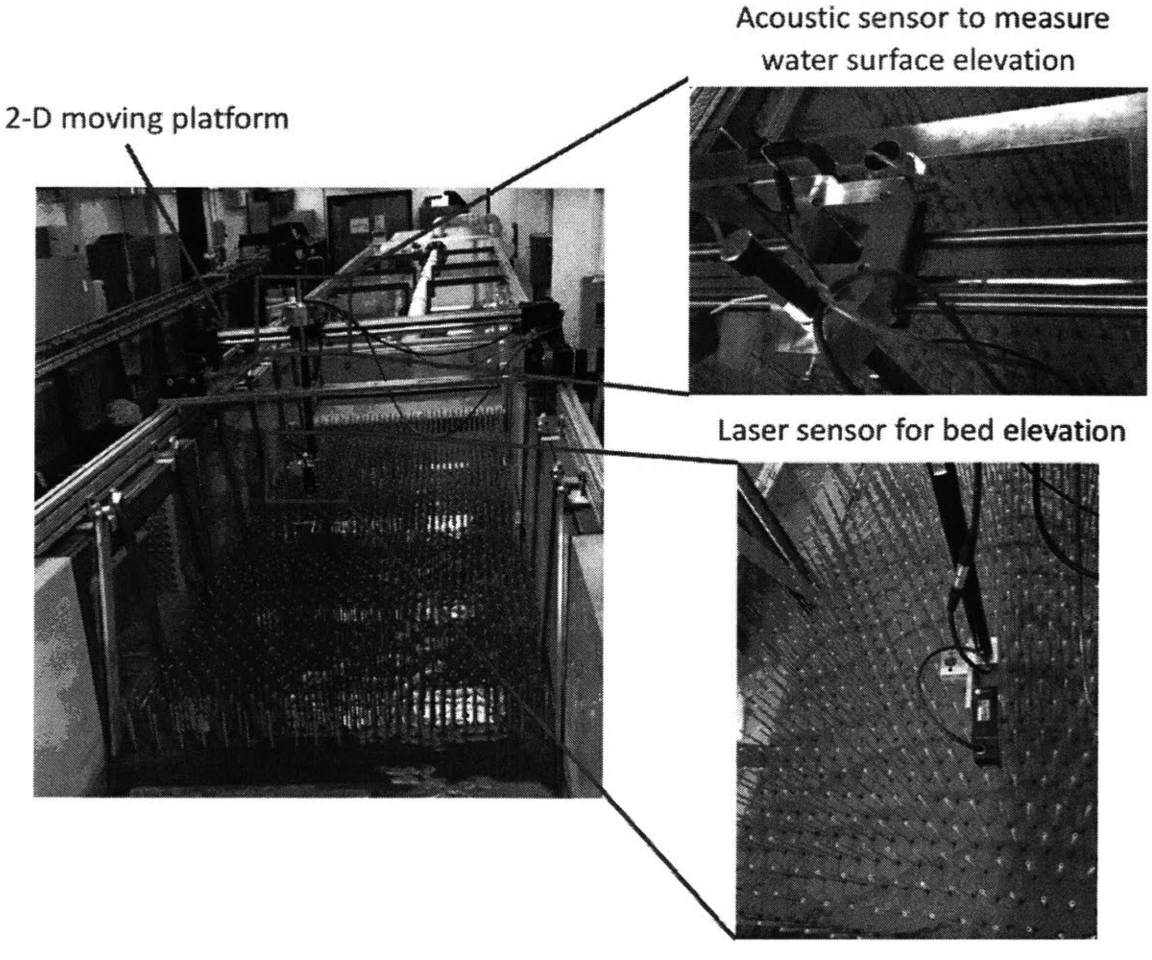

Figure C-1: Bed topography system

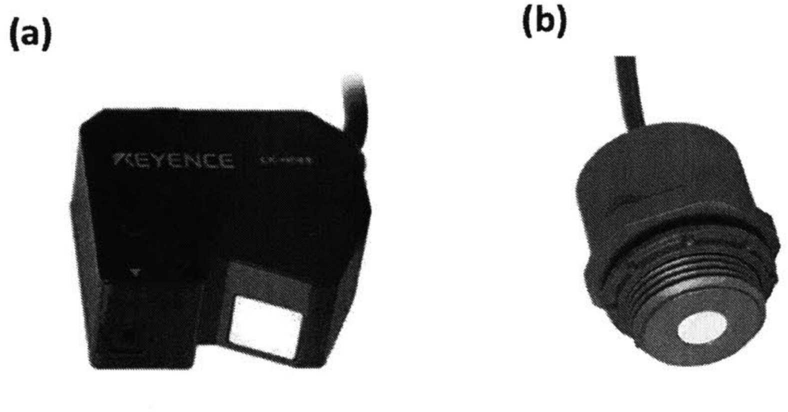

Figure C-2: Laser sensor and acoustic sensor images

(a) The Keyence laser sensor. (b) The Omega acoustic sensor.

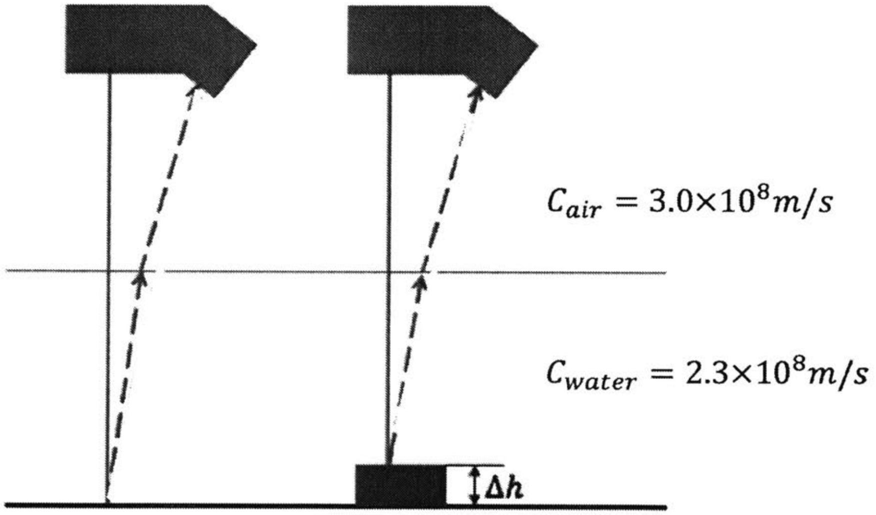

Figure C-3: Laser topography sensor with water

To measure the topography without draining water, the difference in the speed of light in air and in water was corrected. The blue box indicate the laser topography sensor. The solid red lines indicate the light emitted from the sensor and the dashed red lines indicate the light signal scattered from the bottom and received by the sensor receptor. Note that the temperature effects on the light speed is negligible.

The Omega acoustic sensor measures the distance from the sensor head to the water surface, the output is a voltage signal. To calibrate the sensor, the distance from the sensor head to the water surface was varied and measured using a ruler, while the sensor voltage was recorded. The measured distance versus the acoustic sensor output in voltage was plotted in Figure C-4.

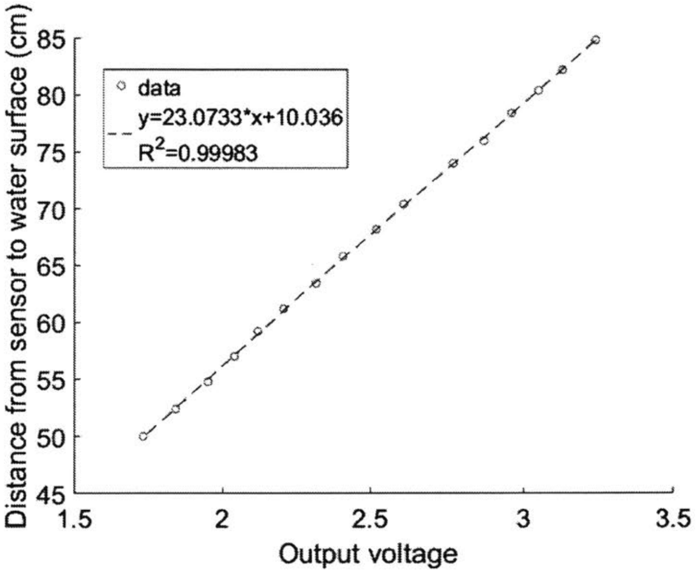

Figure C-4: Calibration of the water surface sensor

This figure is from the research report of an undergraduate research assistant Milani Chatterji-Len. Since the original data is not available, no error bars and errors of the fitting parameters are reported here.

C.2 The automatic control platform in LabVIEW

In order to make the system automatic, the two sensors and the moving system were integrated into the LabVIEW platform. The LabVIEW interface is shown in Figure C-5. The block diagram of the designed LabVIEW control system is shown in Figure C-6 and C-7.

C.3 Procedure for measuring bed topography

Step 1: Connect the sensors wires to power and the Dell computer with the installed labview software, open the labview '.vi' file in LabVIEW, as shown in Figure C-8.

Step 2: Type the names of the files you want to save in LabVIEW in box 1 (Figure C-9).

Step 3: Decide how many steps or positions you want to measure and type in box 2. In box 3, type how long is each step. For example, if you want the topography sensor to move 10mm in x direction per step, then change line 2 of the code in "Sensors go forward" to "PRX=7817" , because 781.7 for the step motor of the system is 1mm. Similarly, change line 2 of the code in "Sensors go backward" to "PRX=-7817". If you want to move 50mm in y direction per step for 6 steps, change line 2 of the code in "Y-direction-code" to "PRY=39085", as $781.7 \times 50 \approx 39805$. Then change line 2 of the code in "Y-direction-code" to "PRY=-234510", which is $781.7 \times 50 \times 6$.

C.4 Troubleshooting

Symptom 1: the topography sensor stops without finishing the scanning.

Possible reason: the connection of the cable to the laser sensor controller is loose (the red box in Figure C-10).

Remedy: please gently fix the connection using tapes or other tools.

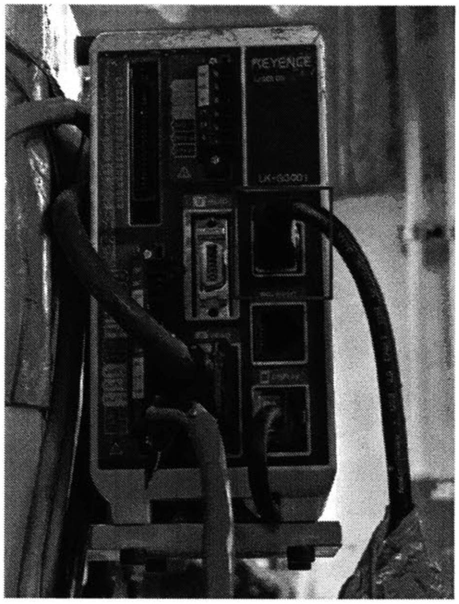

Figure C-10: Topography system troubleshooting

The controller of the Keyence Laser sensor. The red box shows the connect to the computer.

Symptom 2: the recorded topography data has a large amount of infinite values.

Possible reason 1: the water in the flume is too dirty. Remedy: replace the water, clean the flume regularly.

Possible reason 2: if the topography changed too much, it is possible that the distance is outside the range of the laser sensor.

The Keyence laser sensor measures light scattered at surfaces located 30-50cm from the laser head (more specifics about the sensor can be found in:

https://www.keyence.com/products/measure/laser-1d/lk-g3000/models/lk-g402/index.jsp

Therefore, in order for the laser sensor to work properly, the water surface should be less than 30cm from the laser head and the distance of the channel bottom to the sensor head, with the travel distance in the water corrected by the water reflection index, should be within 30-50cm.

C.5 Codes for bed topography

1. Both_sensor_2D_wet.m

```
%Processing laser height sensor calculations
clear,clc;
close all;
dx_step = 7817*1/781.7; %mm
dy_step = 7817*5/781.7; %mm
I = 25.5; % approximate in cm, distance for sensor to water surface
h_water = 35+125; %35+125; %mm, need to change to your measured water depth
%Read depth data and find coefficients and remove noisy data
data = xlsread('Top_2D_a0_4Ucrit_slope_3hours_p4.xls');
non_inf_rate = xlsread('Laser_non_inf_a0_4Ucrit_slope_3hours_p4.xls');
inf_index = find(non_inf_rate/100¡0.4);
% data(inf_index) = NaN;
no_data_rate = numel(find(isnan(data)))./numel(data);
data = fillmissing(data,'linear');
% linearly interpolate this missing data for each no-data point
for i = 1:numel(data(1,:))
data(:,i) = medfilt1(data(:,i)) ;
end
for i = 1:numel(data(:,1))
data(i,:) = medfilt1(data(i,:)) ;
end
%%%% correct for data edge
Top_read = zeros(numel(data(:,1))-1,numel(data(1,:)));
Top_read(:, 1:2:numel(data(1,:))) = data(1:numel(data(:,1))-1, 1:2:numel(data(1,:)));
Top_read(:, 2:2:numel(data(1,:))) = data(2:numel(data(:,1)), 2:2:numel(data(1,:)));
%%%% correct for data edge
```

```
h_top = (Top_read - 9.739*I-4.510)/7.418*10; %in mm
% generate grid point
[Xpt,Ypt] = meshgrid(dx_step*[1:numel(data(:,1))-1],80+dy_step*[0:numel(data(1,:))-1]);
Xpt = Xpt’;
Ypt = Ypt’;
%Read surfaceh data and find coefficients
data2 = xlsread(’Surface_2D_a0_4Ucrit_slope_3hours_p4.xls’);
%%%% correct for data edge
Surface_v = zeros(numel(data2(:,1))-1,numel(data2(1,:)));
Surface_v(:, 1:2:numel(data2(1,:))) = data2(1:numel(data2(:,1))-1, 1:2:numel(data2(1,:)));
Surface_v(:, 2:2:numel(data2(1,:))) = data2(2:numel(data2(:,1)), 2:2:numel(data2(1,:)));
%%%% correct for data edge
dis_water_sensor = 10*(23.0733*Surface_v+10.03); % in mm, the coefficients 23.0733 and 10.03 were obtained by milani chatterji-len and theoritically should not change with the configuration
for i = 1:numel(data2(1,:))
data2(:,i) = medfilt1(data2(:,i)) ;
end
for i = 1:numel(data2(:,1))
data2(i,:) = medfilt1(data2(i,:)) ;
end
Colorset = ’b’,’r’,’b’,’r’,’b’,’r’,’b’,’r’,’b’,’r’,’b’,’r’,’b’,’r’,’b’,’r’; % Cell array of colros.
color_gradient = jet(numel(data(1,:)));
%% Plot the topograph
figure; hold on
set(gca,’FontSize’,20);
colormap(jet)
surf(Xpt, Ypt, h_water-h_top)
% surf(Xpt, Ypt,405-Top_read)
```

```
view(45,30)
set(gca,’PlotBoxAspectRatio’,[1 1 1]);
xlabel(’x/mm’)
ylabel(’y/mm’)
zlabel(’depth/mm’)
% axis([0 inf 0 inf])
xlim([0 inf])
colorbar
title(’Topo 2D’)
%% Plot topography in x-direction for each y position (1D)
figure;
subplot(2,1,1)
hold on
set(gca,’FontSize’,20);
for i = 1 :numel(h_top(1,:))
plot(Xpt(:,i), h_water-h_top(:,i),’+-’,’color’,color_gradient(i,:))
leg_xi = [’y=’,num2str(i*dx_step/10),’cm’];
p = polyfit(Xpt(:,i), h_water-h_top(:,i),1);
slope_x(i) = p(1);
leg_xi = [’y=’,num2str(i*dy_step/10),’cm, s=’,num2str(slope_x(i),2)];
y_fit = polyval(p, Xpt(:,i));
plot(Xpt(:,i),y_fit,’–’,’color’,color_gradient(i,:))
end
% legend(leg_x);
xlabel(’x/mm’)
ylabel(’depth/mm’)
% axis([0 inf 0 inf])
xlim([0 inf])
colorbar
title(’Topo along x’)
```

```
subplot(2,1,2)
hold on
set(gca,’FontSize’,20);
for i = 1 :numel(h_top(1,:))
Bedform(:,i) = h_water-h_top(:,i)-y_fit;
plot(Xpt(:,i), h_water-h_top(:,i)-y_fit,’s’,’color’,color_gradient(i,:))
[xData, yData] = prepareCurveData( Xpt(:,i), Bedform(:,i) );
% Set up fittype and options.
ft = fittype( ’sin1’ );
opts = fitoptions( ’Method’, ’NonlinearLeastSquares’ );
opts.Display = ’Off’;
opts.Lower = [-Inf 0 -Inf];
opts.StartPoint = [3.78865588272251 0.0392699081698724 -1.03402580803018];
% Fit model to data.
[fitresult, gof] = fit( xData, yData, ft, opts );
fitresult
ripple_A(i) = fitresult.a1;
ripple_lambda(i) = 2*pi/fitresult.b1;
% Plot fit with data.
% hh = plot( fitresult, xData, yData );
% set(hh,’color’,color_gradient(i,:),’MarkerSize’,9)
end
legend(leg_x);
xlabel(’x/mm’)
ylabel(’depth/mm’)
% axis([0 inf 0 inf])
xlim([0 inf])
colorbar
title(’Bed forms’)
%% Find the period of the ripples
```

```
figure; hold on
set(gca,’Fontsize’,20)
for i = 1 :numel(h_top(1,:))
f_bed_x(i) = 1/mean(diff(Xpt(:,i)));
amplitude(i) = std(Bedform(:,i));
[autocori,lagsi] = xcorr(Bedform(:,i),’coeff’)
lags_autoi = lagsi/f_bed_x(i);
plot(lags_autoi ,autocori,’color’,color_gradient(i,:),’Linewidth’,2’)
[pksi,locsi] = findpeaks(autocori)
bed_legi = [’SD=’,num2str(amplitude(i),2),’mm’]
end
legend(bed_leg)
L = get(gca,’xlim’)
set(gca,’Xtick’,[-500:100:500])
xlabel(’Lag (mm)’)
ylabel(’Autocorrelation’);
title(’a=2.5m^-^1, 3Ucrit’)
color_gradient2 = jet(numel(data(:,1)));
%% Plot topography in x-direction for each y position (1D)
figure; hold on
set(gca,’FontSize’,20);
for i = 1:numel(h_top(:,1))
plot(Ypt(i,:), h_water-h_top(i,:),’+-’,’color’,color_gradient2(i,:))
leg_yi = [’x=’,num2str(i*dy_step/10),’cm’];
end
legend(leg_y)
xlabel(’y/mm’)
ylabel(’depth/mm’)
% axis([0 inf 0 inf])
xlim([0 inf])
```

```
colorbar
title(’Topo along Y’)
%% Plot the water surface (2D)
figure; hold on
set(gca,’FontSize’,20);
colormap(jet)
surf(Xpt, Ypt,dis_water_sensor)
view(45,30)
set(gca,’PlotBoxAspectRatio’,[1 1 1]);
xlabel(’x/mm’)
ylabel(’y/mm’)
zlabel(’Distance /mm’)
% axis([0 inf 0 inf])
xlim([0 inf])
colorbar
title(’From acoustic sensor to water surface 2D’)
%% Plot water_elevation in x-direction for each y position (1D)
figure; hold on
set(gca,’FontSize’,20,’Linewidth’,2);
for i = 1:numel(h_top(1,:))
plot(Xpt(:,i), dis_water_sensor(:,i),’o:’,’color’,color_gradient(i,:),’MarkerSize’,9,’Linewidth’,2)
end
legend(leg_x);
xlabel(’x/mm’)
ylabel(’Distance/mm’)
% axis([0 inf 0 inf])
xlim([0 inf])
title(’From acoustic sensor to water surface along x’)
%% Plot water_elevation in y-direction for each x position (1D)
figure; hold on
```

```
set(gca,’FontSize’,20,’Linewidth’,2);
color_2 = jet(numel(data(:,1)));
for i = 1:numel(h_top(:,1))
plot(Ypt(i,:), dis_water_sensor(i,:),’o:’,’color’,color_2(i,:),’MarkerSize’,9,’Linewidth’,2)
end
legend(leg_y)
xlabel(’y/mm’)
ylabel(’Distance/mm’)
% axis([0 inf 0 inf])
xlim([0 inf])
title(’From acoustic sensor to water surface along y’)
```

2. Both_sensor_2D_surface.m

```
% Processing laser height sensor calculations
clear,clc;
close all;
dx_step = 7817*1/781.7; % mm
dy_step = 7817*50/781.7; % mm
I = 28.7; % approximate in cm, distance for sensor to glass
h_surface_sensor = 481.7; % mm
% Read surfaceh data and find coefficients
data2 = xlsread(’Surface_2D_only_a0_4_Ucrit_2_5hrs_p2.xls’);
% linearly interpolate this missing data for each no-data point
for i = 1:numel(data2(1,:))
data2(:,i) = medfilt1(data2(:,i)) ;
end
for i = 1:numel(data2(:,1))
data2(i,:) = medfilt1(data2(i,:)) ;
end
% % % % correct for data edge
Surface_v = zeros(numel(data2(:,1))-1,numel(data2(1,:)));
```

```
Surface_v(:, 1:2:numel(data2(1,:))) = data2(1:numel(data2(:,1))-1, 1:2:numel(data2(1,:)));
Surface_v(:, 2:2:numel(data2(1,:))) = data2(2:numel(data2(:,1)), 2:2:numel(data2(1,:)));
% % % % correct for data edge
dis_water_sensor = 10*(23.0733*Surface_v+10.03);
% in mm, the coefficients 23.0733 and 10.03 were obtained by
% milani chatterji-len and theoritically should not change with the configuration
h_water_2D = h_surface_sensor - dis_water_sensor;
% generate grid point
[Xpt,Ypt] = meshgrid(dx_step*[1:numel(data2(:,1))-1],80+dy_step*[0:numel(data2(1,:))-1]);
Xpt = Xpt’;
Ypt = Ypt’;
Colorset = ’b’,’r’,’b’,’r’,’b’,’r’,’b’,’r’,’b’,’r’,’b’,’r’,’b’,’r’,’b’,’r’; % Cell array of colros.
color_gradient = jet(numel(data2(1,:)));
% % Plot the water surface (2D)
figure; hold on
set(gca,’FontSize’,20);
colormap(jet)
surf(Xpt, Ypt,h_water_2D)
view(45,30)
set(gca,’PlotBoxAspectRatio’,[1 1 1]);
xlabel(’x/mm’)
ylabel(’y/mm’)
zlabel(’Distance /mm’)
% axis([0 inf 0 inf])
xlim([0 inf])
colorbar
title(’From acoustic sensor to water surface 2D’)
% % Plot water_elevation in x-direction for each y position (1D)
figure; hold on
```

```
set(gca,’FontSize’,20,’Linewidth’,2);
lineset = ’bo’,’rx’,’cs’,’mp’
for i = 1:numel(h_water_2D(1,:))
h(i) = plot(Xpt(:,i), h_water_2D(:,i),lineseti,’MarkerSize’,9,’Linewidth’,2)
leg_xi = [’y=’,num2str(i*dx_step/10),’cm’];
p = polyfit(Xpt(:,i), h_water_2D(:,i),1);
slope_x(i) = p(1);
leg_xi = [’y=’,num2str(i*dx_step/10),’cm, s=’,num2str(slope_x(i),2)];
yfit = polyval(p,Xpt(:,i));
plot(Xpt(:,i),yfit,’g–’)
end
legend(h,leg_x);
xlabel(’x/mm’)
ylabel(’Distance/mm’)
% axis([0 inf 0 inf])
xlim([0 inf])
title(’From acoustic sensor to water surface along x’)
% % Plot water_elevation in y-direction for each x position (1D)
figure; hold on
set(gca,’FontSize’,20,’Linewidth’,2);
color_2 = jet(numel(data2(:,1)));
for i = 1:numel(h_water_2D(:,1))
plot(Ypt(i,:), h_water_2D(i,:),’o:’,’color’,color_2(i,:),’MarkerSize’,9,’Linewidth’,2)
end
% legend(leg_y)
xlabel(’y/mm’)
ylabel(’Distance/mm’)
% axis([0 inf 0 inf])
xlim([0 inf])
title(’From acoustic sensor to water surface along y’)
```

Figure C-5: The designed LabVIEW interface.

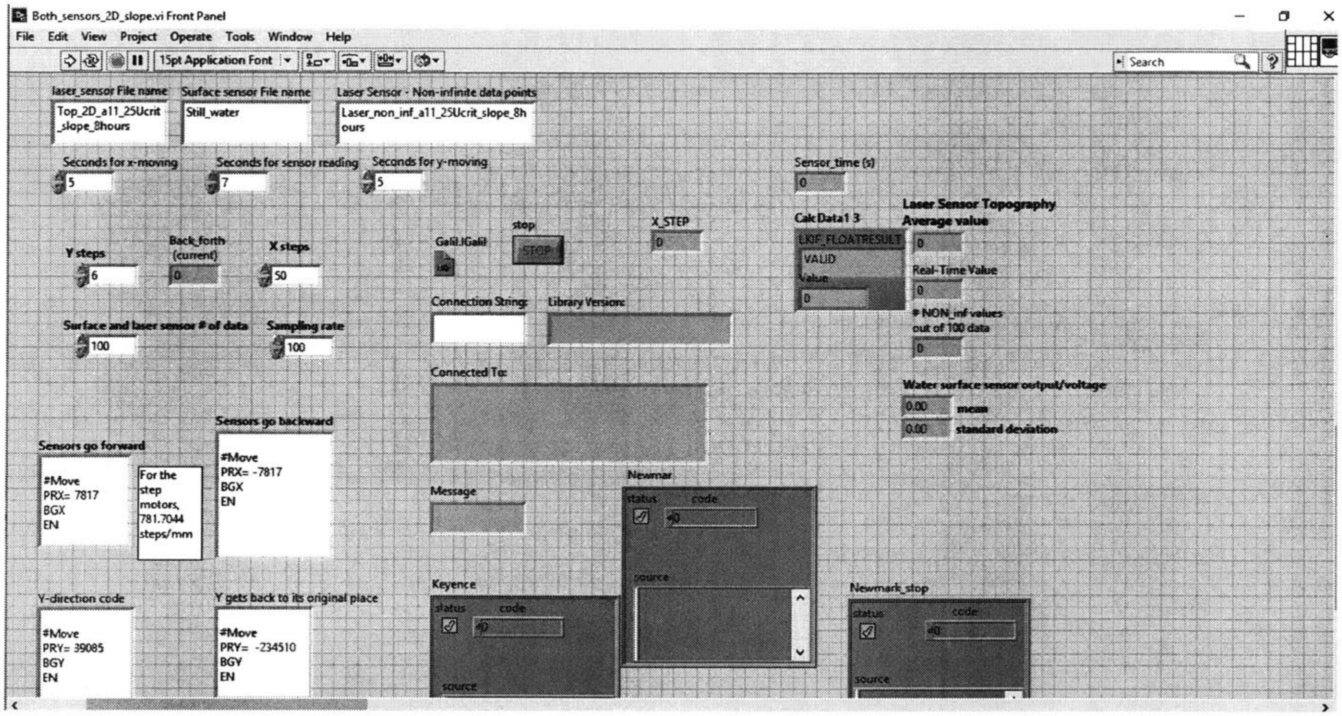

laser_sensor File name: Top_2D_a11_25Ucrit_slope_8hours

Surface sensor File name: Still_water

Laser Sensor - Non-infinite data points: Laser_non_inf_a11_25Ucrit_slope_8hours

Seconds for x-moving: 5

Seconds for sensor reading: 7

Seconds for y-moving: 5

Y steps: 6

Back_forth (current): 0

X steps: 50

Surface and laser sensor # of data: 100

Sampling rate: 100

X_STEP: 0

Connection String:

Library Version:

Connected To:

Message

Sensor_time (s): 0

Calc Data1 3: LKIF_FLOATRESULT VALID; Value: 0

Laser Sensor Topography Average value: 0

Real-Time Value: 0

NON_inf values out of 100 data: 0

Water surface sensor output/voltage

0.00 mean

0.00 standard deviation

Newmar: status ☑ code 0; source

Keyence: status ☑ code 0; source

Newmark_stop: status ☑ code 0; source

Sensors go forward

```
#Move
PRX= 7817
BGX
EN
```

For the step motors, 781.7044 steps/mm

Sensors go backward

```
#Move
PRX= -7817
BGX
EN
```

Y-direction code

```
#Move
PRY= 39085
BGY
EN
```

Y gets back to its original place

```
#Move
PRY= -234510
BGY
EN
```

Figure C-6: The left part of the designed LabVIEW block diagram.

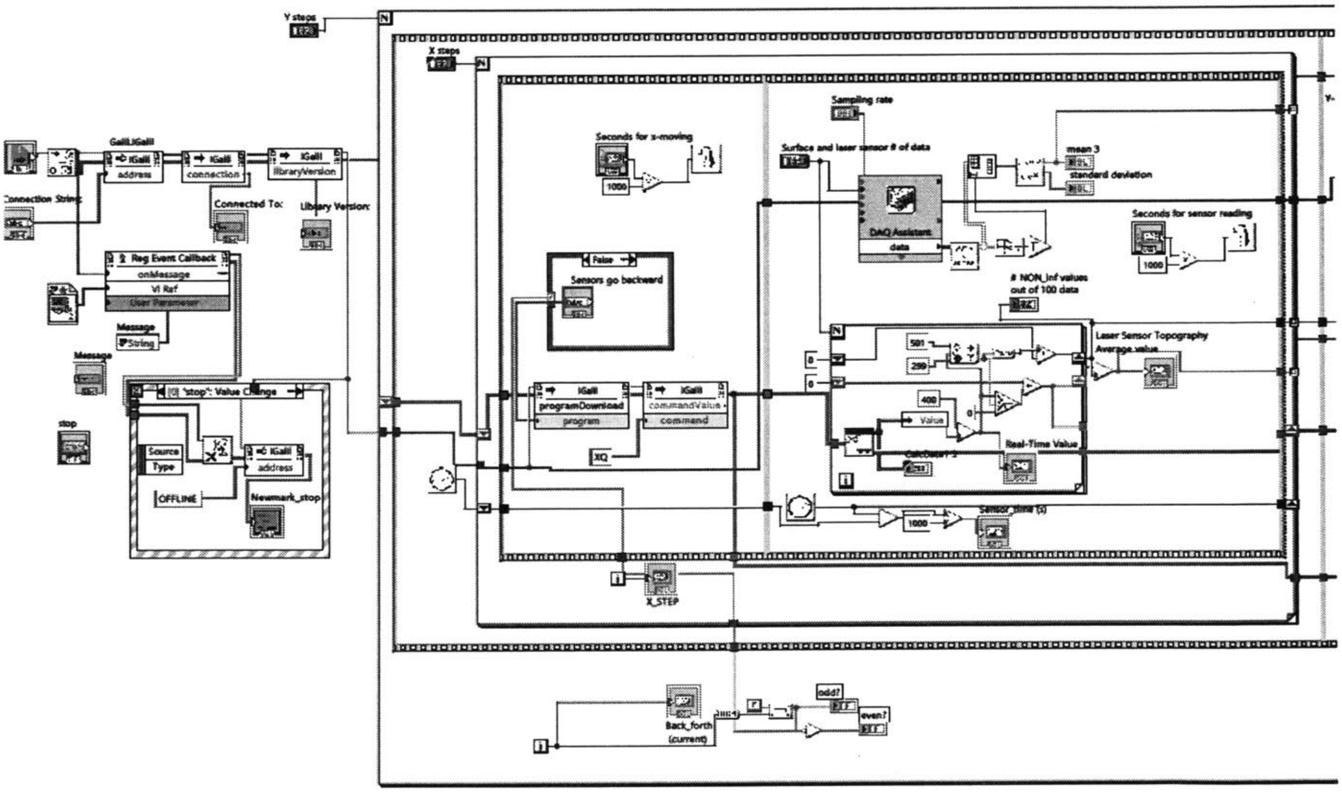

Figure C-7: The right part of the designed Labview block diagram.

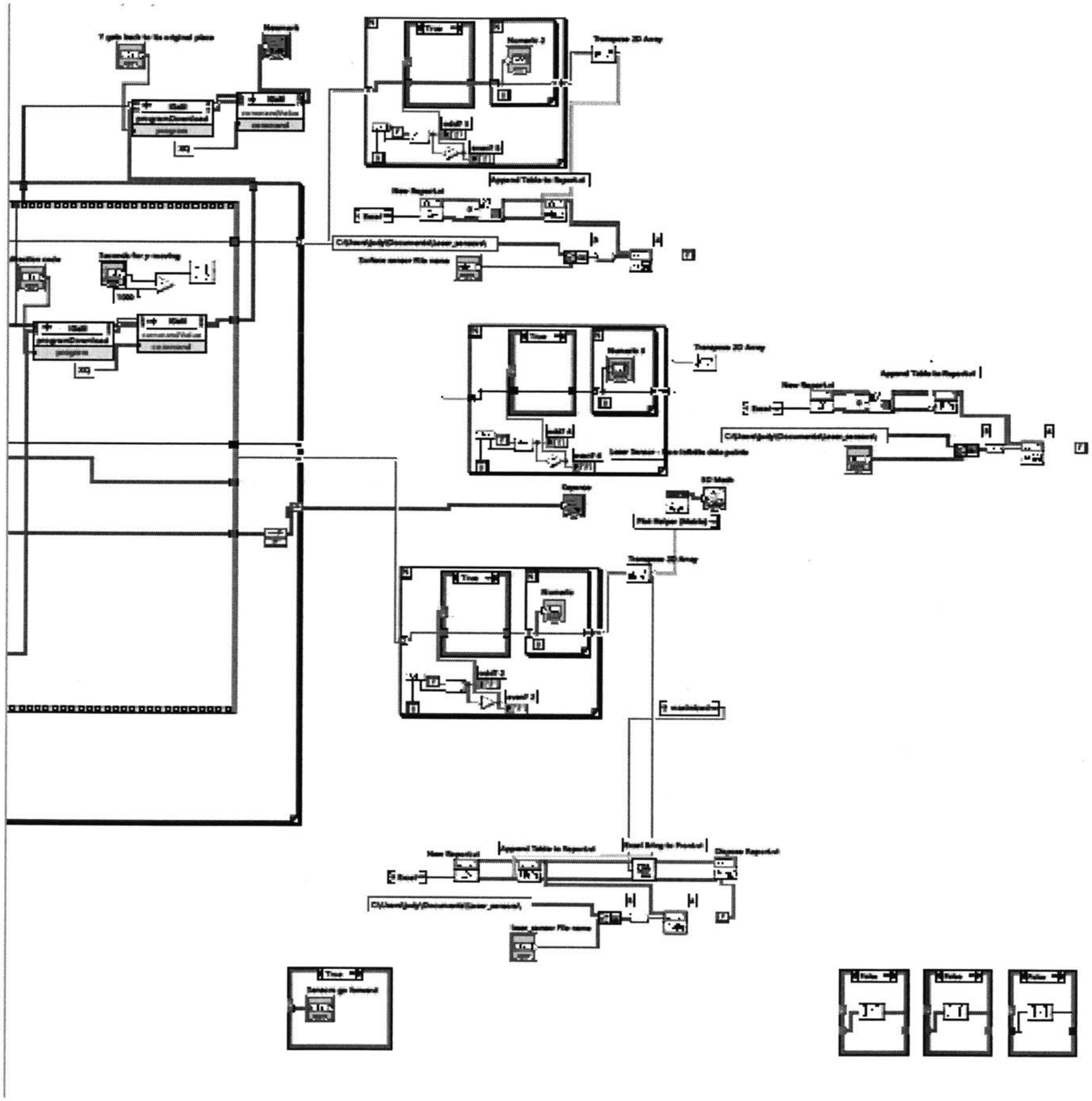

Figure C-8: The vi file.

Both_sensors_2D_slope.vi

Figure C-9: LabVIEW settings.

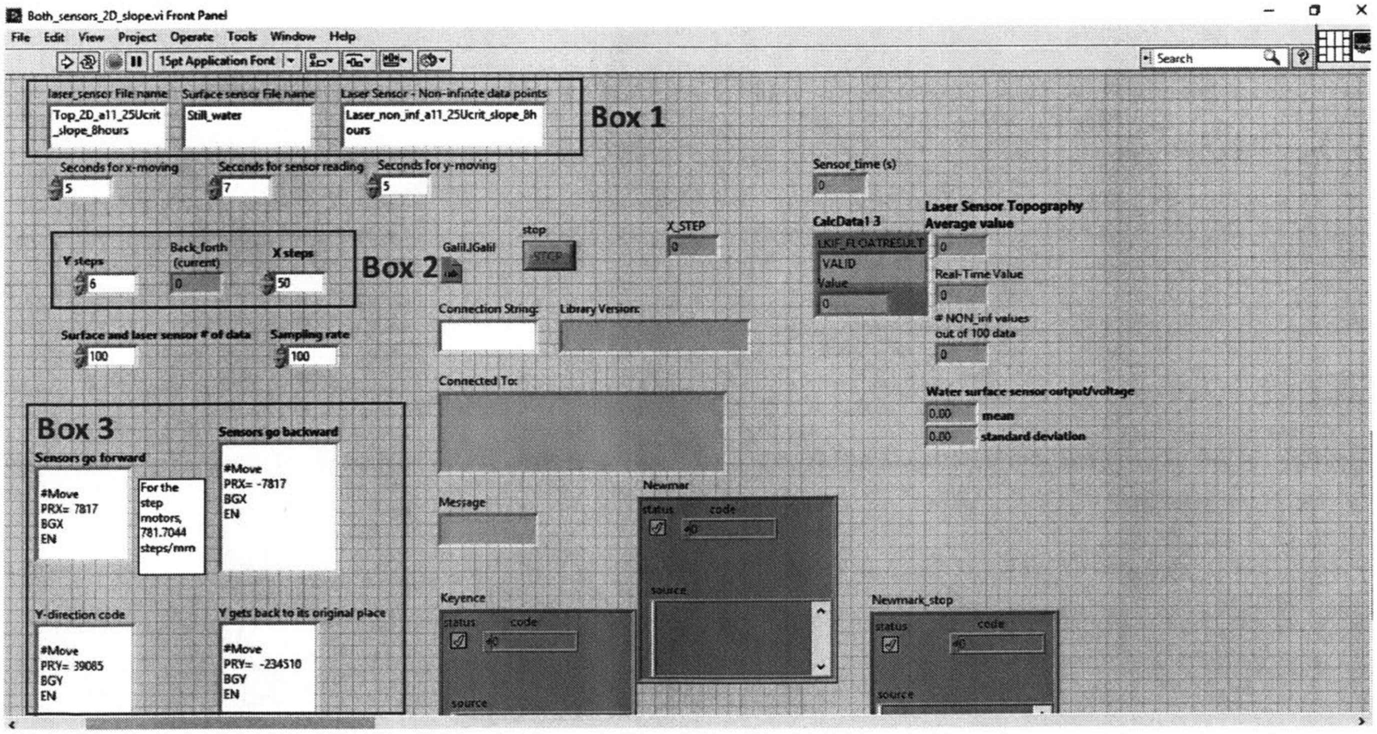

laser_sensor File name: Top_2D_a11_25Ucrit_slope_8hours

Surface sensor File name: Still_water

Laser Sensor - Non-infinite data points: Laser_non_inf_a11_25Ucrit_slope_8hours

Seconds for x-moving: 5

Seconds for sensor reading: 7

Seconds for y-moving: 5

Y steps: 6

Back_forth (current): 0

X steps: 50

Surface and laser sensor # of data: 100

Sampling rate: 100

Connection String:

Library Versions:

Connected To:

Message:

X_STEP: 0

Sensor_time (s): 0

CalcData1 3: LKIF_FLOATRESULT VALID Value 0

Laser Sensor Topography Average value: 0

Real-Time Value: 0

NON_inf values out of 100 data: 0

Water surface sensor output/voltage

0.00 mean

0.00 standard deviation

Keyence: status ✓ code 0

Newmar: status ✓ code 0

Newmark_stop: status ✓ code 0

Sensors go forward

```
#Move
PRX= 7817
BGX
EN
```

For the step motors, 781.7044 steps/mm

Sensors go backward

```
#Move
PRX= -7817
BGX
EN
```

Y-direction code

```
#Move
PRY= 39085
BGY
EN
```

Y gets back to its original place

```
#Move
PRY= -234510
BGY
EN
```

Appendix D

The turbulent kinetic energy and Reynolds stress profiles

This section shows the turbulent kinetic energy and Reynolds stress profiles measured over the mobile bed which are discussed in Chapters 3 and 4. The experimental conditions for each case are listed in Table 4.1 and copied below. The circles in the following figures indicate individual measurement at one position and the black circles connected by dashed lines represent the spatial average (the mean and the standard deviation) of the measurements for different distances from the bed. $z = 0$ represents the mean bed, and only measurements with 20 to $30mm$ from the mean bed were plotted. The titles in the figures show the average and standard error of k_t/U^2 between z = 20 to $30mm$. Because the standard errors of k_t/U^2 were small and almost zero for some cases, 2 significant digits were given to the standard errors for future reference.

Table D.1: Copy of Table 4.1

Case number	a $[m^{-1}]$	ϕ	U $[m/s]$	h $[m]$	$Q_s \pm \sigma_{Q_s}$ $[g/(m \cdot s)]$	$k_t \pm \sigma_{k_t}$ $[cm^2/s^2]$	$(\tau_{RS} \pm \sigma_{RS})/\rho$ $[cm^2/s^2]$
Bare channels							
1.1	0	0	0.42	0.12	0.36 ± 0.05	28 ± 1 (8)	3.9 ± 0.2
1.2	0	0	0.47	0.12	1.84 ± 0.08	46 ± 1 (34)	6.0 ± 0.2
1.3	0	0	0.65	0.12	24 ± 1	111 ± 11 (8)	14.7 ± 1.3
1.4	0	0	0.88	0.12	134 ± 8	205 ± 10 (8)	12.8 ± 1.6
Channels with model emergent vegetation							
2.1	1.1	0.005	0.27	0.12	0.5 ± 0.1	19 ± 3 (24)	0.5 ± 0.2
2.2	1.1	0.005	0.30	0.12	2.5 ± 0.3	20 ± 2 (24)	0.2 ± 0.2
2.3	1.1	0.005	0.34	0.12	9 ± 1	32 ± 5 (24)	1.9 ± 0.5
2.4	1.1	0.005	0.43	0.12	68 ± 17	65 ± 8 (24)	6.2 ± 0.7
3.1	2.5	0.012	0.21	0.12	0.15 ± 0.02	17 ± 2 (27)	0.5 ± 0.1
3.2	2.5	0.012	0.24	0.12	2.6 ± 0.5	22 ± 2 (27)	0.1 ± 0.1
3.3	2.5	0.012	0.28	0.12	9.4 ± 0.6	45 ± 5 (27)	2.0 ± 0.6
4.1	5.1	0.025	0.21	0.10	1.3 ± 0.1	20 ± 2 (23)	0.5 ± 0.1
4.2	5.1	0.025	0.23	0.10	2.9 ± 0.3	42 ± 4 (23)	0.1 ± 0.1
4.3	5.1	0.025	0.27	0.10	17 ± 1	46 ± 4 (23)	1.0 ± 0.2
4.4	5.1	0.025	0.31	0.10	41 ± 2	51 ± 5 (23)	1.6 ± 0.3

Figure D-1: Case 1.1, the turbulent kinetic energy profile

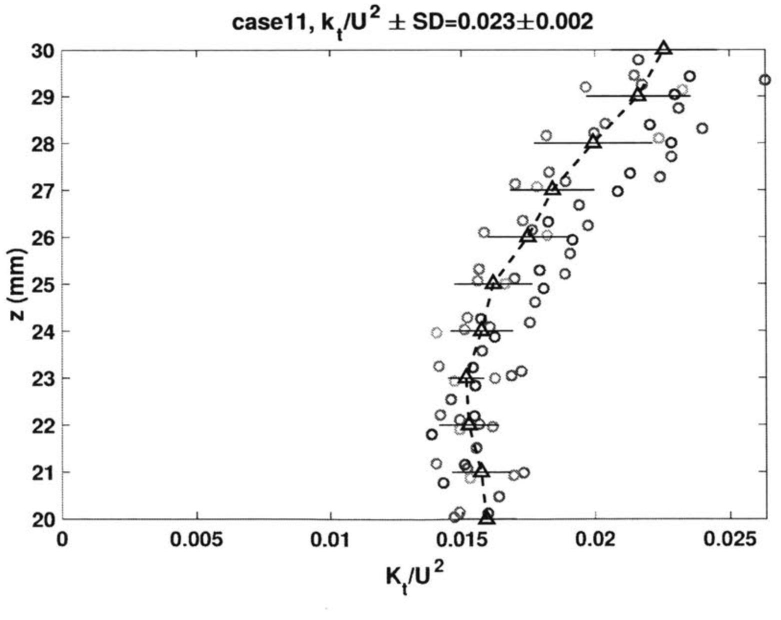

Figure D-2: Case 1.1, the Reynolds stress profile

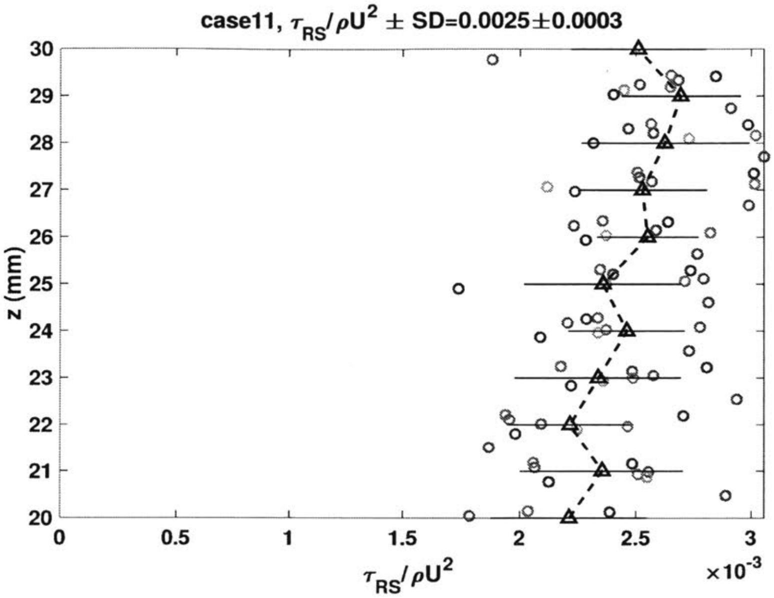

Figure D-3: Case 1.2, the turbulent kinetic energy profile

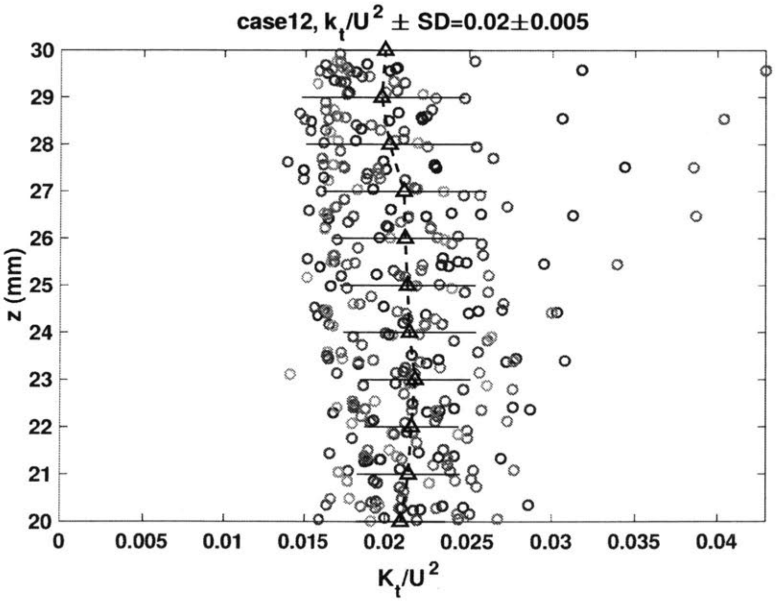

Figure D-4: Case 1.2, the Reynolds stress profile

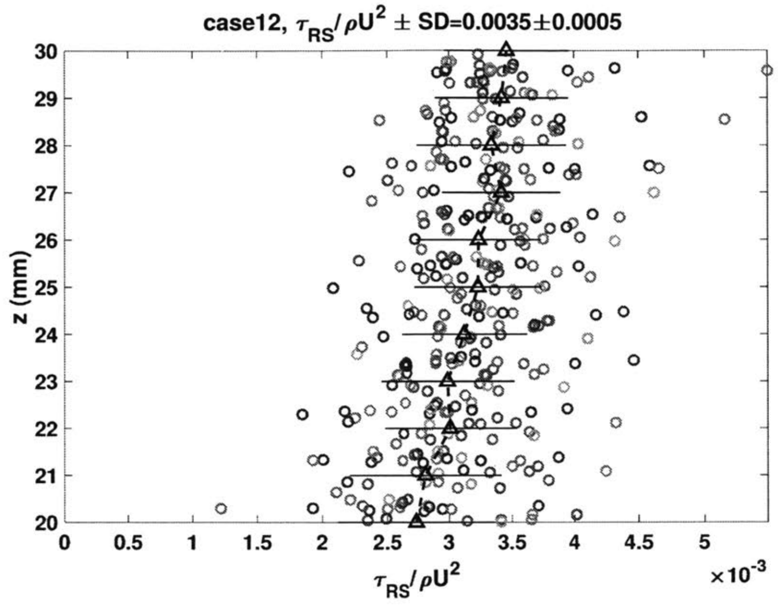

Figure D-5: Case 1.3, the turbulent kinetic energy profile

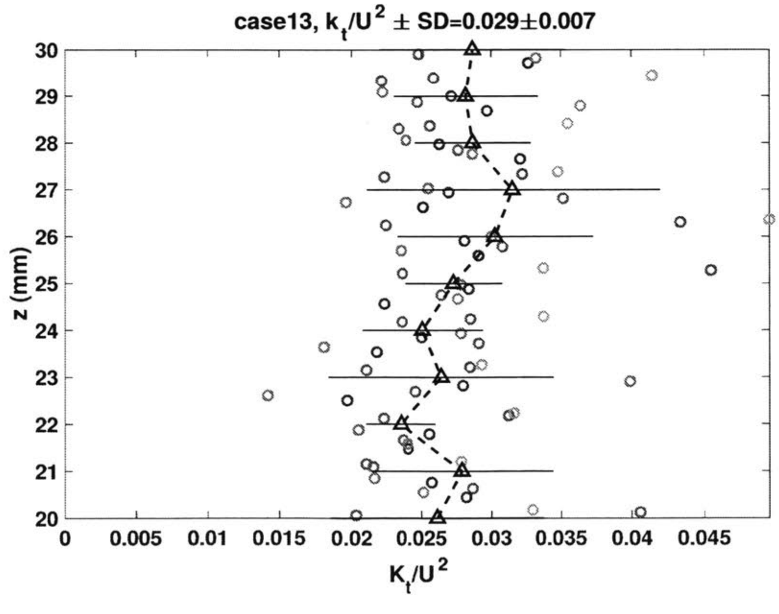

Figure D-6: Case 1.3, the Reynolds stress profile

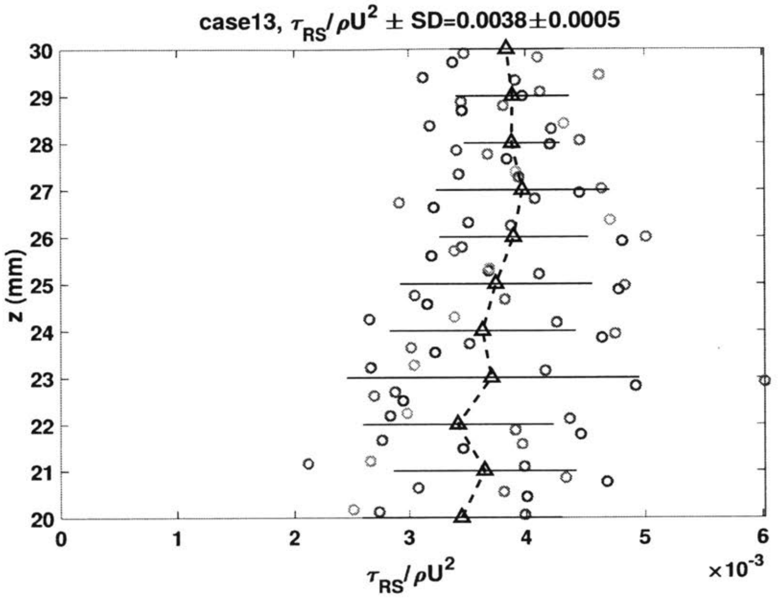

Figure D-7: Case 1.4, the turbulent kinetic energy profile

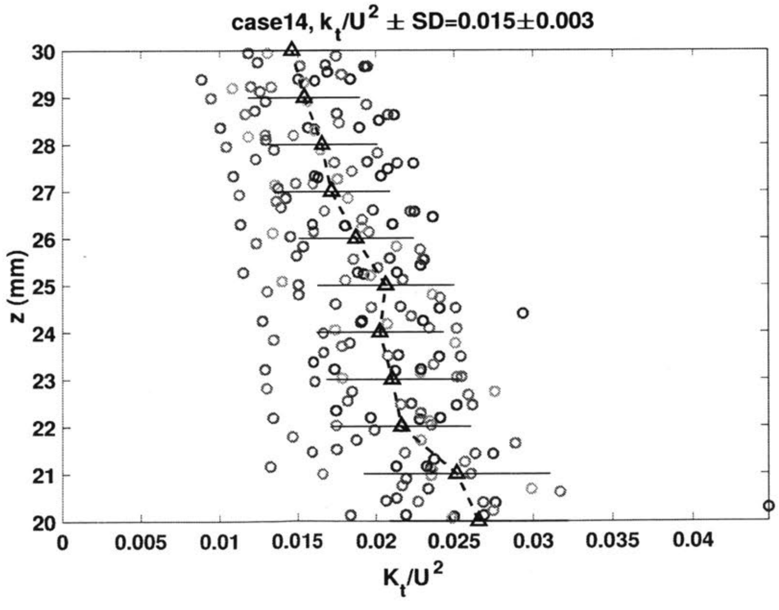

Figure D-8: Case 1.4, the Reynolds stress profile

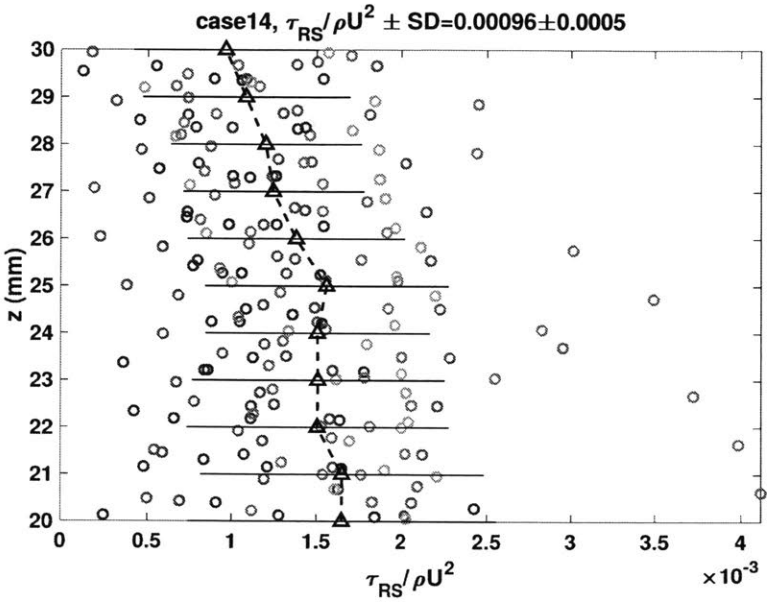

Figure D-9: Case 2.1, the turbulent kinetic energy profile

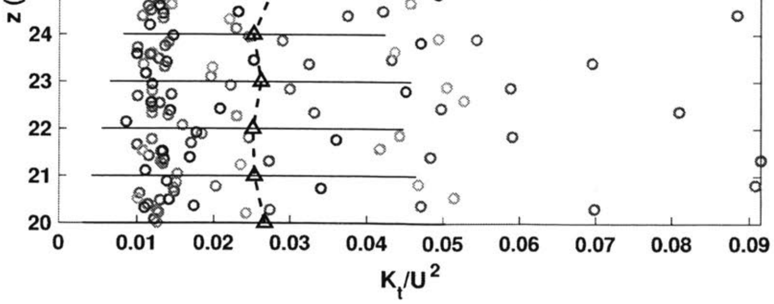

Figure D-10: Case 2.1, the Reynolds stress profile

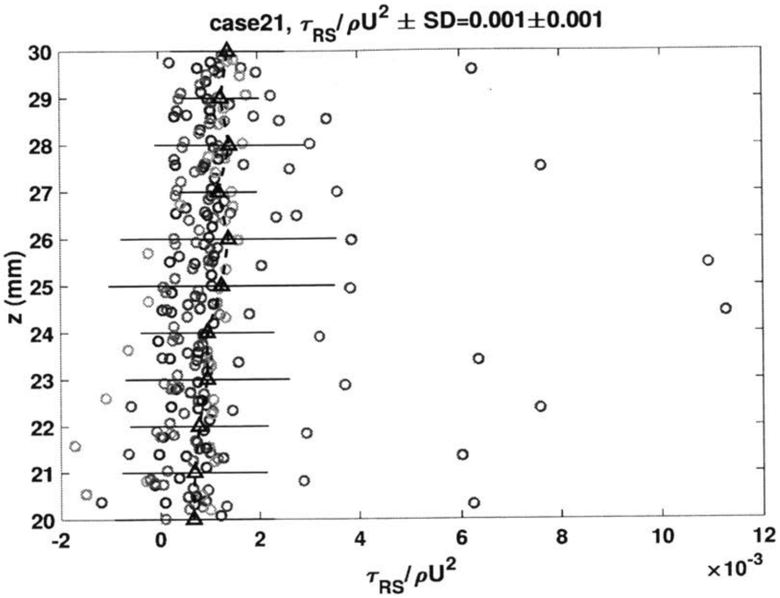

Figure D-11: Case 2.2, the turbulent kinetic energy profile

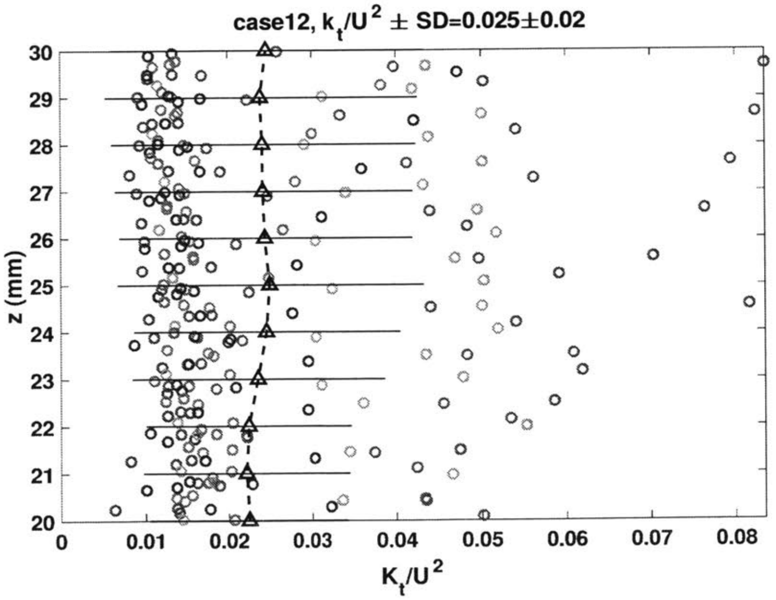

Figure D-12: Case 2.2, the Reynolds stress profile

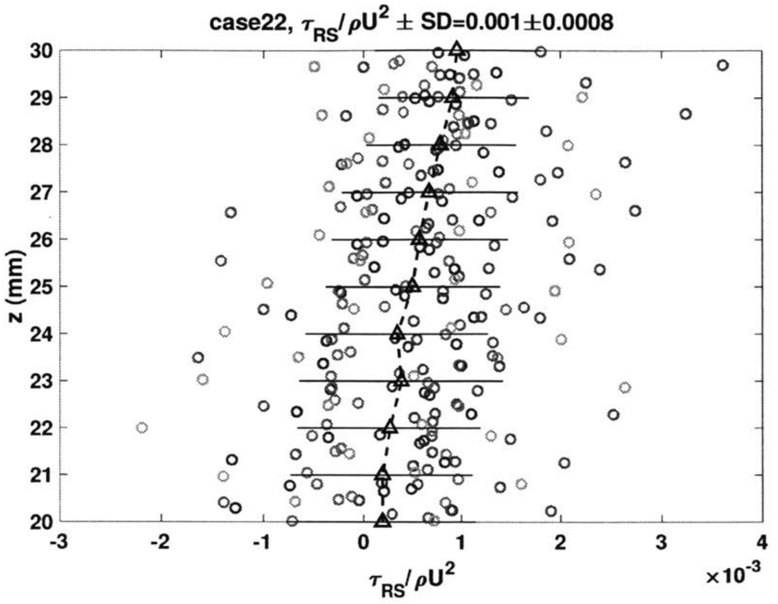

Figure D-13: Case 2.3, the turbulent kinetic energy profile

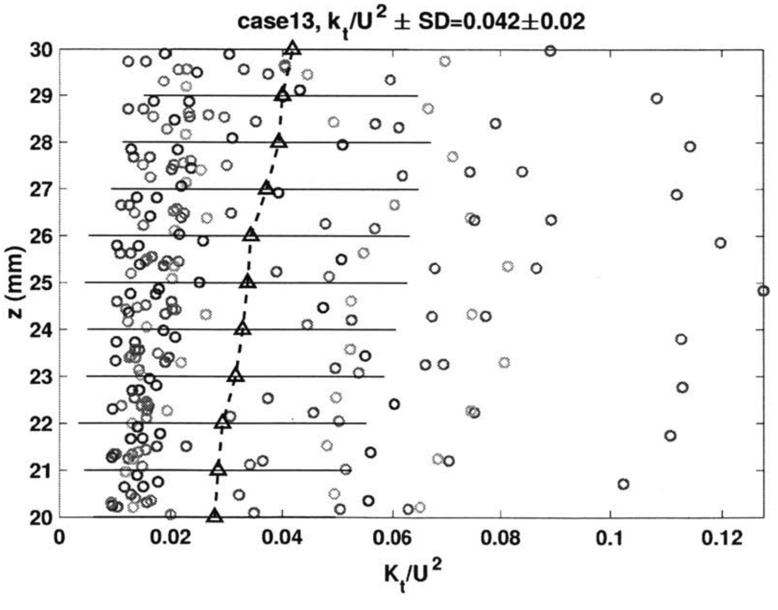

Figure D-14: Case 2.3, the Reynolds stress profile

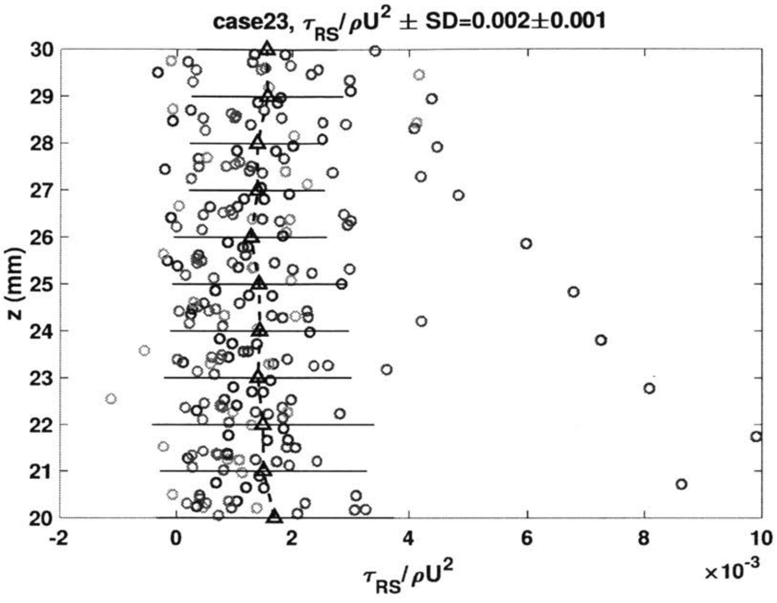

Figure D-15: Case 2.4, the turbulent kinetic energy profile

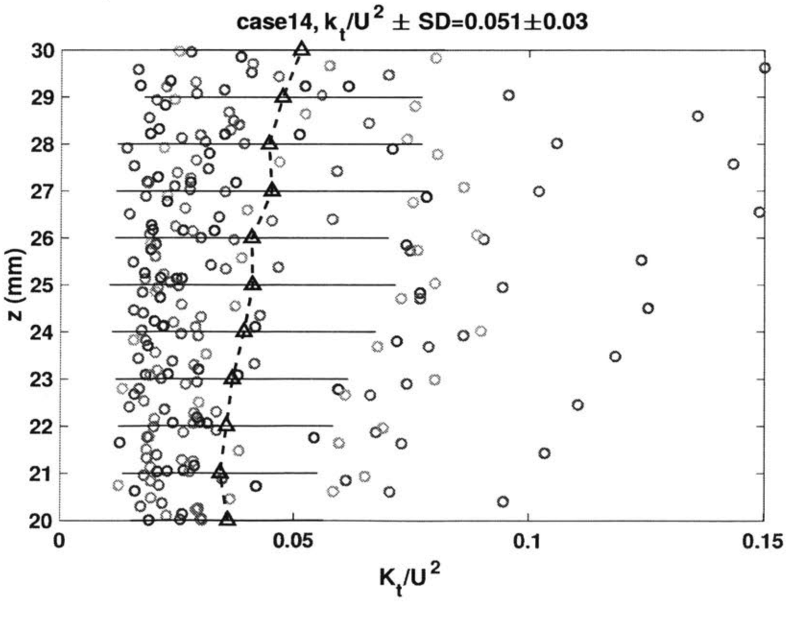

Figure D-16: Case 2.4, the Reynolds stress profile

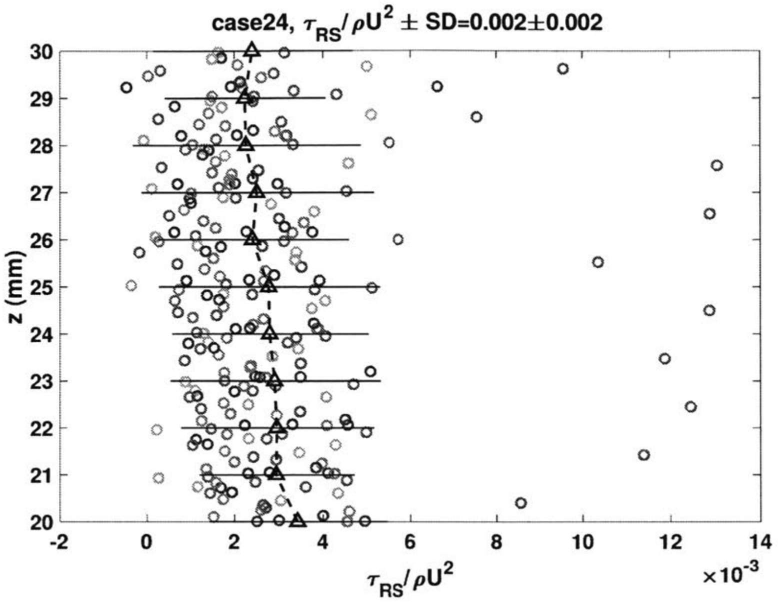

Figure D-17: Case 3.1, the turbulent kinetic energy profile

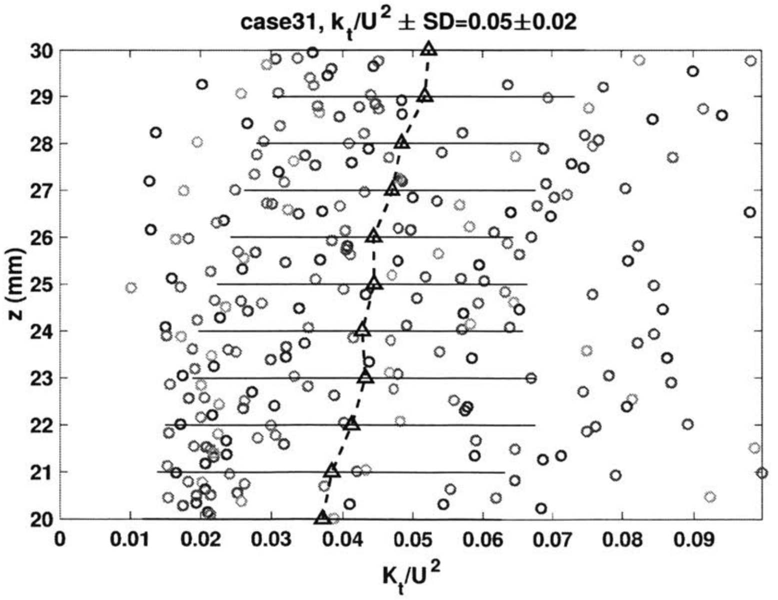

Figure D-18: Case 3.1, the Reynolds stress profile

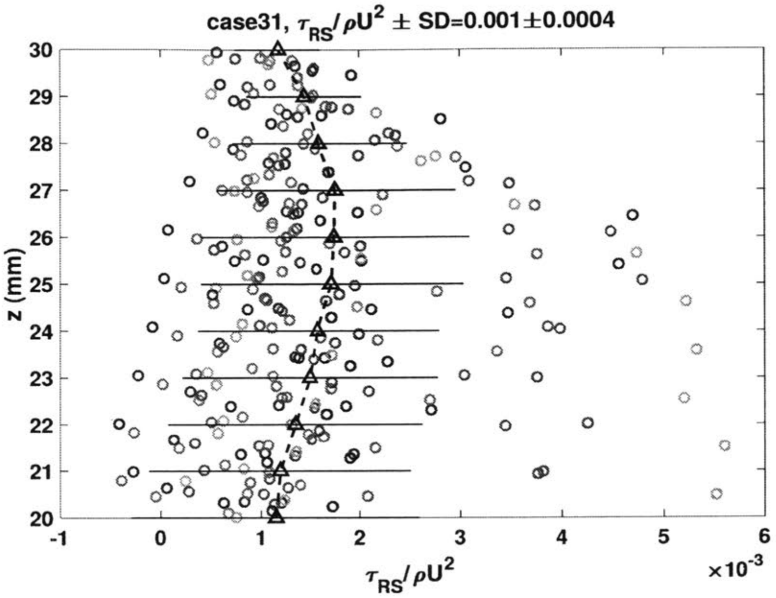

Figure D-19: Case 3.2, the turbulent kinetic energy profile

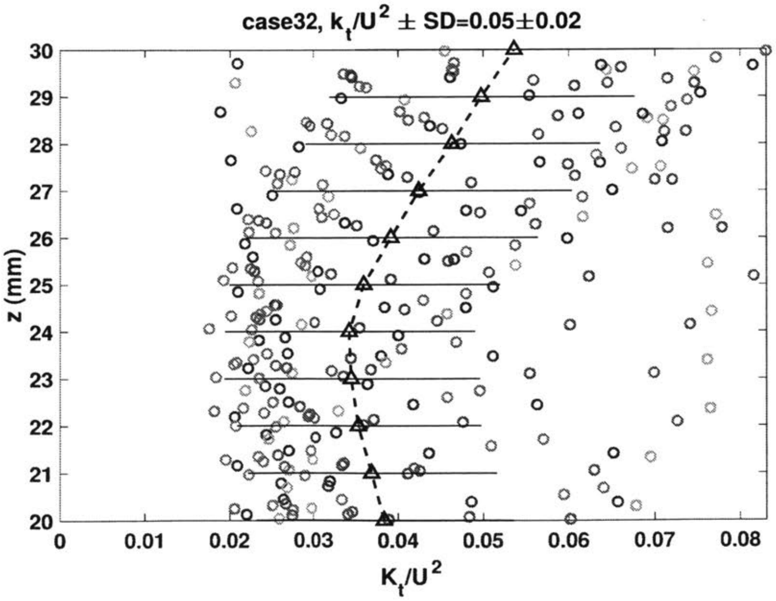

Figure D-20: Case 3.2, the Reynolds stress profile

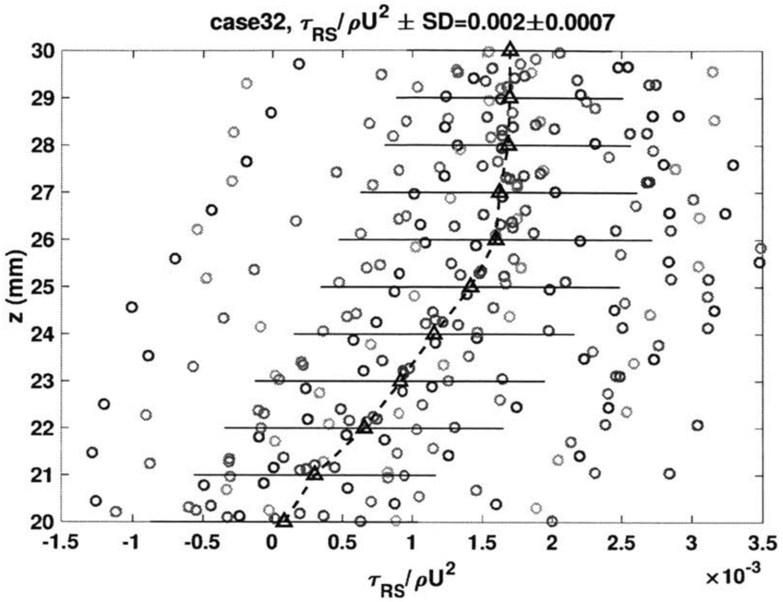

Figure D-21: Case 3.3, the turbulent kinetic energy profile

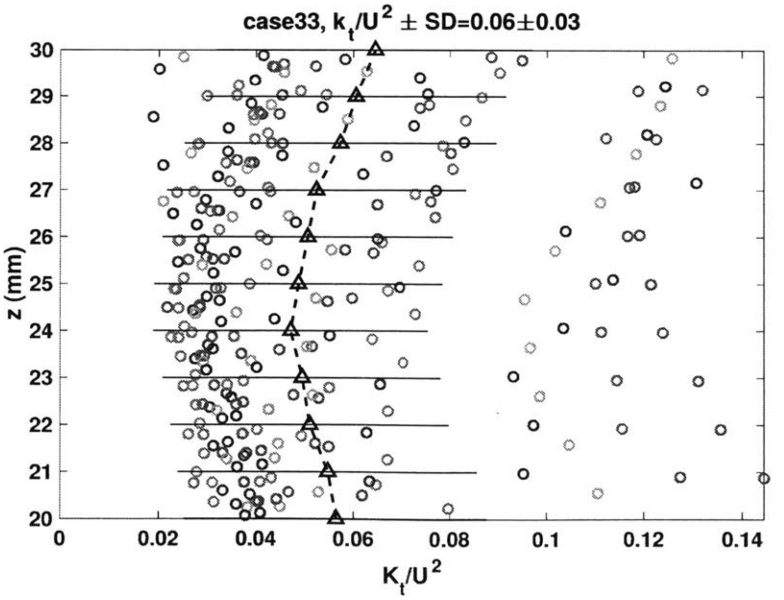

Figure D-22: Case 3.3, the Reynolds stress profile

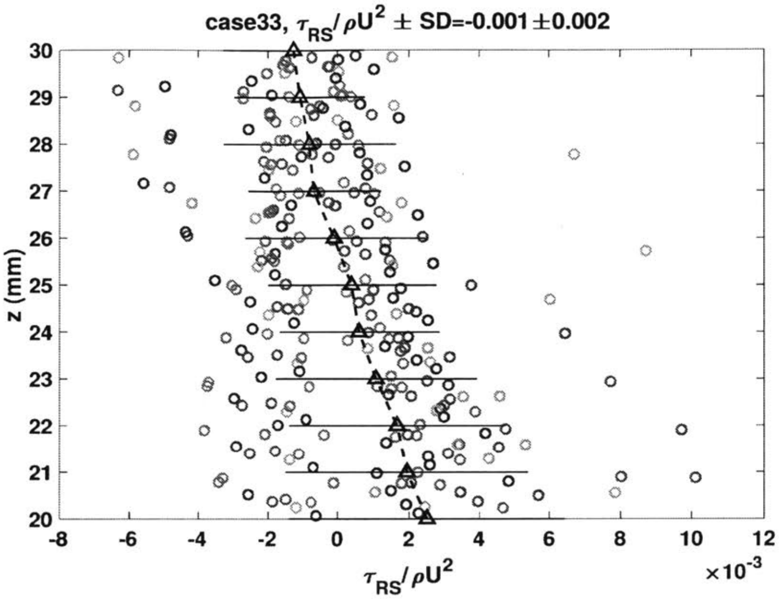

Figure D-23: Case 4.1, the turbulent kinetic energy profile

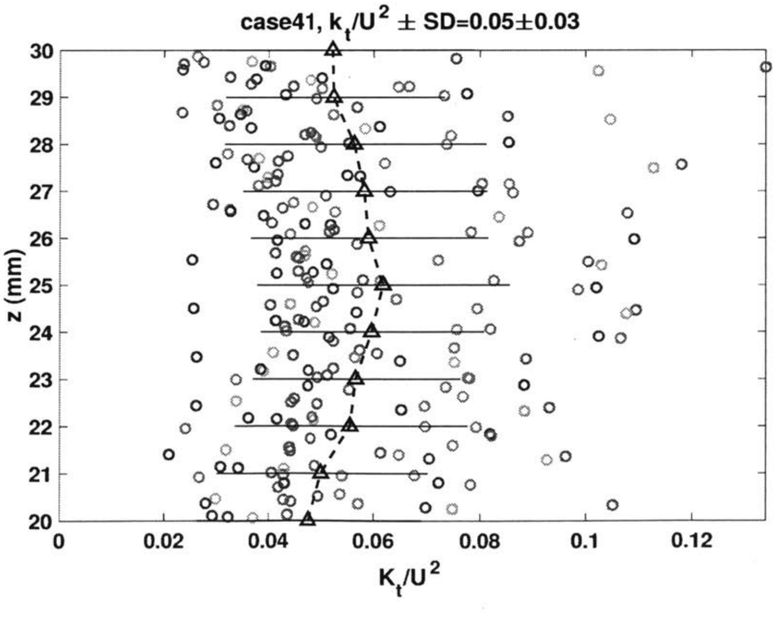

Figure D-24: Case 4.1, the Reynolds stress profile

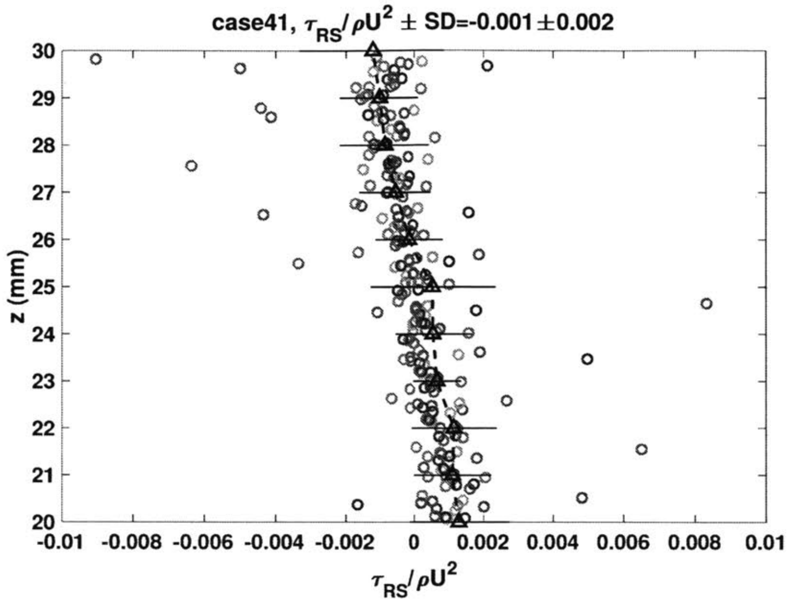

Figure D-25: Case 4.2, the turbulent kinetic energy profile

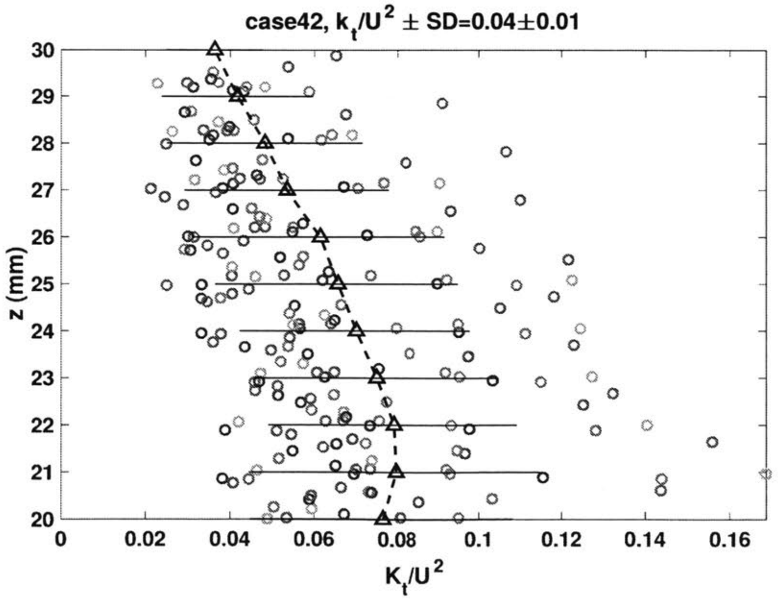

Figure D-26: Case 4.2, the Reynolds stress profile

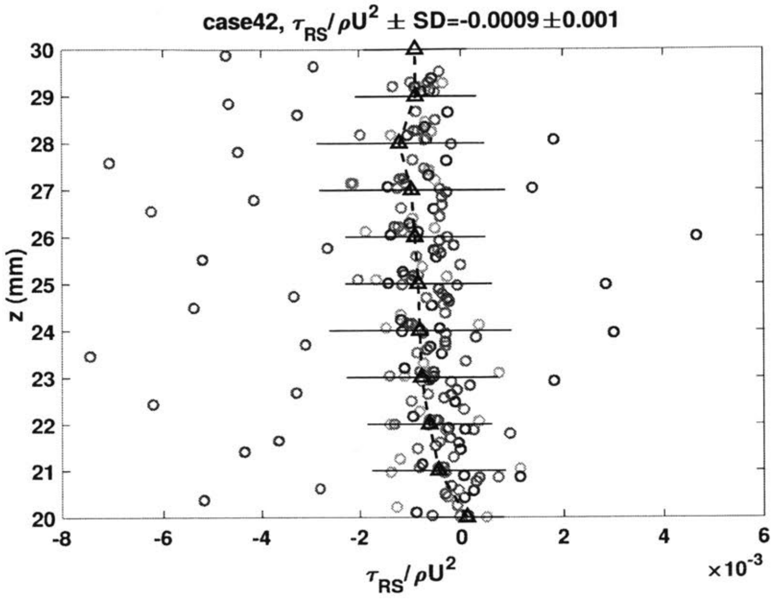

Figure D-27: Case 4.3, the turbulent kinetic energy profile

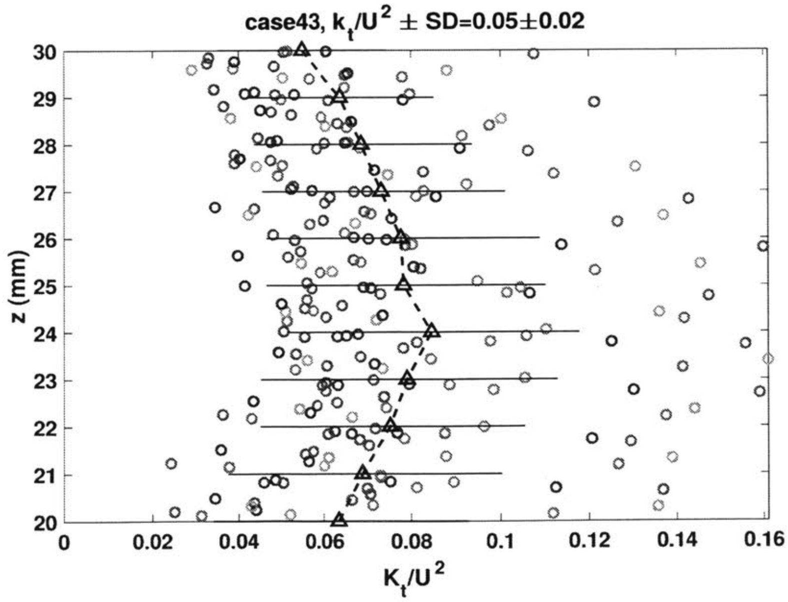

Figure D-28: Case 4.3, the Reynolds stress profile

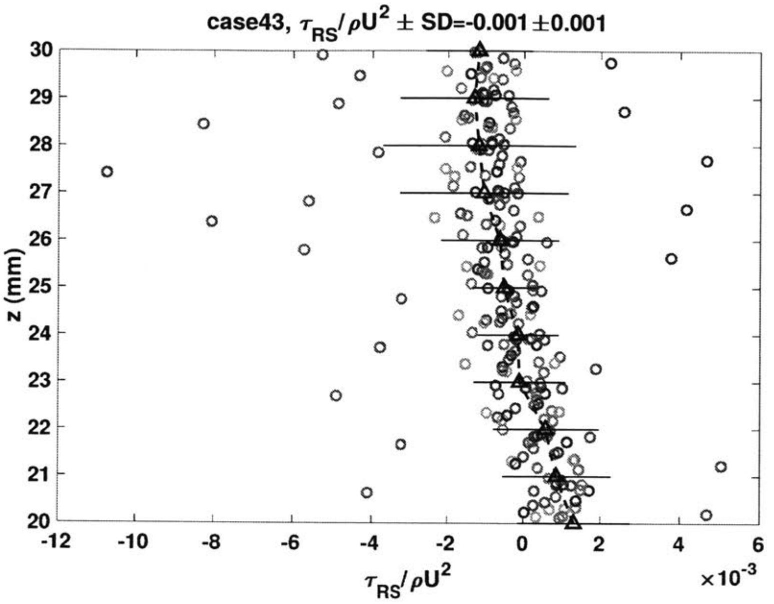

Figure D-29: Case 4.4, the turbulent kinetic energy profile

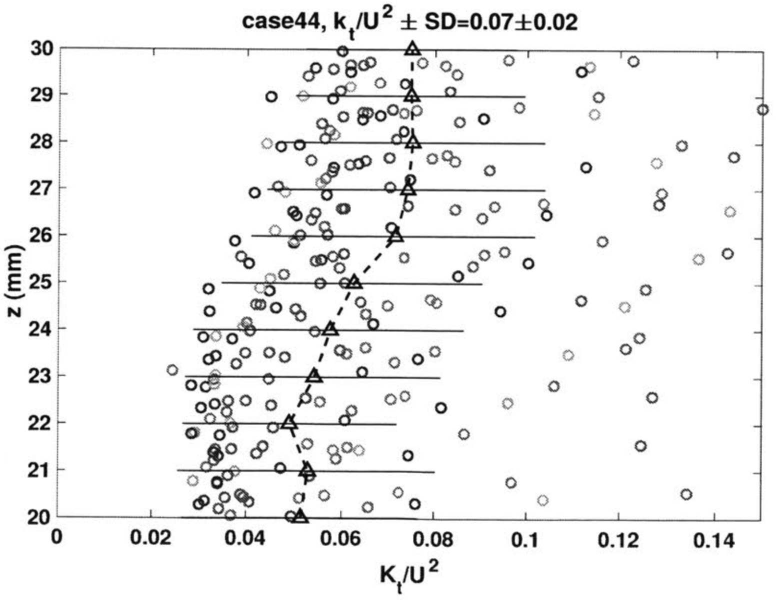

Figure D-30: Case 4.4, the Reynolds stress profile

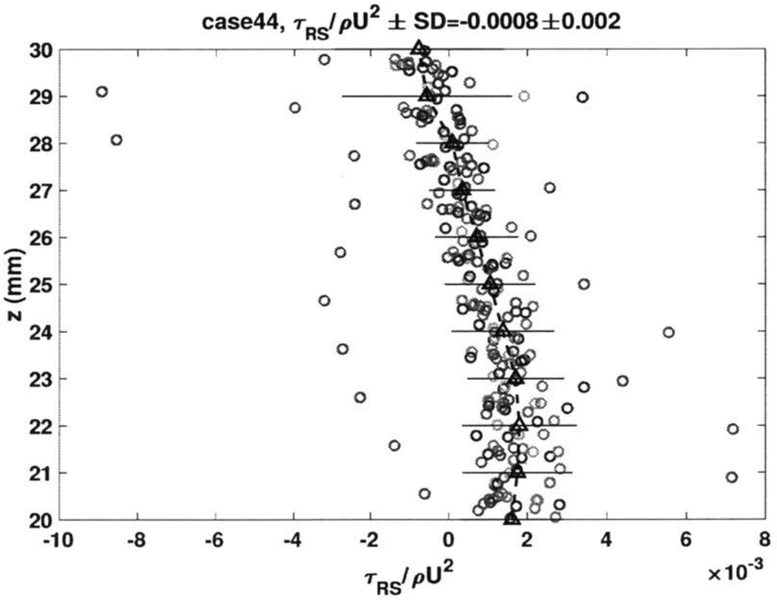

Appendix E

The bedform profiles

This section shows the measured ripple profiles in both temporal and spatial domain. The ripple wavelength, height, and period are tabulated in Chapter 4, Table 4.2, which is also copied below. For the plots of ripple profiles in temporal domain, the blue curves in figures (a) indicate the original measured bed topography profiles and the red curves are the same bed topography profiles filtered by 100-point movmean filter in MATLAB. The uncertainty in T, denoted as σ_T, was estimated as half the range of the first positive lobe (the black color part of the curves in Figures (b)). The $std(Z_{bed})$ in the title of the right figures represents the standard deviation of the bed elevation around the mean. For the plots of ripple profiles in spatial domain, in figures (b) the black lines show the identified ripple height and only ripple heights larger than 1mm (two times median grain size $d_s = 0.5mm$) were identified. The legends in figures (b) are $\eta_2 \pm SD(\eta_2)$, the means and the standard deviations of the identified ripple heights (the vertical black lines).

Table E.1: Copy of Table 4.2

Case number	$\lambda \pm \sigma_\lambda$ $[m]$	$\eta_1 \pm SD(\eta_1)$ (# of ripples) $[mm]$	$\eta_2 \pm SD(\eta_2)$ (# of ripples) $[mm]$	$T \pm \sigma_T$ $[s]$
Bare channels				
1.1	0.25 ± 0.03	5 ± 3 (5)	2 ± 1 (4)	880 ± 160
1.2	0.28 ± 0.05	11 ± 2 (9)	4 ± 3 (6)	660 ± 200
1.3	NA	11 ± 4 (16)	NA	38 ± 4
1.4	0.29 ± 0.09	13 ± 2 (7)	6 ± 5 (6)	40 ± 20
Channels with model emergent vegetation				
2.1	0.21 ± 0.06	3 ± 1 (3)	3 ± 1 (6)	2400 ± 300
2.2	0.16 ± 0.04	3 ± 1 (8)	3 ± 1 (7)	630 ± 160
2.3	0.17 ± 0.04	7 ± 3 (17)	7 ± 3 (4)	110 ± 50
2.4	0.17 ± 0.03	12 ± 5 (52)	10 ± 3 (6)	42 ± 11
3.1	0.10 ± 0.02	2 ± 1 (4)	3 ± 1 (8)	4600 ± 800
3.2	0.10 ± 0.02	4 ± 1 (2)	6 ± 2 (8)	2300 ± 500
3.3	0.16 ± 0.06	6 ± 2 (52)	6 ± 3 (5)	200 ± 110
4.1	NA	2 ± 1 (12)	NA	1800 ± 300
4.2	NA	2 ± 1 (7)	NA	1500 ± 500
4.3	NA	3 ± 1 (47)	NA	29 ± 12
4.4	NA	2 ± 1 (55)	NA	30 ± 20

Figure E-1: Case 1.1, the ripple profile in temporal domain

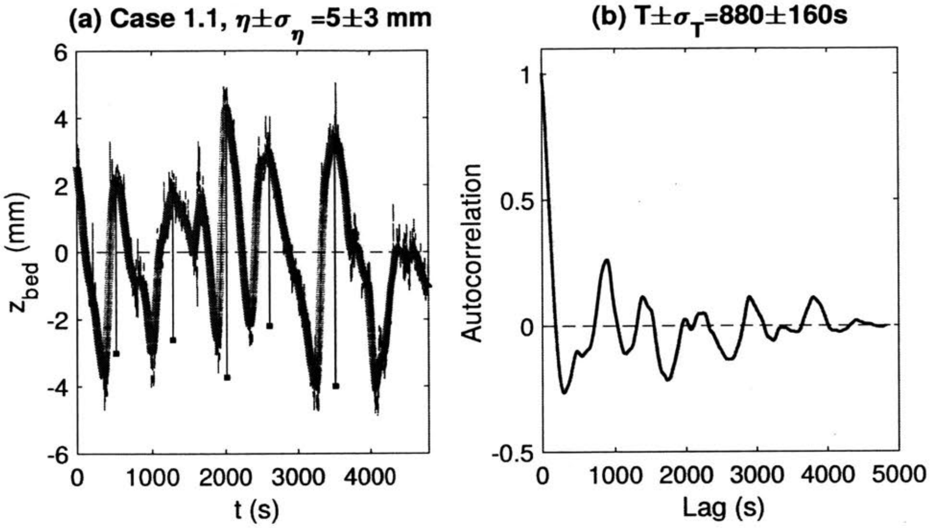

Figure E-2: Case 1.1, the ripple profile in spatial domain

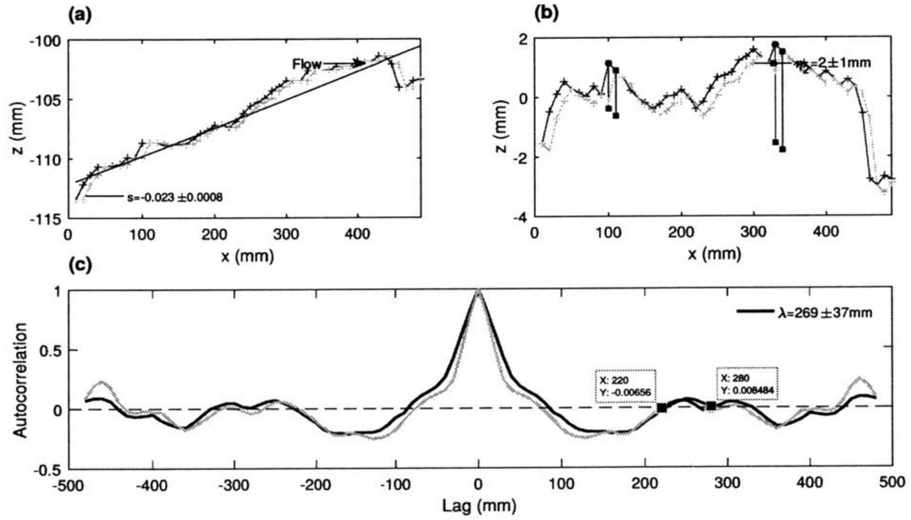

Figure E-3: Case 1.2, the ripple profile in temporal domain

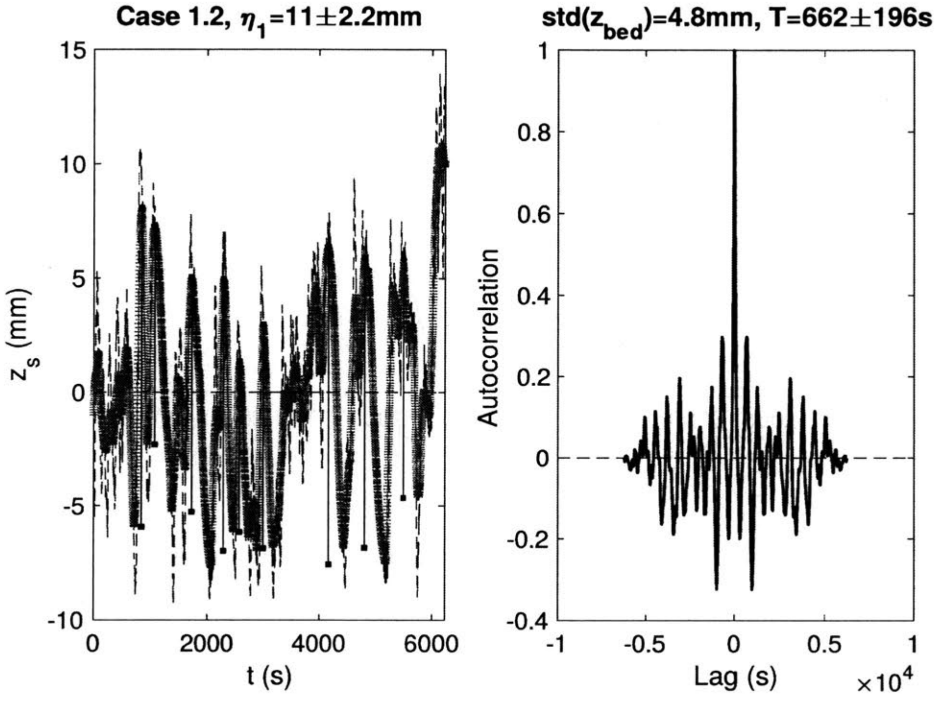

Figure E-4: Case 1.2, the ripple profile in spatial domain

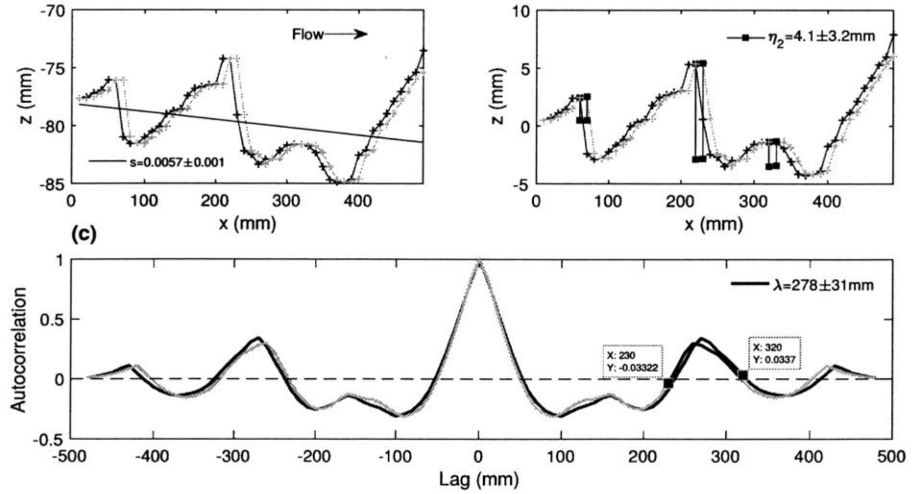

Figure E-5: Case 1.3, the ripple profile in temporal domain

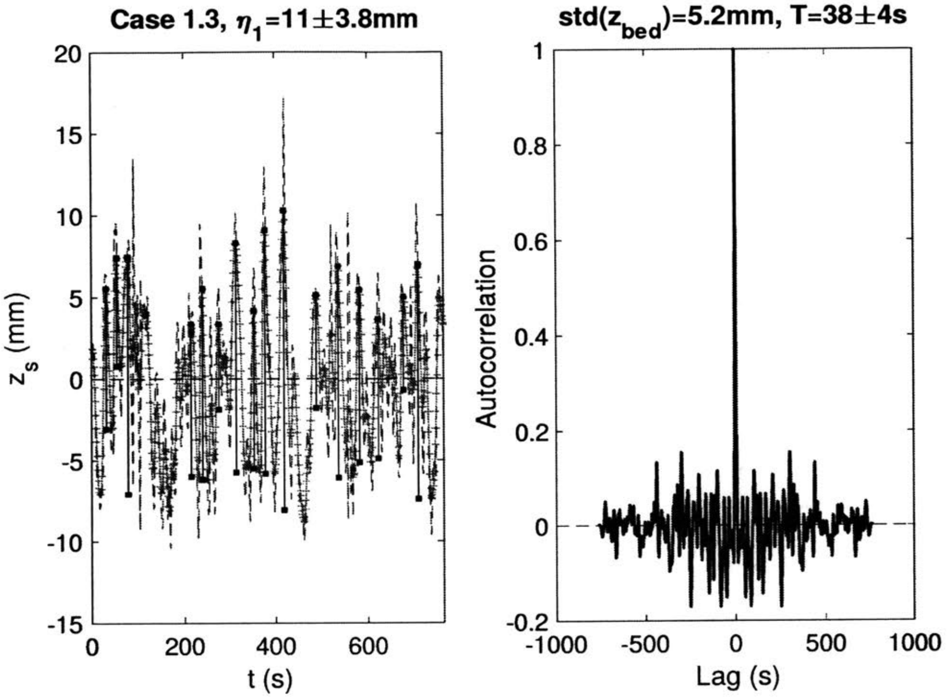

Figure E-6: Case 1.4, the ripple profile in temporal domain

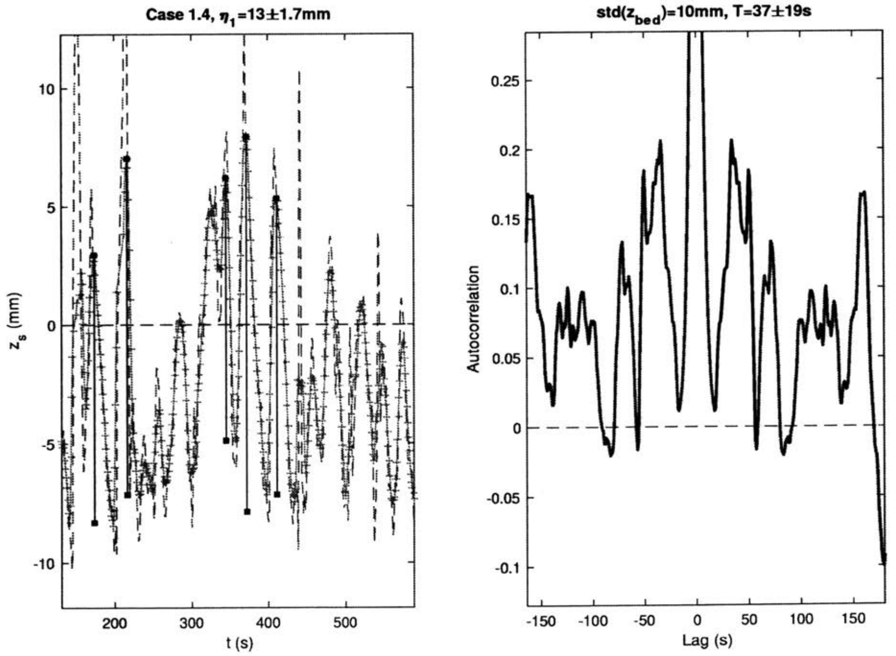

Figure E-7: Case 1.4, the ripple profile in spatial domain

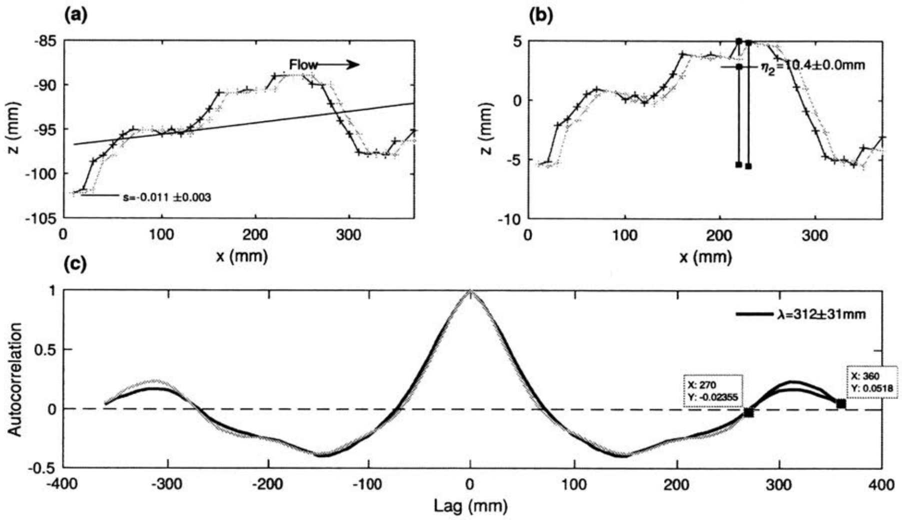

Case 1.4, the topography were measured twice at different times during the experiment. Here shows the two profiles measured at first time. The values of ripple height η_2 and ripple wavelength in the table in Chapter 4 were the average of all the identified ripples from both measurements.

Figure E-8: Case 1.4, the ripple profile in spatial domain (repeat)

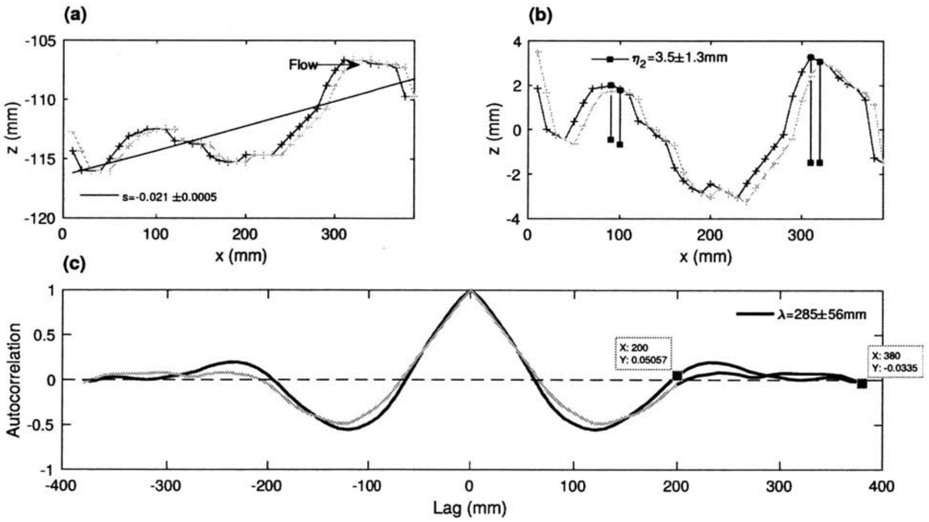

Case 1.4, the topography were measured twice at different times during the experiment. Here shows the two profiles measured at the second time.

Figure E-9: Case 2.1, the ripple profile in temporal domain

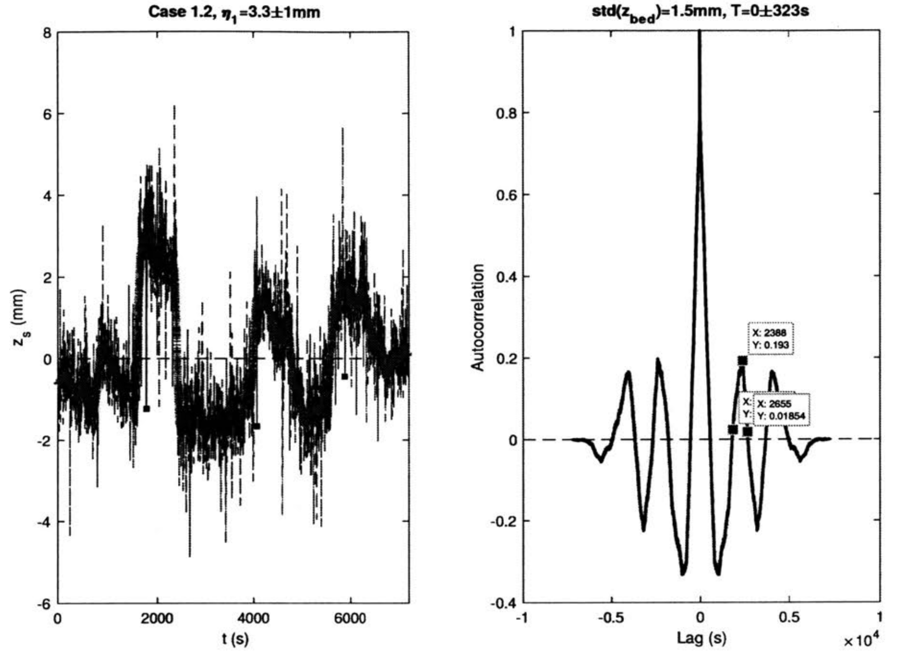

Figure E-10: Case 2.1, the ripple profile in spatial domain

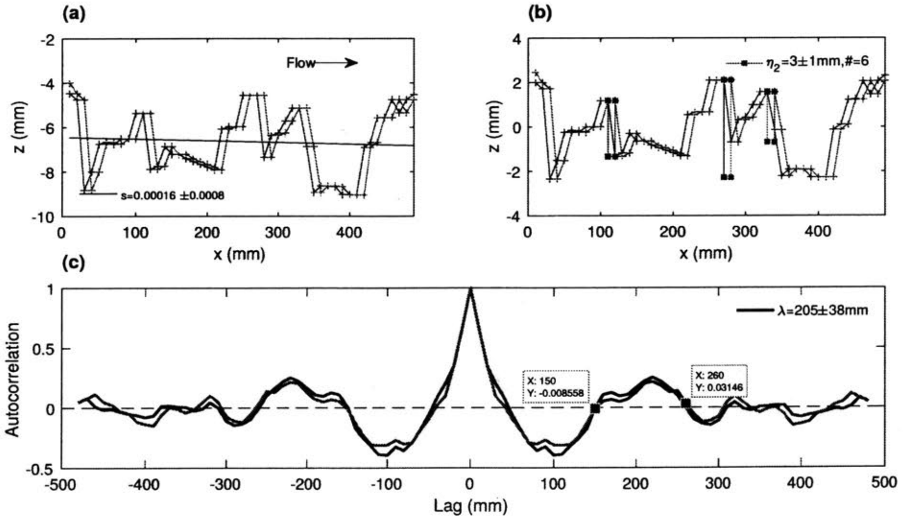

Figure E-11: Case 2.2, the ripple profile in temporal domain

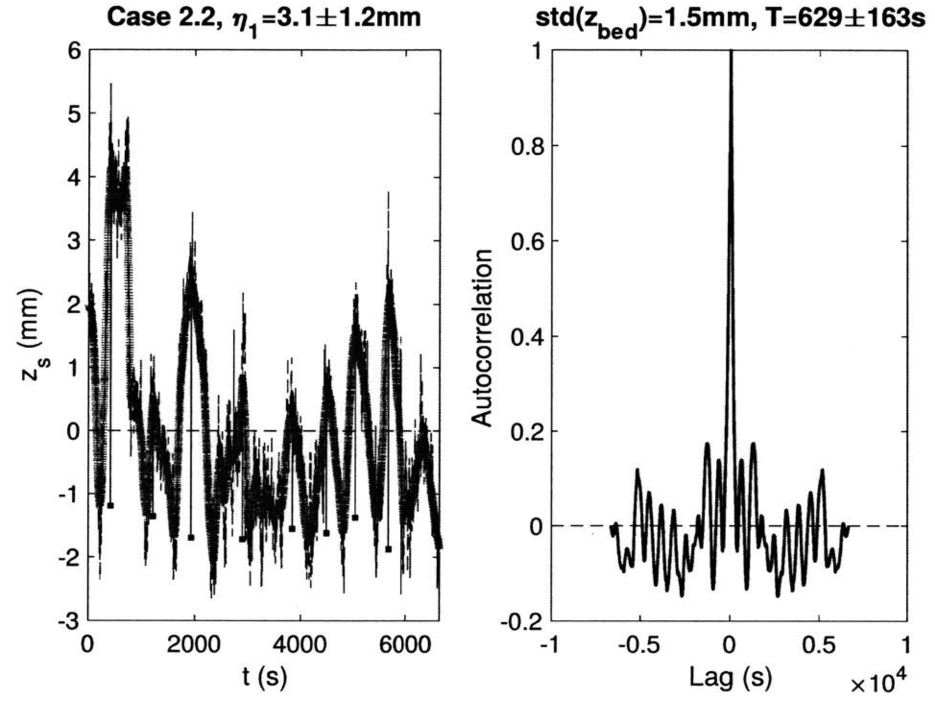

Figure E-12: Case 2.2, the ripple profile in spatial domain

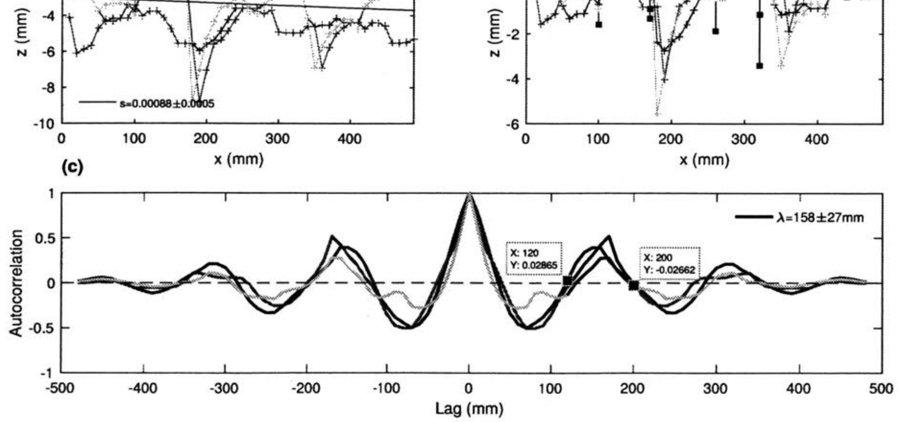

Figure E-13: Case 2.3, the ripple profile in temporal domain

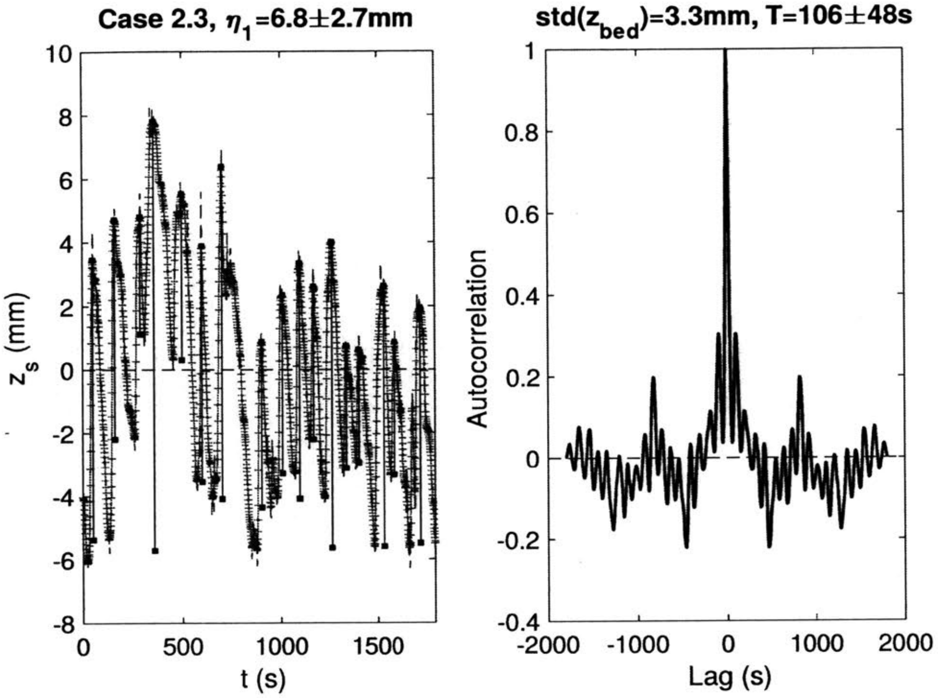

Figure E-14: Case 2.3, the ripple profile in spatial domain

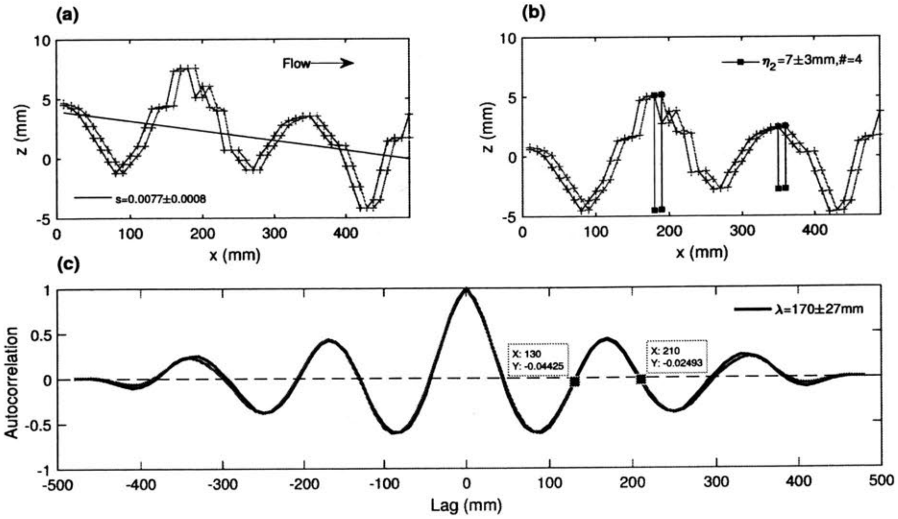

Figure E-15: Case 2.4, the ripple profile in temporal domain

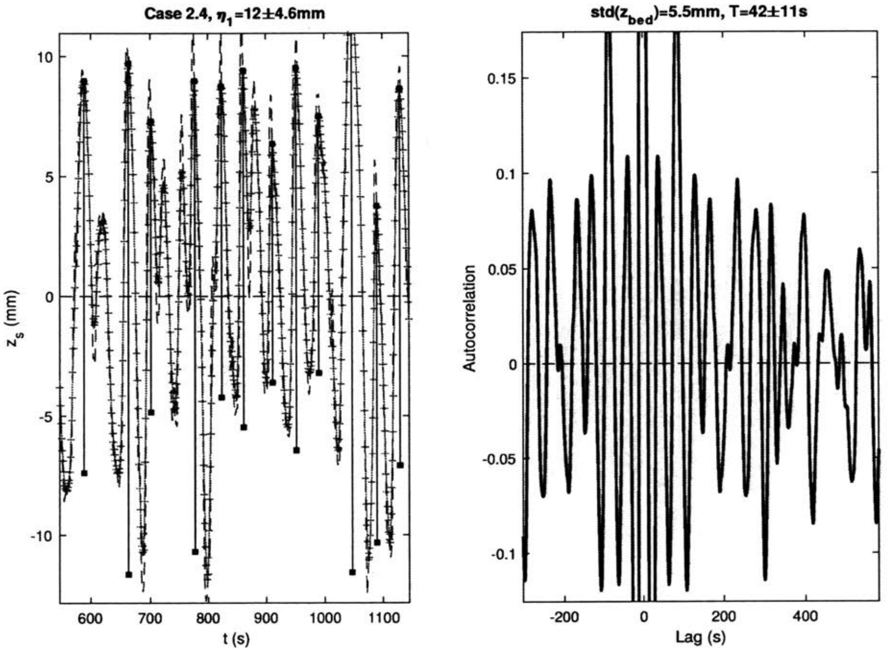

Only a portion of the identified ripple heights (black lines) was shown.

Figure E-16: Case 2.4, the ripple profile in spatial domain

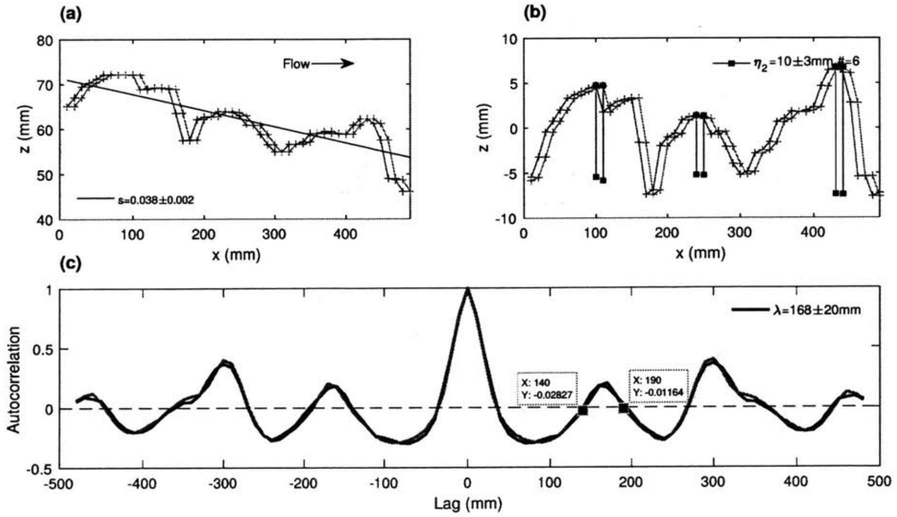

Figure E-17: Case 3.1, the ripple profile in temporal domain

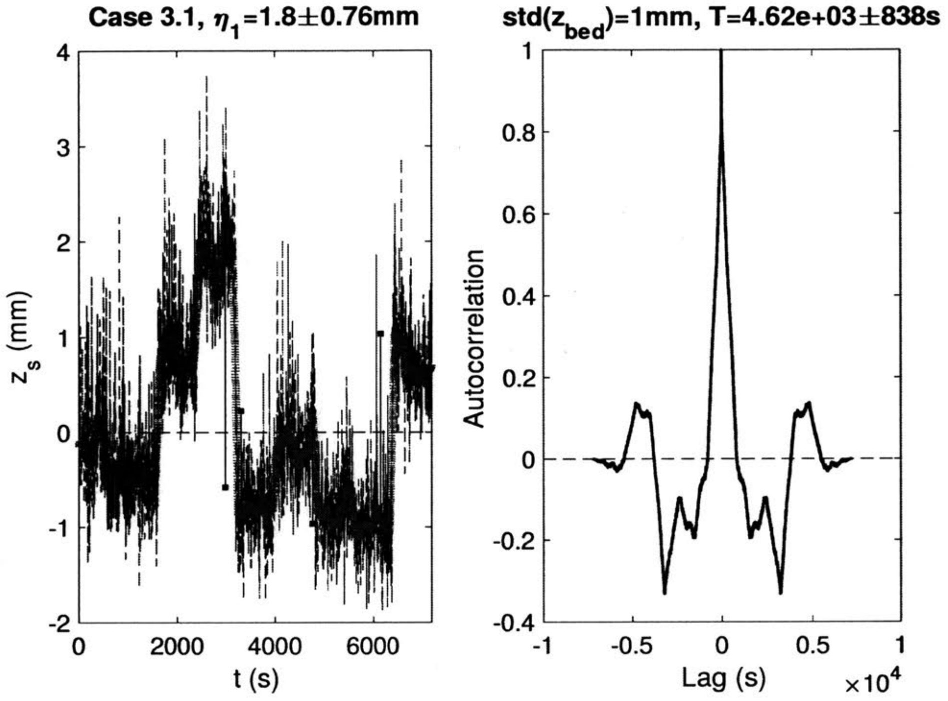

Figure E-18: Case 3.1, the ripple profile in spatial domain

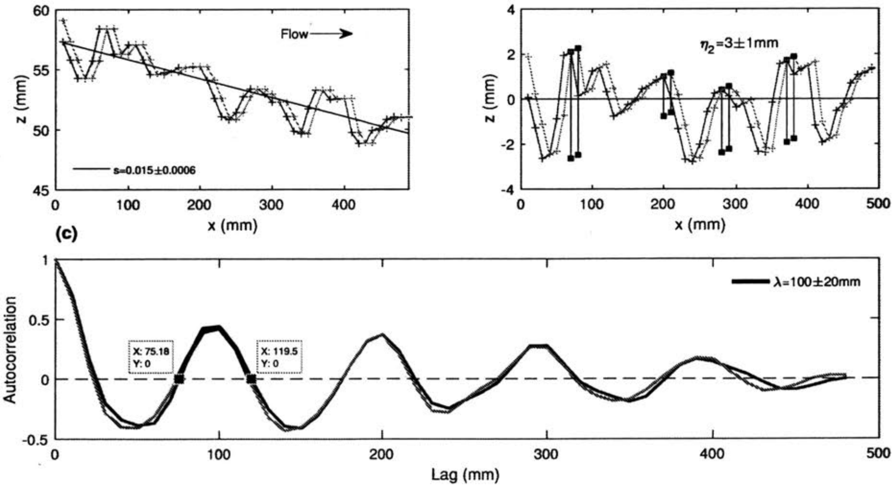

Figure E-19: Case 3.2, the ripple profile in temporal domain

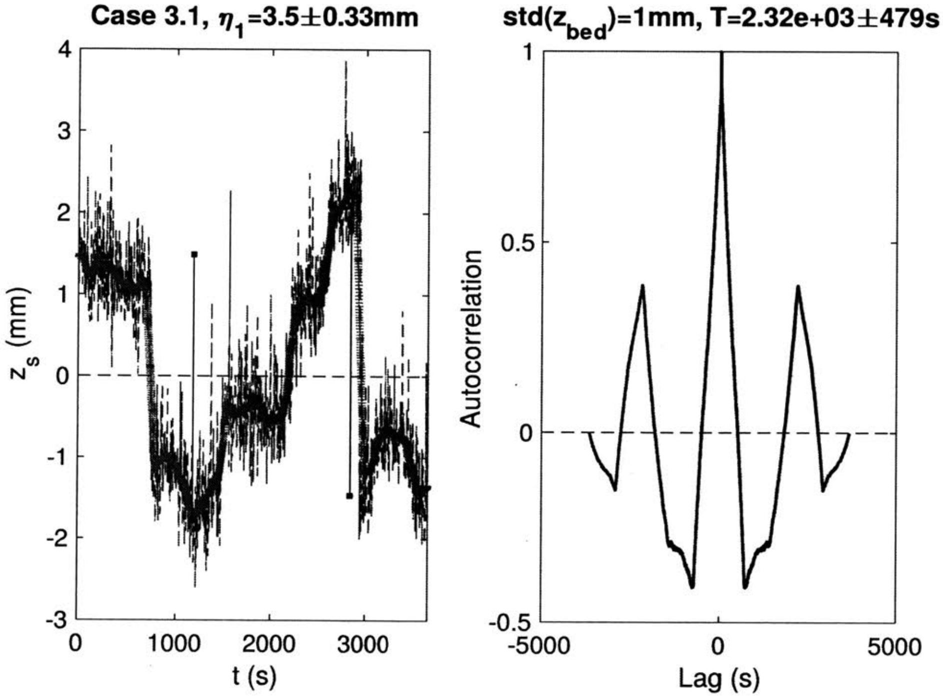

Figure E-20: Case 3.2, the ripple profile in spatial domain

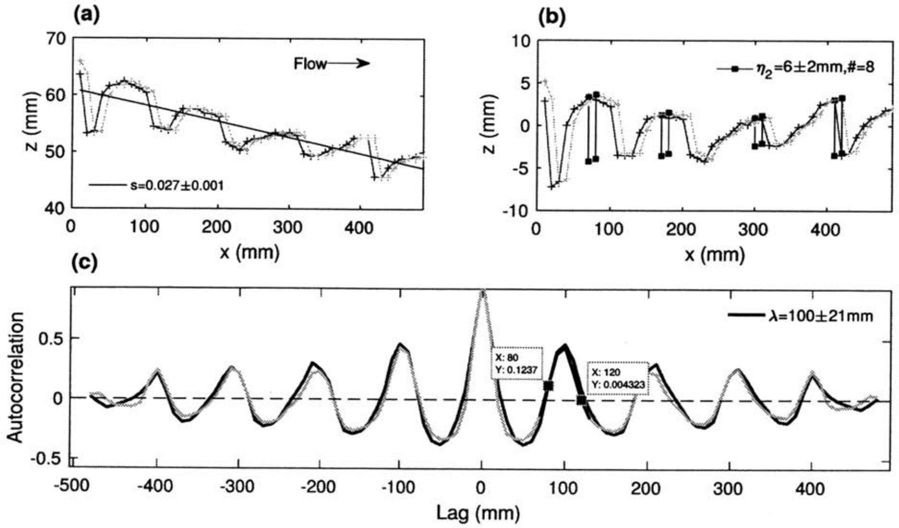

Figure E-21: Case 3.3, the ripple profile in temporal domain

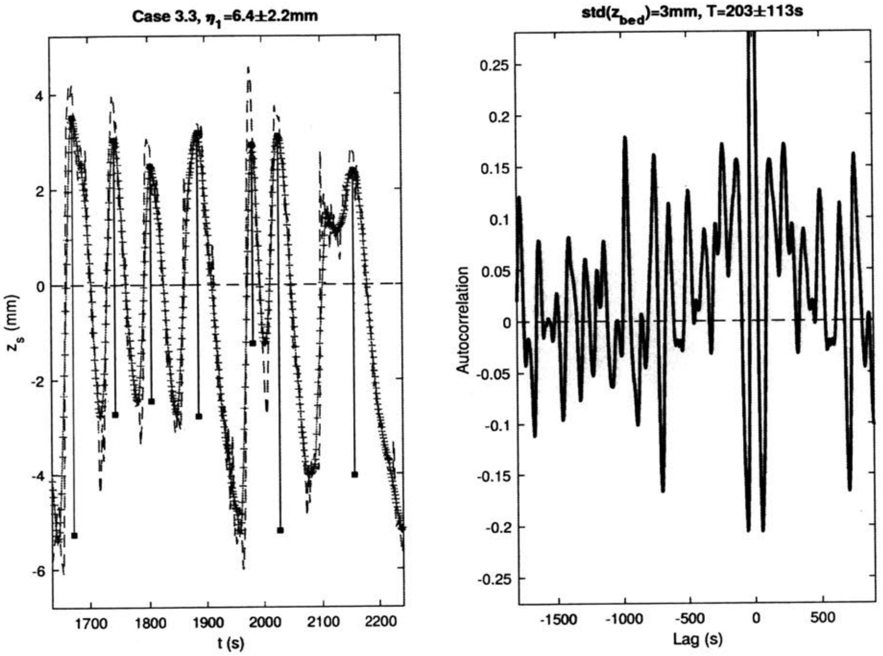

Only a portion of the identified ripple heights (black lines) was shown.

Figure E-22: Case 3.3, the ripple profile in spatial domain

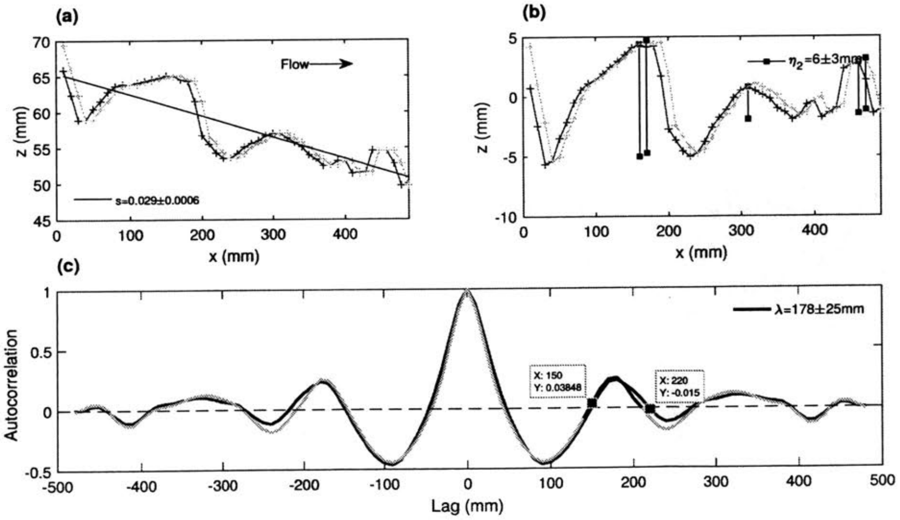

Figure E-23: Case 4.1, the ripple profile in temporal domain

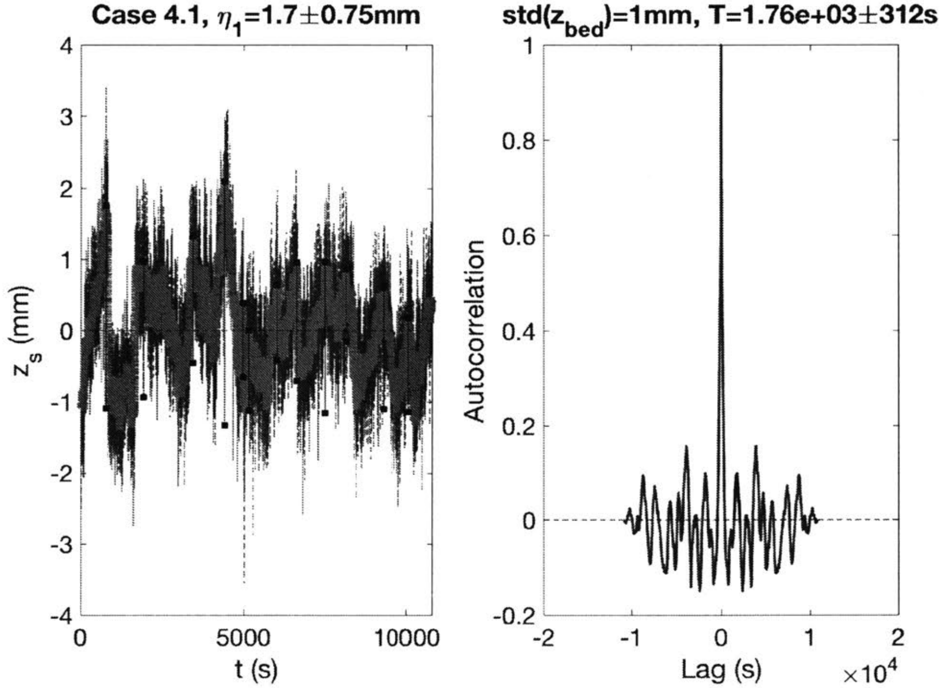

Figure E-24: Case 4.2, the ripple profile in temporal domain

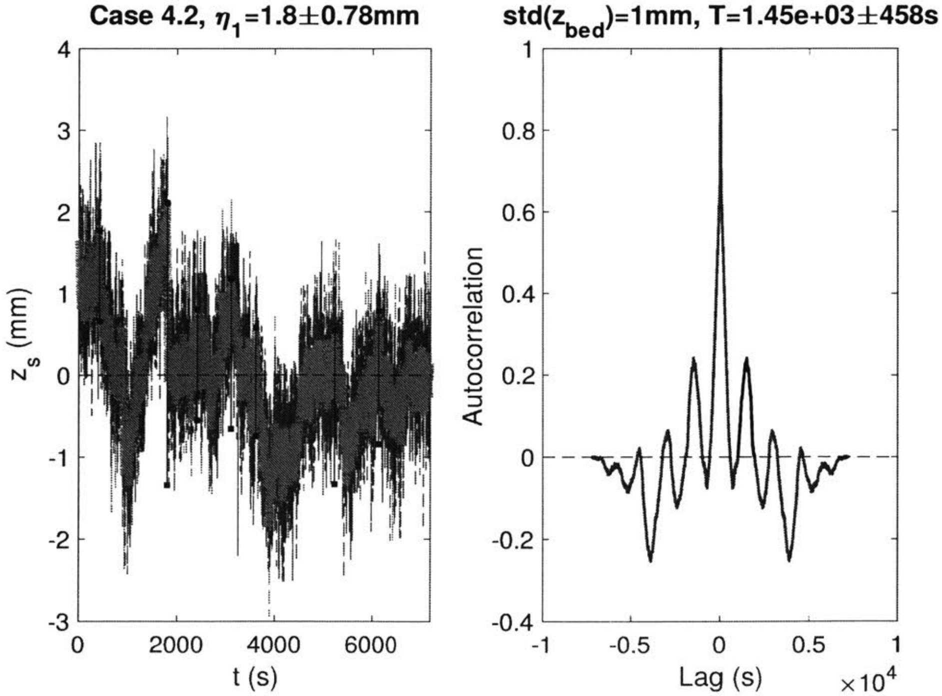

Figure E-25: Case 4.3, the ripple profile in temporal domain

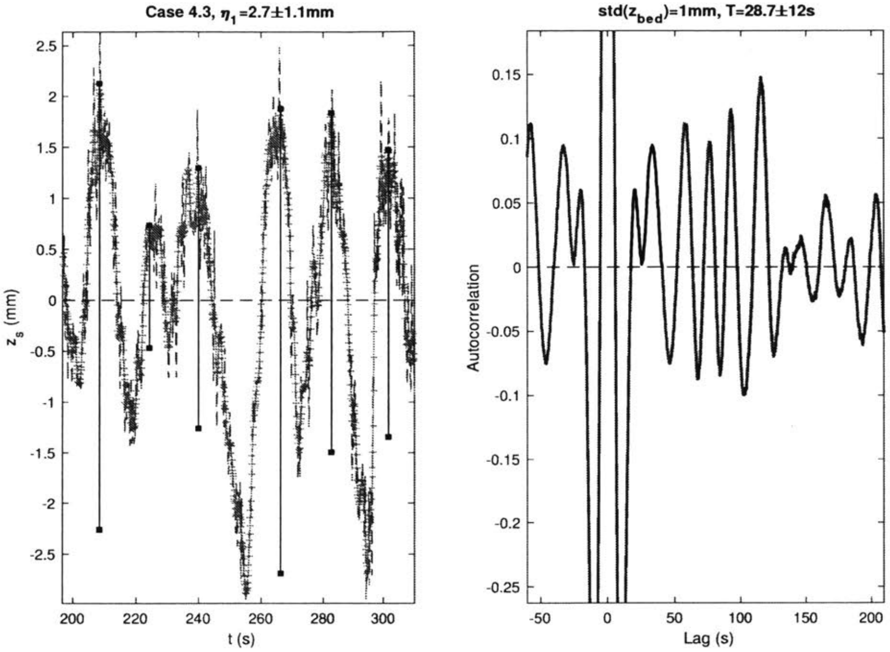

Only a portion of the identified ripple heights (black lines) was shown.

Figure E-26: Case 4.4, the ripple profile in temporal domain

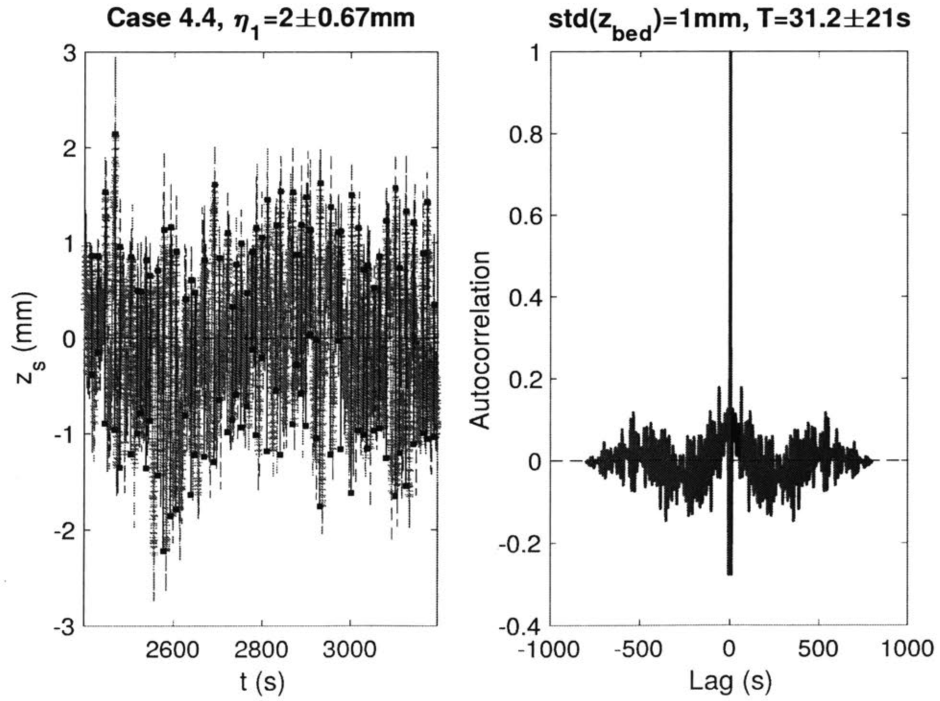

Bibliography

[1] Steven R Abt, Warren P Clary, and Christopher I Thornton. Sediment deposition and entrapment in vegetated streambeds. *Journal of Irrigation and Drainage Engineering*, 120(6):1098–1111, 1994.

[2] JD Ackerman and A Okubo. Reduced mixing in a marine macrophyte canopy. *Functional Ecology*, pages 305–309, 1993.

[3] Jaco H Baas. *Dimensional analysis of current ripples in recent and ancient depositional environments.* Faculteit Aardwetenschappen, 1993.

[4] Ralph Alger Bagnold. *The physics of blown sand and desert dunes.* Courier Corporation, 2012.

[5] Walter Berry, Norman Rubinstein, Brian Melzian, and Brian Hill. The biological effects of suspended and bedded sediment (sabs) in aquatic systems: a review. *United States Environmental Protection Agency, Duluth*, 2003.

[6] Pascale M Biron, Colleen Robson, Michel F Lapointe, and Susan J Gaskin. Comparing different methods of bed shear stress estimates in simple and complex flow fields. *Earth Surface Processes and Landforms*, 29(11):1403–1415, 2004.

[7] Michael D Blum and Harry H Roberts. Drowning of the mississippi delta due to insufficient sediment supply and global sea-level rise. *Nature Geoscience*, 2(7):488, 2009.

[8] Carl B Brown. Sediment transportation. *Engineering hydraulics*, 12:769–857, 1950.

[9] Thomas Buffin-Bélanger and André G Roy. 1 min in the life of a river: selecting the optimal record length for the measurement of turbulence in fluvial boundary layers. *Geomorphology*, 68(1):77–94, 2005.

[10] Ahmet O Celik, Panayiotis Diplas, Clinton L Dancey, and Manousos Valyrakis. Impulse and particle dislodgement under turbulent flow conditions. *Physics of Fluids*, 22(4):046601, 2010.

[11] Ahmet Ozan Celik, Panayiotis Diplas, and Clint L Dancey. Instantaneous turbulent forces and impulse on a rough bed: Implications for initiation of bed material movement. *Water Resources Research*, 49(4):2213–2227, 2013.

[12] YL Chang. Laboratory investigation of flume traction and transportation. *Transactions of the American Society of Civil Engineers*, 104(1):1246–1284, 1939.

[13] Nian-Sheng Cheng and Hoai Thanh Nguyen. Hydraulic radius for evaluating resistance induced by simulated emergent vegetation in open-channel flows. *Journal of hydraulic engineering*, 137(9):995–1004, 2011.

[14] Robert Costanza, Ralph d'Arge, Rudolf De Groot, S Faber, Monica Grasso, Bruce Hannon, Karin Limburg, Shahid Naeem, Robert V O'neill, Jose Paruelo, et al. The value of the world's ecosystem services and natural capital. 1997.

[15] JA Cotton, G Wharton, JAB Bass, CM Heppell, and RS Wotton. The effects of seasonal changes to in-stream vegetation cover on patterns of flow and accumulation of sediment. *Geomorphology*, 77(3-4):320–334, 2006.

[16] Maurice J Crickmore. Effect of flume width on bed-form characteristics. *Journal of the Hydraulics Division*, 1970.

[17] John C Crocker and David G Grier. Methods of digital video microscopy for colloidal studies. *Journal of colloid and interface science*, 179(1):298–310, 1996.

[18] Jesper Damgaard, Richard Soulsby, Andrew Peet, and Scott Wright. Sand transport on steeply sloping plane and rippled beds. *Journal of Hydraulic Engineering*, 129(9):706–719, 2003.

[19] Finn Danielsen, Mikael K Sørensen, Mette F Olwig, Vaithilingam Selvam, Faizal Parish, Neil D Burgess, Tetsuya Hiraishi, Vagarappa M Karunagaran, Michael S Rasmussen, Lars B Hansen, et al. The asian tsunami: a protective role for coastal vegetation. *Science(Washington)*, 310(5748):643, 2005.

[20] John W Day, Donald F Boesch, Ellis J Clairain, G Paul Kemp, Shirley B Laska, William J Mitsch, Kenneth Orth, Hassan Mashriqui, Denise J Reed, Leonard Shabman, et al. Restoration of the mississippi delta: lessons from hurricanes katrina and rita. *science*, 315(5819):1679–1684, 2007.

[21] Panayiotis Diplas, Clint L Dancey, Ahmet O Celik, Manousos Valyrakis, Krista Greer, and Tanju Akar. The role of impulse on the initiation of particle movement under turbulent flow conditions. *Science*, 322(5902):717–720, 2008.

[22] Andreas Dittrich. *Wechselwirkung Morphologie/Strömung naturnaher Fließgewässer*. Inst. f. Wasserwirtschaft u. Kulturtechnik, 1998.

[23] Ugyen Dorji and Reza Ghomashchi. Hydro turbine failure mechanisms: An overview. *Engineering Failure Analysis*, 44:136–147, 2014.

[24] MP DuBoys. Etudes du regime et l'action exercée par les eaux sur un lit a fond de graviers indefinement affouilable. *Annals des Ponts et Chaussées*, 5:141–195, 1879.

[25] Hans Albert Einstein. *Der Geschiebetrieb als Wahrscheinlichkeitsproblem.* PhD thesis, ETH Zurich, 1936.

[26] Hans Albert Einstein. *The bed-load function for sediment transportation in open channel flows.* Number 1026. US Department of Agriculture, 1950.

[27] Sergio Fagherazzi, Karin R Bryan, and William Nardin. Buried alive or washed away: The challenging life of mangroves in the mekong delta. *Oceanography*, 30(3):48–59, 2017.

[28] Sergio Fagherazzi, Giuilio Mariotti, Patricia L Wiberg, and KAREN J McGLATHERY. Marsh collapse does not require sea level rise. *Oceanography*, 26(3):70–77, 2013.

[29] Elizabeth M Follett and Heidi M Nepf. Sediment patterns near a model patch of reedy emergent vegetation. *Geomorphology*, 179:141–151, 2012.

[30] David Jon Furbish, Peter K Haff, John C Roseberry, and Mark W Schmeeckle. A probabilistic description of the bed load sediment flux: 1. theory. *Journal of Geophysical Research: Earth Surface*, 117(F3), 2012.

[31] Marco Ghisalberti and Heidi Nepf. The structure of the shear layer in flows over rigid and flexible canopies. *Environmental Fluid Mechanics*, 6(3):277–301, 2006.

[32] Grove Karl Gilbert and Edward Charles Murphy. *The transportation of debris by running water.* Number 86. US Government Printing Office, 1914.

[33] Basil Gomez and Michael Church. An assessment of bed load sediment transport formulae for gravel bed rivers. *Water Resources Research*, 25(6):1161–1186, 1989.

[34] Derek G Goring and Vladimir I Nikora. Despiking acoustic doppler velocimeter data. *Journal of Hydraulic Engineering*, 128(1):117–126, 2002.

[35] Raymond E Grizzle, Frederick T Short, Carter R Newell, Heidi Hoven, and Linda Kindblom. Hydrodynamically induced synchronous waving of seagrasses: 'monami' and its possible effects on larval mussel settlement. *Journal of Experimental Marine Biology and Ecology*, 206(1-2):165–177, 1996.

[36] Jason E. Hall, Damon M. Holzer, and Timothy J. Beechie. Predicting river floodplain and lateral channel migration for salmon habitat conservation. *Journal of the American Water Resources Association*, 43(3):786–797, 2007.

[37] AD Heathershaw and PD Thorne. Sea-bed noises reveal role of turbulent bursting phenomenon in sediment transport by tidal currents. *Nature*, 316:339–342, 1985.

[38] Bas Hofland and Jurjen A Battjes. Probability density function of instantaneous drag forces and shear stresses on a bed. *Journal of Hydraulic Engineering*, 132(11):1169–1175, 2006.

[39] Tang Hongwu, Hao Wang, DF Liang, SQ Lv, and L Yan. Incipient motion of sediment in the presence of emergent rigid vegetation. *Journal of Hydro-environment Research*, 7(3):202–208, 2013.

[40] Morgane Houssais, Carlos P Ortiz, Douglas J Durian, and Douglas J Jerolmack. Onset of sediment transport is a continuous transition driven by fluid shear and granular creep. *Nature communications*, 6, 2015.

[41] Blanco Humberto and Rattan Lal. Principles of soil conservation and management, 2012.

[42] David Hurther and U Lemmin. A correction method for turbulence measurements with a 3d acoustic doppler velocity profiler. *Journal of Atmospheric and Oceanic Technology*, 18(3):446–458, 2001.

[43] W Aaron Jenkins, Brian C Murray, Randall A Kramer, and Stephen P Faulkner. Valuing ecosystem services from wetlands restoration in the mississippi alluvial valley. *Ecological Economics*, 69(5):1051–1061, 2010.

[44] Angelina A Jordanova and CS James. Experimental study of bed load transport through emergent vegetation. *Journal of Hydraulic Engineering*, 129(6):474–478, 2003.

[45] Pierre Y Julien. *Erosion and sedimentation.* Cambridge University Press, 2010.

[46] Michael S Kearney, JC Riter, and R Eugene Turner. Freshwater river diversions for marsh restoration in louisiana: twenty-six years of changing vegetative cover and marsh area. *Geophysical Research Letters*, 38(16), 2011.

[47] John M Kondziolka and Heidi M Nepf. Vegetation wakes and wake interaction shaping aquatic landscape evolution. *Limnology and Oceanography: Fluids and Environments*, 4(1):106–119, 2014.

[48] Umesh C Kothyari, Haruyuki Hashimoto, and Kenjirou Hayashi. Effect of tall vegetation on sediment transport by channel flows. *Journal of Hydraulic Research*, 47(6):700–710, 2009.

[49] Umesh C Kothyari, Kenjirou Hayashi, and Haruyuki Hashimoto. Drag coefficient of unsubmerged rigid vegetation stems in open channel flows. *Journal of Hydraulic Research*, 47(6):691–699, 2009.

[50] Claire Kremen. Managing ecosystem services: what do we need to know about their ecology? *Ecology letters*, 8(5):468–479, 2005.

[51] RA Kuhnle, JK Horton, SJ Bennett, and JL Best. Bed forms in bimodal sand–gravel sediments: laboratory and field analysis. *Sedimentology*, 53(3):631–654, 2006.

[52] PK Kundu, IM Cohen, and HH Hu. Fluid mechanics. 2004. *Elsevier Academic Press, San Diego). Two-and three-dimensional self-sustained flow oscillations*, 307:471–476, 2008.

[53] Eric Lajeunesse, Luce Malverti, and François Charru. Bed load transport in turbulent flow at the grain scale: Experiments and modeling. *Journal of Geophysical Research: Earth Surface*, 115(F4), 2010.

[54] Rattan Lal. Soil carbon sequestration impacts on global climate change and food security. *science*, 304(5677):1623–1627, 2004.

[55] Caroline Le Bouteiller and JG Venditti. Sediment transport and shear stress partitioning in a vegetated flow. *Water Resources Research*, 51(4):2901–2922, 2015.

[56] Chao Liu and Heidi Nepf. Sediment deposition within and around a finite patch of model vegetation over a range of channel velocity. *Water Resources Research*, 52(1):600–612, 2016.

[57] Mitul Luhar, Jeffrey Rominger, and Heidi Nepf. Interaction between flow, transport and vegetation spatial structure. *Environmental Fluid Mechanics*, 8(5-6):423, 2008.

[58] Rebecca B Manners, Andrew C Wilcox, Li Kui, Anne F Lightbody, John C Stella, and Leonard S Sklar. When do plants modify fluvial processes? plant-hydraulic interactions under variable flow and sediment supply rates. *Journal of Geophysical Research: Earth Surface*, 120(2):325–345, 2015.

[59] M Marani, A d'Alpaos, S Lanzoni, and M Santalucia. Understanding and predicting wave erosion of marsh edges. *Geophysical Research Letters*, 38(21), 2011.

[60] Rajat Mazumder. Turbulence–particle interactions and their implications for sediment transport and bedform mechanics under unidirectional current: some recent developments. *Earth-Science Reviews*, 50(1-2):113–124, 2000.

[61] Elizabeth Mcleod, Gail L Chmura, Steven Bouillon, Rodney Salm, Mats Björk, Carlos M Duarte, Catherine E Lovelock, William H Schlesinger, and Brian R Silliman. A blueprint for blue carbon: toward an improved understanding of the role of vegetated coastal habitats in sequestering co2. *Frontiers in Ecology and the Environment*, 9(10):552–560, 2011.

[62] Dieter WSA Meire, John M Kondziolka, and Heidi M Nepf. Interaction between neighboring vegetation patches: Impact on flow and deposition. *Water Resources Research*, 50(5):3809–3825, 2014.

[63] E Meyer-Peter, H Favre, and HA Einstein. Neuere versuchsresultate über den geschiebetrieb. *Schweizerische Bauzeitung*, 103(13):147–150, 1934.

[64] Eugen Meyer-Peter and R Müller. Formulas for bed-load transport. In *IAHSR 2nd meeting, Stockholm, appendix 2*. IAHR, 1948.

[65] ER Micheli and JW Kirchner. Effects of wet meadow riparian vegetation on streambank erosion. 2. measurements of vegetated bank strength and consequences for failure mechanics. *Earth Surface Processes and Landforms*, 27(7):687–697, 2002.

[66] Joann Mossa and Harry H Roberts. Synergism of riverine and winter storm-related sediment transport processes in louisiana's coastal wetlands. 1990.

[67] Pamela Naden, Ponnambalam Rameshwaran, Owen Mountford, and Coralie Robertson. The influence of macrophyte growth, typical of eutrophic conditions, on river flow velocities and turbulence production. *Hydrological Processes: An International Journal*, 20(18):3915–3938, 2006.

[68] Siddharth Narayan, Michael W Beck, Paul Wilson, Christopher J Thomas, Alexandra Guerrero, Christine C Shepard, Borja G Reguero, Guillermo Franco, Jane Carter Ingram, and Dania Trespalacios. The value of coastal wetlands for flood damage reduction in the northeastern usa. *Scientific reports*, 7(1):9463, 2017.

[69] Jonathan M Nelson, Ronald L Shreve, Stephen R McLean, and Thomas G Drake. Role of near-bed turbulence structure in bed load transport and bed form mechanics. *Water Resources Research*, 31(8):2071–2086, 1995.

[70] Heidi M Nepf. Flow and transport in regions with aquatic vegetation. *Annual Review of Fluid Mechanics*, 44:123–142, 2012.

[71] Heidi M Nepf. Hydrodynamics of vegetated channels. *Journal of Hydraulic Research*, 50(3):262–279, 2012.

[72] HM Nepf. Drag, turbulence, and diffusion in flow through emergent vegetation. *Water resources research*, 35(2):479–489, 1999.

[73] Iehisa Nezu, Hiroji Nakagawa, and Gerhard H Jirka. Turbulence in open-channel flows. *Journal of Hydraulic Engineering*, 120(10):1235–1237, 1994.

[74] Iehisa Nezu and Wolfgang Rodi. Open-channel flow measurements with a laser doppler anemometer. *Journal of Hydraulic Engineering*, 112(5):335–355, 1986.

[75] Y Nino and MH Garcia. Experiments on particle-turbulence interactions in the near–wall region of an open channel flow: implications for sediment transport. *Journal of Fluid Mechanics*, 326:285–319, 1996.

[76] Chris Paola, Robert R Twilley, Douglas A Edmonds, Wonsuck Kim, David Mohrig, Gary Parker, Enrica Viparelli, and Vaughan R Voller. Natural processes in delta restoration: Application to the mississippi delta. *Annual Review of Marine Science*, 3:67–91, 2011.

[77] Eliana Perucca, Carlo Camporeale, and Luca Ridolfi. Significance of the riparian vegetation dynamics on meandering river morphodynamics. *Water Resources Research*, 43(3), 2007.

[78] WJR Poos. Stability diagram of upper flow regime bedforms. an experimental study. Master's thesis, 2011.

[79] ND Pope, John Widdows, and MD Brinsley. Estimation of bed shear stress using the turbulent kinetic energy approach - a comparison of annular flume and field data. *Continental Shelf Research*, 26(8):959–970, 2006.

[80] Ana M Ricardo, Katinka Koll, Mário J Franca, Anton J Schleiss, and Rui ML Ferreira. The terms of turbulent kinetic energy budget within random arrays of emergent cylinders. *Water Resources Research*, 50(5):4131–4148, 2014.

[81] Jeffrey T Rominger, Anne F Lightbody, and Heidi M Nepf. Effects of added vegetation on sand bar stability and stream hydrodynamics. *Journal of Hydraulic Engineering*, 136(12):994–1002, 2010.

[82] John C Roseberry, Mark W Schmeeckle, and David Jon Furbish. A probabilistic description of the bed load sediment flux: 2. particle activity and motions. *Journal of Geophysical Research: Earth Surface*, 117(F3), 2012.

[83] William Walden Rubey. Settling velocity of gravel, sand, and silt particles. *American Journal of Science*, (148):325–338, 1933.

[84] Sarik Salim, Charitha Pattiaratchi, Rafael Tinoco, Giovanni Coco, Yasha Hetzel, Sarath Wijeratne, and Ravindra Jayaratne. The influence of turbulent bursting on sediment resuspension under unidirectional currents. *Earth Surface Dynamics*, 5(3):399, 2017.

[85] Mark W Schmeeckle. The role of velocity, pressure, and bed stress fluctuations in bed load transport over bed forms: numerical simulation downstream of a backward-facing step. *Earth Surface Dynamics Discussions*, 2(2):715–732, 2014.

[86] Albert Shields. Anwendung der aehnlichkeitsmechanik und der turbulenzforschung auf die geschiebebewegung. *PhD Thesis Technical University Berlin*, 1936.

[87] Albert Shields. Application of similarity principles and turbulence research to bed-load movement. Technical report, Soil Conservation Service, 1936.

[88] GM Smart and HM Habersack. Pressure fluctuations and gravel entrainment in rivers. *Journal of Hydraulic Research*, 45(5):661–673, 2007.

[89] RL Soulsby, RJS Whitehouse, and KV Marten. Prediction of time-evolving sand ripples in shelf seas. *Continental Shelf Research*, 38:47–62, 2012.

[90] John B Southard. Experimental determination of bed-form stability. *Annual Review of Earth and Planetary Sciences*, 19(1):423–455, 1991.

[91] KR Stapleton and DA Huntley. Seabed stress determinations using the inertial dissipation method and the turbulent kinetic energy method. *Earth Surface Processes and Landforms*, 20(9):807–815, 1995.

[92] Richard W Sternberg. Measurements of sediment movement and ripple migration in a shallow marine environment. *Marine Geology*, 5(3):195–205, 1967.

[93] Thorsten Stoesser, SJ Kim, and P Diplas. Turbulent flow through idealized emergent vegetation. *Journal of hydraulic engineering*, 136(12):1003–1017, 2010.

[94] B Mutlu Sumer, Lloyd HC Chua, N-S Cheng, and Jørgen Fredsøe. Influence of turbulence on bed load sediment transport. *Journal of Hydraulic Engineering*, 129(8):585–596, 2003.

[95] B Mutlu Sumer and Beyhan Oguz. Particle motions near the bottom in turbulent flow in an open channel. *Journal of Fluid Mechanics*, 86(1):109–127, 1978.

[96] James PM Syvitski, Albert J Kettner, Irina Overeem, Eric WH Hutton, Mark T Hannon, G Robert Brakenridge, John Day, Charles Vörösmarty, Yoshiki Saito, Liviu Giosan, et al. Sinking deltas due to human activities. *Nature Geoscience*, 2(10):681, 2009.

[97] Y Tanino and HM Nepf. Experimental investigation of lateral dispersion in aquatic canopies. In *PROCEEDINGS OF THE CONGRESS-INTERNATIONAL ASSOCIATION FOR HYDRAULIC RESEARCH*, volume 32, page 152, 2007.

[98] Yukie Tanino and Heidi M Nepf. Laboratory investigation of mean drag in a random array of rigid, emergent cylinders. *Journal of Hydraulic Engineering*, 134(1):34–41, 2008.

[99] Yukie Tanino and Heidi M Nepf. Lateral dispersion in random cylinder arrays at high reynolds number. *Journal of Fluid Mechanics*, 600:339–371, 2008.

[100] John Taylor. *Introduction to error analysis, the study of uncertainties in physical measurements*, volume 1. 1997.

[101] S Temmerman, TJ Bouma, J Van de Koppel, D Van der Wal, MB De Vries, and PMJ Herman. Vegetation causes channel erosion in a tidal landscape. *Geology*, 35(7):631–634, 2007.

[102] Stijn Temmerman, Patrick Meire, Tjeerd J Bouma, Peter MJ Herman, Tom Ysebaert, and Huib J De Vriend. Ecosystem-based coastal defence in the face of global change. *Nature*, 504(7478):79, 2013.

[103] Rafael O Tinoco and Giovanni Coco. A laboratory study on sediment resuspension within arrays of rigid cylinders. *Advances in water resources*, 92:1–9, 2016.

[104] RO Tinoco and G Coco. Observations of the effect of emergent vegetation on sediment resuspension under unidirectional currents and waves. *Earth Surface Dynamics*, 2(1):83, 2014.

[105] RO Tinoco and G Coco. Turbulence as the main driver of resuspension in oscillatory flow through vegetation. *Journal of Geophysical Research: Earth Surface*, 123:891–904, 2018.

[106] RO Tinoco and G Coco. Turbulence as the main driver of resuspension in oscillatory flow through vegetation. *Journal of Geophysical Research: Earth Surface*, 123:891–904, 2018.

[107] W Vandenbruwaene, C Schwarz, TJ Bouma, P Meire, and S Temmerman. Landscape-scale flow patterns over a vegetated tidal marsh and an unvegetated tidal flat: Implications for the landform properties of the intertidal floodplain. *Geomorphology*, 231:40–52, 2015.

[108] Vito A Vanoni. *Sedimentation engineering.* American Society of Civil Engineers, New York, 1975.

[109] Stefan Vollmer and Maarten G Kleinhans. Predicting incipient motion, including the effect of turbulent pressure fluctuations in the bed. *Water Resources Research*, 43(5), 2007.

[110] Bernhard Vowinckel, Ramandeep Jain, Tobias Kempe, and Jochen Fröhlich. Entrainment of single particles in a turbulent open-channel flow: a numerical study. *Journal of Hydraulic Research*, 54(2):158–171, 2016.

[111] Tony L Wahl. Discussion of "despiking acoustic doppler velocimeter data" by derek g. goring and vladimir i. nikora. *Journal of Hydraulic Engineering*, 129(6):484–487, 2003.

[112] Nathaniel B Weston. Declining sediments and rising seas: an unfortunate convergence for tidal wetlands. *Estuaries and Coasts*, 37(1):1–23, 2014.

[113] Peter J Whiting and William E Dietrich. Boundary shear stress and roughness over mobile alluvial beds. *Journal of Hydraulic Engineering*, 116(12):1495–1511, 1990.

[114] Patricia L Wiberg and J Dungan Smith. Model for calculating bed load transport of sediment. *Journal of hydraulic engineering*, 115(1):101–123, 1989.

[115] John Widdows, Nick D Pope, and Mary D Brinsley. Effect of spartina anglica stems on near-bed hydrodynamics, sediment erodability and morphological changes on an intertidal mudflat. *Marine Ecology Progress Series*, 362:45–57, 2008.

[116] Peter Richard Wilcock. Estimating local bed shear stress from velocity observations. *Water Resources Research*, 32(11):3361–3366, 1996.

[117] Miguel Wong, Gary Parker, Paul DeVries, Timothy M Brown, and Stephen J Burges. Experiments on dispersion of tracer stones under lower-regime plane-bed equilibrium bed load transport. *Water Resources Research*, 43(3), 2007.

[118] EM Yager and MW Schmeeckle. The influence of vegetation on turbulence and bed load transport. *Journal of Geophysical Research: Earth Surface*, 118(3):1585–1601, 2013.

[119] JQ Yang, H Chung, and HM Nepf. The onset of sediment transport in vegetated channels predicted by turbulent kinetic energy. *Geophysical Research Letters*, 43(21), 2016.

[120] JQ Yang and HM Nepf. A turbulence-based bed-load transport model for bare and vegetated channels. *Geophysical Research Letters*, (under review), 2018.

[121] Judy Q Yang, Francois Kerger, and Heidi M Nepf. Estimation of the bed shear stress in vegetated and bare channels with smooth beds. *Water Resources Research*, 51(5):3647–3663, 2015.

[122] SL Yang, H Li, T Ysebaert, TJ Bouma, WX Zhang, YY Wang, P Li, M Li, and PX Ding. Spatial and temporal variations in sediment grain size in tidal wetlands, yangtze delta: On the role of physical and biotic controls. *Estuarine, Coastal and Shelf Science*, 77(4):657–671, 2008.

[123] UCE Zanke. On the influence of turbulence on the initiation of sediment motion. *International Journal of Sediment Research*, 18(1):17–31, 2003.

[124] Joy B Zedler and Suzanne Kercher. Wetland resources: status, trends, ecosystem services, and restorability. *Annu. Rev. Environ. Resour.*, 30:39–74, 2005.